Improving the Energy Density and Cycling Stability of All-Solid-State Batteries

By

Tan Shi

A dissertation submitted in partial satisfaction of the

requirements for the degree of

Doctor of Philosophy

in

Engineering - Materials Science and Engineering

in the

Graduate Division

of the

University of California, Berkeley

Committee in charge:

Professor Gerbrand Ceder, Chair
Professor Kristin Persson
Professor Bryan McCloskey

Spring 2020

Improving the Energy Density and Cycling Stability of All-Solid-State Batteries

Abstract

Improving the Energy Density and Cycling Stability of All-Solid-State Batteries

by

Tan Shi

Doctor of Philosophy in Engineering - Material Science and Engineering

University of California, Berkeley

Professor Gerbrand Ceder, Chair

The emerging electrical vehicle market and global decarbonization trend demand batteries with higher energy density, better safety, and longer cycle life. An all-solid-state battery has the potential to meet such requirements and is widely considered as the next-generation battery technology to replace the current Li-ion batteries. The remarkable success in the discovery of ceramic alkali superionic conductors has provided a wide selection of solid electrolytes, allowing the fabrication and testing of all-solid-state battery cells. However, the current solid-state battery still cannot compete with state-of-the-art Li-ion technology because of its poor cycle stability and low energy density.

One of the causes of the poor cycle stability in all-solid-state batteries is the lack of chemical stability between the solid electrolytes and electrodes. To efficiently and systematically investigate these chemical compatibility issues, a methodology was developed combining density functional theory calculations and simple experimental techniques such as X-ray diffraction, simultaneous differential scanning calorimetry, thermal gravimetric analysis, and electrochemistry. Two aspects of the chemical stability were investigated: the electrochemical stability of the solid-state conductor, which is relevant wherever the electrolyte contacts an electron pathway, and the electrochemical stability of the electrode/electrolyte interfaces. Computationally derived voltage stability windows are small for both Na_3PS_4 and Na_3PSe_4, which are confirmed experimentally. By combining the theory calculations and simple experimental techniques, the most stable system ($NaCrO_2$|Na_3PS_4|Na–Sn) within a selected Na solid-state battery chemical space (more than 20 different combinations of electrodes and electrolytes) was efficiently found. Important selection criteria for the cathode, electrolyte, and anode in solid-state batteries are derived from this study. This method provides an essential guide for probing the chemical instability issue in the all-solid-state battery, and experimental results show the importance of interfacial engineering for the all-solid-state battery.

The mechanical degradation in all-solid-state batteries can also cause rapid capacity fade. To investigate the severity of the mechanical degradation after long-term cycling, the all-solid-state composite cathode morphology before and after long-term cycling was imaged using the focused ion beam scanning electron microscope tomography. A large amount of void volume (~ 12%) and contact loss area (> 10%) are found in the cathode composite after 50 cycles, revealing the severe mechanical degradation during cycling. The contact loss between the cathode and solid electrolyte

is accompanied by the rapid capacity drop during battery cycling. This result suggests that mechanical degradation does not progress gradually starting from the first cycle. Instead, the majority of the void formation and contact loss likely occurs at later cycles and over a short time. This part of the study highlights the importance of mechanical stability for the all-solid-state battery.

Lastly, increasing the cathode active material loading is proposed as a method to increase the full cell energy density of the all-solid-state battery. Current low active material loading in the composite electrode is one of the main reasons for the low full cell energy density. In this part, modeling and experimental results show that a higher cathode loading and therefore an increased energy density can be achieved by increasing the ratio of the cathode to conductor particle size. The utilization of the cathode materials in the solid-state composite is shown to be highly dependent on the particle size ratio of the cathode to the solid electrolyte, especially in the regime of high cathode loading. These results are consistent with the ionic percolation being the limiting factor in cold-pressed solid-state cathode materials and provide specific guidelines on how to improve the energy density of composite cathodes for solid-state batteries. By reducing solid electrolyte particle size and increasing the active material particle size, over 50 vol% cathode loading with high cathode material utilization was experimentally demonstrated. This part of the work proves that a commercially-relevant, energy-dense cathode composite is achievable through simple mixing and pressing method.

Table of Contents

List of Figures

List of Tables

Acknowledgments

I would first like to thank my advisor, Professor Gerbrand Ceder, for his guidance during my graduate studies. Professor Ceder showed me how to develop and carry out a scientific research project rigorously, which was the most valuable knowledge I gained during my Ph.D. career.

I would also like to thank my qualifying exam and dissertation committee members, Professor Kristin Persson, Professor Bryan Mccloskey, Professor Mark Asta, and Professor Jeffrey Long, for taking time out of their busy schedules to help me develop my research project.

I thank the sponsor of our solid-state battery project, Samsung Advanced Institute of Technology, for their interests and support of our research project.

I owe many thanks to all of my collaborators (Yaosen Tian, Will Richards, Juchuan Li, Jae Chul Kim, Shou-Hang Bo, Penghao Xiao, Deok-Hwang Kwon, Gopalakrishnan Sai Gautam, Khetpakorn Chakarawet, Hyunchul Kim, Qingsong Tu, Yihan Xiao, Lincoln Miara, and Olga Kononova). Completing my research project would not have been possible without their contributions, and I am grateful for their valuable insights and comments on my research.

I want to thank all the members of the Ceder group. It was a great pleasure to work with and learn from so many bright minds. In particular, I would like to thank Dr. Shou-Hang Bo, who mentored me through the first two years of my Ph.D. with patience, and Dr. Penghao Xiao, who taught me a lot about the computational materials science. The members of the solid-state battery subgroup are greatly acknowledged. Our subgroup meetings were always substantive and rewarding. I would like to especially thank the two theorists in the subgroup, Qingsong Tu and Yihan Xiao, whom I often bounced ideas off of.

I was lucky enough to meet my fiancé Yaqian Zhang during my Ph.D. She has brought much joy and encouragement to both of my personal and work lives.

Finally, I would like to thank my grandparents, my parents and my sister for their love. I would not be here without their continued support for me to pursue my interests.

Chapter 1 - Introduction and Background

1.1 Motivation

Li-ion battery (LIB) has become ubiquitous in modern electronics. It is the critical component in consumer electronics such as cellphones, laptops, and even power tools. LIB is gathering even more attention with the urgent need for decarbonization in recent years. The application of LIB in electric vehicles (EVs) and grid storage is considered an important step to reduce fossil fuel consumption.

The emerging EV market has played a major part in the rapid growth of the LIB market. In 2018, the global EV fleet exceeded 5.1 million, up 2 million from the previous year and almost doubled the number of new electric car sales.[1] However, global EV adoption is still in the very early stage, and further adoption of EVs requires the improvement of their batteries. Higher energy density batteries allow an EV to travel longer on a single charge, and higher power density batteries reduce the charging time of the EV, both of which are critical for EVs to replace internal combustion engine vehicles. Improved safety is also needed for EV batteries. The flammability of the liquid electrolyte in the current LIBs is a huge concern.

There has been intense research effort on improving the energy density of the LIB, a majority of which are focused on better electrode materials. With the development of high energy density Li-rich cathodes and the incorporation of Si nanoparticles in the carbon-based anode, the energy density of LIBs has increased from ~ 90 Wh kg^{-1} to close to 250 Wh kg^{-1} at the cell level over the last two decades.[2] However, the EV market demands even better batteries with energy density over 350 Wh kg^{-1} or even 400 Wh kg^{-1}.[3] Such a further increase in energy density cannot be met by slight modifications at the material level and requires a dramatic change in the battery components. Utilization of a Li metal anode has been considered as a key step to increase the energy density of the next generation batteries.

Li metal, which has a theoretical capacity of 3860 mAh g^{-1}, is the ideal anode material for high energy LIBs. Its instability with current liquid electrolyte and the tendency to form dendrites during cycling raise safety concerns and prevent its application in LIBs.[4] In an all-solid-state battery (SSB), the problematic organic liquid electrolyte in LIBs is replaced with inorganic solid electrolytes. A high energy density SSB with Li metal anode has been considered by many as the promising next-generation technology to replace the current LIBs. However, current SSB still suffers from low energy density and poor cycling stability, and cannot compete with the LIB. This dissertation will focus on the understanding of the causes of poor cycling stability in the SSB and methods to increase its energy density.

1.2 Overview of secondary batteries

Before discussing SSBs, a brief introduction of the working principle and the main components of a secondary battery is needed.

1.2.1 Working principle of secondary batteries

The main components in a secondary battery include the cathode, the anode, and the electrolyte. Figure 1.1 shows a schematic of their typical configuration in a LIB. During the battery operation, both electrons and ions are exchanged between cathode and anode. The ionic species that are mobile in the battery is often called the working ion, which is the Li-ion in this case. The electrons flow through the external circuit, and the working ions flow through the ionic conductive

electrolyte. Figure 1.1 shows the flow of the charged species during the discharging process. During the discharge, chemical potential difference drives Li ions to move from the anode to the cathode with the accompanying electrons passing through the external circuit doing electrical work. The reverse process takes place during the charging process, where external work is needed to move the Li ions and electrons back to the anode from the cathode side. The voltage of the battery is therefore determined by the chemical potential difference of the two electrodes, and can be expressed by the Nernst equation:

$$Voltage = -\frac{\mu^c - \mu^a}{zF} \tag{1.1}$$

μ^c and μ^a are the chemical potentials of the working ion in the cathode and anode, z is the working ion valence, and F is the Faraday constant. The capacity of the battery is defined as the number of electrons transported between electrodes divided by the mass of cathode material (electrode-based specific capacity) or the mass of all cell components (cell-based specific capacity). The product of the average cell voltage and specific capacity determines the specific energy density of the cell. In addition, the mass-specific energy density (or gravimetric energy density), volume-specific energy density (volumetric energy density) is also used when comparing different battery cells.

Figure 1.1 only shows a simplified version of a working battery. In reality, cathode and anode do not consist of one single material, but are composites consisting of active material, polymer binder, conductive additive, and electrolyte. Active materials, or commonly called anode and cathode materials, provide the Li storage and extraction capacity. The polymer binder connects the individual particles and allows them to form a continuous film on top of the current collector. The conductive additives are often small carbon particles such as Super P or carbon microfibers, which provide electron pathways to active particles across the composite electrode. The composite electrode has porosity up to ~ 40%, which allows liquid electrolyte wetting. Good contact between electrolyte and active material particles allows the Li ion transport within the composite electrolyte and is critical for full capacity utilization and achieving high power density.

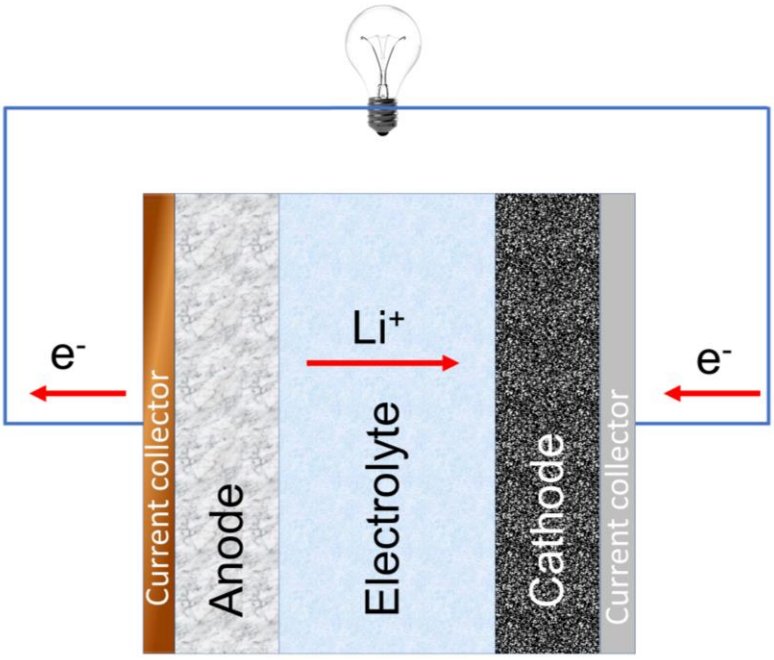

Figure 1.1: Schematic representation of a traditional LIB. The direction Li ion and electron movements during discharging are labeled in the figure.

Materials properties needed for the three main components in LIBs (cathode, anode, and electrolyte) are very different and will be discussed in the following sections. Many different electrode materials have been investigated and reported, which have very exotic structures and consist of elements spanning a large area of the periodic table. Here, only materials that are commercialized or likely to be commercialized will be discussed.

1.2.2 Cathode materials for LIBs

The most common cathode materials used in current LIBs are lithium metal oxides, often in the form of $LiMO_2$, where the M is one or a combination of several transition metals. The Li ion is reversibly extracted from and inserted into the cathode material during cycling. The overall charge balance is maintained by the oxidation and reduction of the transition metal in the material. These cathode materials, therefore, are also called intercalation cathodes. An ideal cathode material must maintain its structure after many cycles and requires good chemical and structural stabilities after a large amount of Li extraction (at high voltage). This is often difficult to achieve in reality as structure change [5,6] and O loss [7,8] are observed in most highly delithiated cathode materials.

Intercalation cathodes usually have a layered crystal structure, where Li and transition metal ions sit in alternating oxygen octahedral layers (Figure 1.2(a)). $LiCoO_2$ is the most well-known layered cathode material. It is the first commercialized LIB cathode material and is still widely used in today's portable electronics.[9] However, Co reserves and production are limited and cannot meet the demand of large-scale energy storage applications such as EVs and grid storage.[10] To avoid the expensive Co used in $LiCoO_2$, much effort has been devoted to utilizing other transition metals in the layered structure such as Mn and Ni. In these materials, a small amount of Co is still needed to stabilize the layered structure, leading to layered cathode materials with multiple transition metals such as $LiNi_{0.33}Mn_{0.33}Co_{0.33}O_2$ (NMC111), $LiNi_{0.5}Mn_{0.3}Co_{0.2}O_2$ (NMC532), and $LiNi_{0.8}Mn_{0.1}Co_{0.1}O_2$ (NMC811). These NMC cathodes not only reduce the Co content but also allow extraction of more Li in the structure, increasing the specific capacity.

Several other cathode materials have also been investigated and commercialized. $LiMn_2O_4$ forms a spinel structure with 3D Li-ion diffusion channels (Figure 1.2(b)), which allows fast Li diffusion within the cathode particle. However, the low specific capacity (110 – 120 mAh g^{-1}) limits its energy density. Poor stability, especially at elevated temperatures, further limits its applications.[11] Another important cathode material is $LiFePO_4$, which has an olivine structure (Figure 1.2(c)). This cathode material not only reduces cost by utilizing Fe redox but also has high rate capability, high stability, and long cycle life. However, unlike in layered cathodes, which have 2D Li diffusion, and spinel cathodes, which have 3D Li diffusion, olivine cathodes only allow Li diffusion through a 1D channel. The 1D diffusion channel can be easily blocked by defects where transition metal ions occupy Li sites. Therefore, the nano-sized cathode particles are required to minimize the channel blockage.[11] Although $LiFePO_4$ has a large specific capacity (110 – 120 mAh g^{-1}), its voltage is only slightly over 3 V, which makes its energy density lower than layered cathode materials.

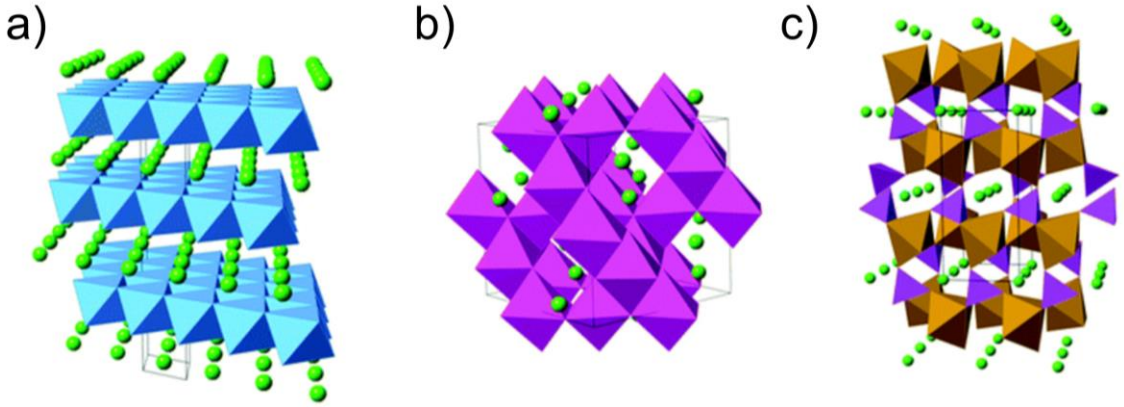

Figure 1.2: Representative crystal structures of cathode materials for LIBs: (a) layered α-$LiCoO_2$; (b) cubic $LiMn_2O_4$ spinel; (c) olivine-structured $LiFePO_4$. Li ions are shown as light green spheres, CoO_6 octahedra in blue, MnO_6 octahedra in mauve, Fe–O polyhedra in brown, PO_4 tetrahedra in purple.[12]

While many other high-performance cathode materials with different structures and chemistries have been reported [13], layered oxide materials, particularly Ni-rich compounds, will likely dominate the market in the near future because of their good performance, competitive cost, and well-established manufacturing process. Therefore, NMC532 is used as the model cathode material in Chapters 3 and 4.

1.2.3 Anode materials for LIBs

Improving anode materials are equally important for increasing battery energy density. Carbon-based anode materials were the first to be commercialized in the early 1990s, and are still the most important class of LIB anode material today. Graphite is the most widely used anode materials today due to its low cost and good performance. Graphite has a hexagonal lattice symmetry with layers of graphene stacked together. Li ions can be intercalated between the graphene layers, forming a LiC_6 structure, which corresponds to a specific capacity of 372 mAh g^{-1}. In addition to the large specific capacity, graphite also has a very low insertion voltage. The majority of the capacity comes at a voltage below 0.2 V against Li metal, which is beneficial for maximizing the energy density.[14] Li diffusion within the graphene layers is relatively fast. Still, when flake-shaped natural graphite is stacked together onto the current collector, the Li diffusion into the layers becomes the limiting step.[14] Synthetic graphite with a spherical shape was designed to

avoid this Li diffusion issue. It also allows high packing density, which allows higher volumetric energy density, and reduced surface area to minimize electrolyte decomposition. These synthetic graphite anode materials such as mesocarbon microbeads (MCMB) or massive artificial graphite (MAG) have dominated the small format LIB market.[15]

Another important class of anodes is the alloying anode materials. Si is a particularly promising alloying anode material because of its abundance, low cost, low voltage (0.4 V on average), and most importantly, a large specific capacity of 4200 mAh g^{-1} by allowing up to 4.4 Li per Si lithiation. However, dramatic volume expansion (over 300%) during the lithiation/delitiation process creates huge stress within the particle, often causing the particles breaking apart, leading to the loss of electronic pathways and continuous Li consumption due to the SEI layer formation.[16] Reducing the size of Si anode particles can help limit the mechanical failure and improve cycle performance. Specifically, Si nanoparticles and Si nanowires/nanotubes have shown good performances when embedded in the carbon-based matrix.[17,18] The carbon matrix provides electron transport, porosity for electrolyte wetting, and space for Si particle volume change. This class of Si/C composites can often achieve capacity exceeding 1000 mAh g^{-1}, and several variations have been successfully commercialized.[19-21] The incorporation of alloying anode materials has contributed greatly to the increase in full cell energy densities in recent years.

1.2.4 Electrolytes for LIBs

The electrolyte plays an important role in transporting Li ions between cathode and anode. Electrolytes must possess several important characteristics: (1) High ionic conductivity. The ionic conductivity of electrolytes relates to the mobility of Li ion in the electrolyte. How fast Li ion can move within the electrolyte is one important factor that controls the overpotential and rate capability of the battery. (2) Wide electrochemical window. The electrochemical window describes the voltage range (usually reference against Li metal) where the electrolyte is stable. The unstable electrolyte can be oxidized or reduced under battery operation conditions, which not only causes electrolyte consumption but also creates a decomposition layer on the electrode surface, severely hindering the ion transport between electrolyte and electrode. An ideal electrolyte must have high cathodic stability (stable with Li metal) and high anodic stability (stable with high voltage cathode). (3) Good thermal stability. Batteries are expected to function at both low and high temperatures. The electrolyte is the component whose performance is most susceptible to temperature. At low temperatures, lowered thermal energy will reduced the conductivity of the electrolyte. A liquid electrolyte can even freeze when the temperature is below the freezing point. At high temperatures, the electrolyte can decompose easily, which reduces battery life. Another important thermal consideration is flammability. The electrolyte should also not be flammable in case of external abuse or internal shorting.

The most common electrolyte in current LIBs uses a mixture of ethylene carbonate, dimethyl, diethyl, and ethyl-methyl carbonate and $LiPF_6$ salt as the liquid electrolyte solution. This class of electrolytes is widely used because of their high polarity (good conductivity in the solutions), a reasonable temperature range (low freezing point and high boiling points), and low toxicity.[22] However, the alkyl carbonate/Li salt-based electrolyte is far from perfect. One major issue of this electrolyte is its flammability. The carbonate-based liquid electrolyte can undergo a rapid exothermic decomposition reaction when thermal runaway occurs as a result of electrical or mechanical abuse, which can potentially lead to fires or explosions.[23] Another issue is its stability. $LiPF_6$, the Li salt commonly used, can decompose to LiF and PF_5, and the PF_5 readily hydrolyzes to form HF and PF_3O. These hydrolysis products can react with both anode and cathode, leading to reduced performance during long-term cycling.[24] Additionally, alkyl carbonate

solvents cannot accommodate high voltage systems. Oxidation of the carbonate solvents usually occurs just over 4 V, and they are mostly not stable against Li metal anode, forming solid electrolyte interphase (SEI). Various side reactions at different potentials for alkyl carbonate/Li salt-based electrolytes can be seen in Figure 1.3. The limitations of the current liquid electrolytes have motivated intense research into alternative electrolyte materials, including inorganic solid electrolytes.

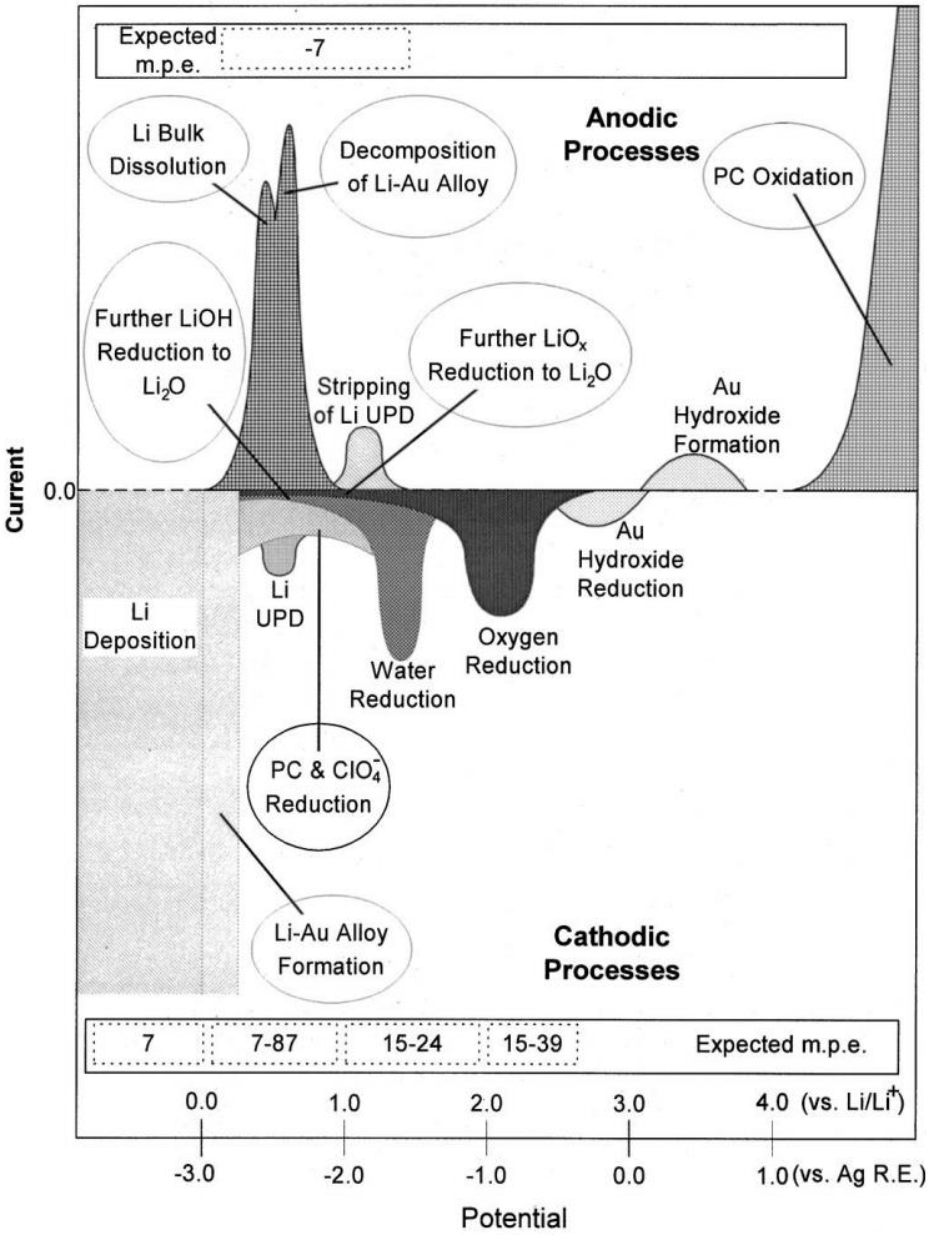

Figure 1.3: Organic liquid electrolyte decomposition. A schematic drawing showing the potential at which various electrochemical processes occur for a gold electrode in an alkyl carbonate/Li salt-based electrolyte.[25]

1.3 Background on solid conductors and SSBs.

1.3.1 Overview of all-solid-state batteries

All-solid-state batteries (SSBs) have been considered by many as a next-generation energy storage technology. The working principle of the SSBs is the same as traditional LIBs, with working ions and electrons transporting between cathode and anode. The main difference between the two is that SSBs uses a solid ionic conductor as the electrolyte to transport working ions between the anode and cathode. Over the past two decades, intense research effort has been focused on the development of the solid electrolyte (SE), resulting in the discovery of a wide variety of fast solid ionic conductors.[26] The rapid progress of the SSB research has pushed it close to commercialization, with several major automotive companies have targeted the mid-2020s to begin using SSBs in electric vehicles (EVs).[27-29]

Figure 1.4 shows the difference in the cell structures between a conventional LIB and a SSB. In the SSB, a thin layer of SE is used as a separator between the anode and cathode. The SE (yellow particles) is also mixed in the cathode composite to provide ionic pathways for individual cathode particles. The most common SEs can be divided into two categories: organic and inorganic (or ceramic) SEs. Although organic SEs are mechanically soft and can better accommodate the electrode volume change, their low ionic conductivity limits the power density at room temperature.[30,31] In contrast, inorganic SEs shows much better ionic conductivities even at low temperature, therefore enables the realization of practical SSB full cells.

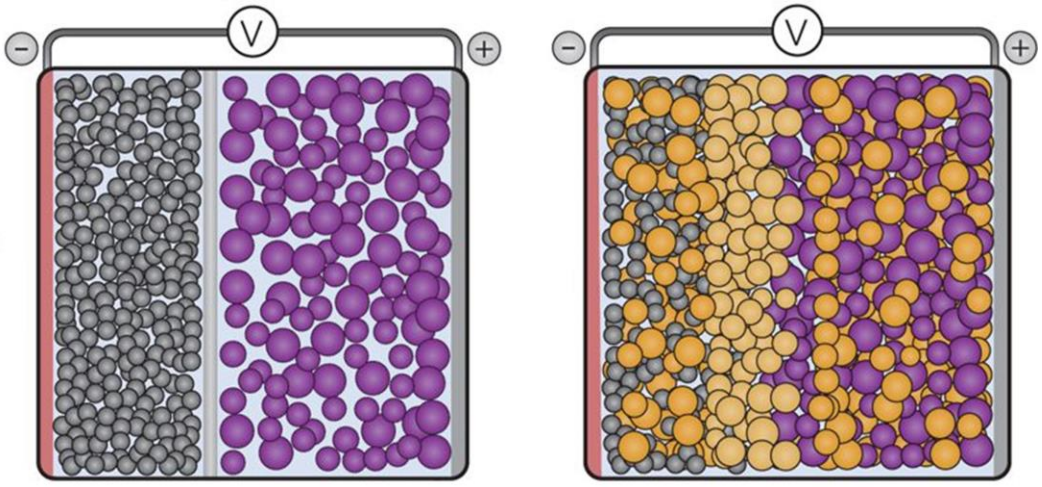

Figure 1.4: Cell structure differences between SSBs and LIBs. Schematic drawing of the difference between a conventional LIB (left) and a SSB (right).[32] The yellow and orange spheres in SSB are SEs that are both used as the separator and mixed in the electrode.

1.3.2 Potential benefits of all-solid-state batteries

Improved safety is one of the most significant advantages of SSBs over current LIBs. The safety of LIBs became the central issue from both the battery industry and the public after several widely publicized safety incidents involving both consumer electronics and EVs [33,34]. The main cause of the flammability in current LIBs is the carbonate-based organic liquid electrolyte. Without the flammable liquid electrolyte, SSBs cannot burn or explode even under electrical or mechanical abuse. This inherent safety means that SSBs are better suited for consumer electronics and EV applications than LIBs.

Another important advantage of SSBs is higher energy density. Higher energy density in SSBs can be achieved through the use of a lithium metal anode, which has a high theoretical specific capacity of 3860 mAh g^{-1}. Li metal anode cannot be used in current LIBs, mainly due to two reasons: dendrite growth and lithium/electrolyte consumption. Dendrite growth in LIBs, where the electrodeposited Li metal grows as sharp tips towards the opposite electrode, is particularly dangerous because the potential short circuit can lead to fast exothermal reaction and battery fire. The origin of the dendrite growth in LIBs can be trace to the SEI layer formed on the Li surface. During the Li plating process, the SEI can break open and expose fresh Li surface as a preferential plating site, causing the uneven Li growth rate.[4] The continuous SEI formation also causes Li and electrolyte consumption, limiting the cycle life of LIBs with Li metal anode.[4] SSBs can potentially solve both issues related to the Li metal anode in LIBs. The inherent safety makes the dendrite growth a less concerning issue, and a fully dense SE pellet can potentially mechanically prevent the dendrite propagation. The electrolyte consumption issue can also be avoided by the formation of a stable or passivated interface between the Li and SE. Figure 1.5 shows the estimated volumetric energy density for SSBs utilizing a $LiNi_{0.6}Mn_{0.2}Co_{0.2}O_2$ (NMC622) cathode, Li_3PS_4 (LPS) SE, and Li metal anode. With a high cathode loading (> 80 wt% active material in the cathode composite) and a thin separator (< 50 μm), SSBs have a large volumetric energy density advantage over current LIBs. Further improvement in energy density for SSBs is achieved through the utilization of bi-polar electrode stacking cell design. Figure 1.6 shows the schematic comparison between the cell structures of the conventional LIBs and SSBs with bi-polar stacking cell design. The bi-polar stacking allows the use of only one current collector per unit cell, which can reduce the overall current collector thickness as well as the "dead volume" between cells.[35] It also makes the construction of high voltage cells easier since the unit cells are now connected in series, which would be beneficial for high-voltage, high power applications such as EVs and power tools.

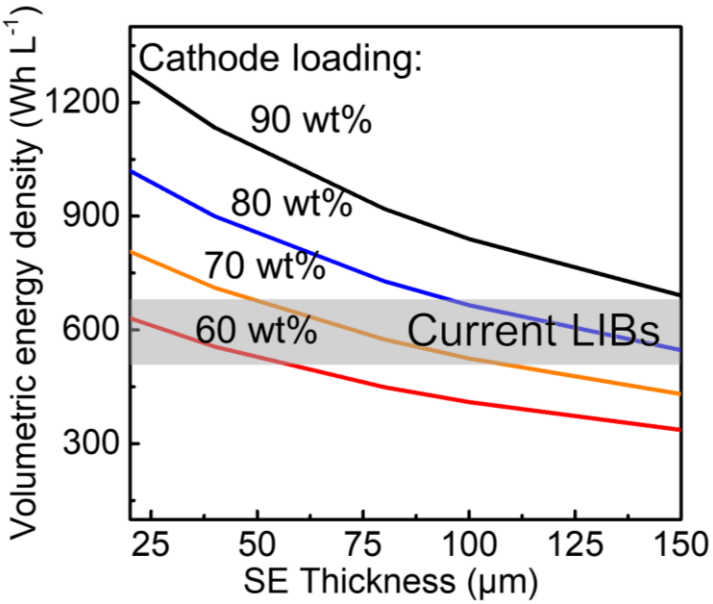

Figure 1.5: Energy density comparison between SSBs and LIBs. Estimated cell-level volumetric energy density for SSB utilizing Li metal anode with different cathode loadings and separator thicknesses compared with those of current LIBs. The model uses NMC622 as the cathode, 20% excess Li metal as the anode, and LPS as the SE.

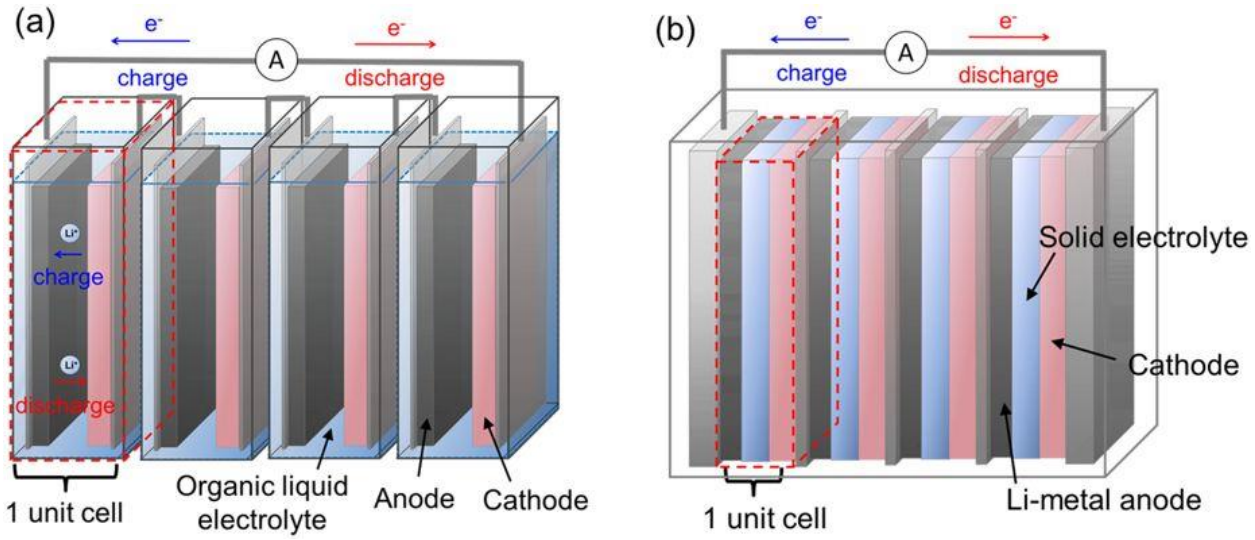

Figure 1.6: Benefits of bi-polar stacking. Schematic of (a) a conventional prismatic LIB cell and (b) a bi-polar stacking SSB cell.[36]

Also, SSBs can potentially achieve higher power densities than LIBs. A high power density allows the high current rate during charging and discharging, and is critical to achieving fast charging and high peak power output, which is essential for EV applications. A high power density requires low resistance and fast Li transport within the cell to reduce the overpotential under high current density, which can be achieved by increasing the ionic conductivity of the electrolyte. Several SEs have shown ionic conductivities higher than those of current liquid electrolytes (~ 10 mS cm^{-1}), including $Li_{9.54}Si_{1.74}P_{1.44}S_{11.7}Cl_{0.3}$ and $Li_{10}GeP_2S_{12}$.[35,37] SSBs with very high power density (stable cycling at 18C) have also been demonstrated using these superionic conductors.[35] Recent research efforts have resulted in an expanded understanding of the chemical and structural factors that control the ionic conductivity in SEs. Therefore, it is reasonable to expect that more superionic conductors will be available for high-power SSB applications in the future.

1.3.3 Ion transport in solid conductors

Solid electrolytes are fast ion conductors (or superionic conductors) that have high ionic conductivity and low electronic conductivity. To understand the chemical and structural effects on the ionic conductivity, the ion diffusion mechanism in solids need first be explained.

At the atomic level, the working ions in solids mostly diffuse through either vacancy or interstitial defects. The working ions sit in stable sites (usually octahedral or tetrahedral sites) within the lattice. They can be thermally excited, overcome a small energy barrier, and hop to adjacent vacancy or metastable sites. The diffusion pathway consists of many individual hops from one site to another. To be able to have long-range diffusion, the sites must form a percolating network.

The diffusion via hopping mechanism suggests that the ionic conductivity of the solid, σ, is related to how easily the ions can hop between sites, which can be described by the ion mobility u and the concentration of available hopping ions in the materials n. The conductivity can be represented as follows:

$$\sigma = q\, n\, u \tag{1.2}$$

where q is the working ion charge. The mobility of the ion is mainly governed by the energy barrier between hops and can be described by the simple Arrhenius relationship. The conductivity can be further expressed as:

$$\sigma = \sigma_0 e^{-\frac{E_a}{k_B T}} \tag{1.3}$$

where σ_0 is the pre-factor, E_a is the activation energy, which includes the mobile defect formation energy (E_f) and the ion migration energy barrier (E_m), T is the absolute temperature, and k_B is the Boltzmann constant. The pre-factor σ_0 is related to the other details related to the hopping process, such as hopping distance (α), jumping frequency (υ), and migration entropy (ΔS_m). For the direct uncorrelated hopping, the pre-factor σ_0 can be expressed as follows:

$$\sigma_0 = \upsilon\, \alpha^2 \frac{nq^2}{k_B} e^{-\frac{\Delta S_m}{k_B}} \tag{1.4}$$

From equation (1.3), it is clear that the energy barrier between hopping is the dominating factor controlling the ionic conductivity in solids. The energy change along the working ion diffusion path is often described by the energy landscape, and a schematic representation of such an energy landscape is shown in figure 1.7. The hopping energy barrier is the energy difference for Li sitting in the stable site and the highest energy site during migration (or the transition state). Therefore, a flat energy landscape, where the energy change along the path is minimal, is ideal for fast ion diffusion. The mobile ion energy change along the path is determined by the surrounding anions or anion groups in the structure. Both the anion structure and chemistry will influence the energy change along the diffusion path, and minimizing the hopping energy barrier requires the optimization of both material structure and chemistry.

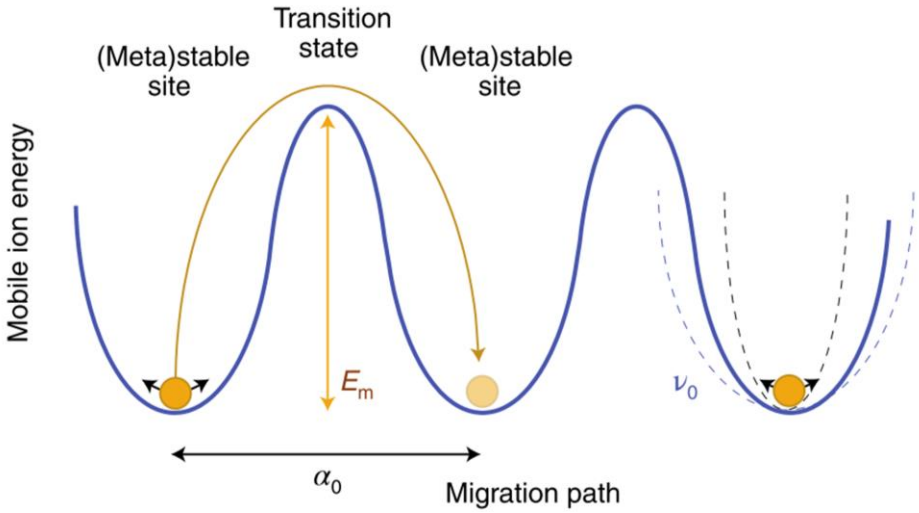

Figure 1.7: Energy landscape during ion diffusion. A schematic drawing of a representative energy landscape along a working ion migration path. The conductivity is related to the hopping energy barrier E_m, hopping distance α, and the hopping frequency υ.[38]

The anion structure framework is critical in determining the hopping energy barrier. The working ion site energy is largely determined by how many bonds it forms with nearby anions (its coordination number). Therefore, an ideal anion structure framework would have a minimal coordination number change for the working ion along its diffusion path, resulting in a flat energy

landscape and a small energy barrier. Only certain anion frameworks can satisfy this criterion. For example, Li can directly hop between adjacent tetrahedral sites in a body-centered cubic (bcc)-like anion framework, leading to a reduced energy barrier. In contrast, other close-packed frameworks, where Li must hop along a tetrahedral–octahedral–tetrahedral path, often has a much larger energy barrier.[39]

The anion chemistry can also modify the hopping energy barrier. Larger and more polarizable anions can better screen the cation-cation interactions during the working ion migration, reducing the transition state energy. For example, while Li_6PO_5Cl and Li_6PS_5Cl both form argyrodite-type structure, sulfide version exhibit higher ionic conductivity than the oxide version because sulfur anions are larger and more polarizable compared to oxygen anions.[40] Additionally, replacing a single anion atom with a large polyanion group can add a degree of freedom (rotational), and further reduces the interaction between the working ion and its neighboring anions, lowering the energy barrier. This strategy has been applied to successfully increase the ionic conductivity of the sodium anti-perovskite Na_3OX (X = Cl, Br, I) materials by substituting the halide anion with the BH_4 polyanion group.[41]

Another strategy to lower the hopping energy barrier is to push up the stable site energy, thereby minimizing the difference between the stable site and the transition state. The site energy of the mobile ions can be raised by the addition of mobile ions in the pristine structure, forcing them to occupy higher energy sites. This phenomenon has been observed in garnet-type oxide ionic conductors. While $Li_7La_3Zr_2O_{12}$ (LLZO), $Li_5La_3Nb_2O_{12}$, and $Li_3La_3Te_2O_{12}$ all have the same garnet structure, the ionic conductivity of the materials greatly improves when the Li content is increased from 3 in the Te version to 7 in the Zr version. This is because the high Li content pushes Li to occupy the high energy octahedral sites to minimize the Li–Li interaction. This higher occupancy of the high energy site flattens the migration energy landscape, therefore reducing the hopping energy barrier.[42]

Equation (1.2) suggests that the conductivity is also related to the carrier concentration or the migrating defect (vacancy or interstitial) concentration. The defect formation energy also affects the activation energy. Therefore, controlling the defect chemistry in the material is also crucial for ionic conductor optimization. Intrinsic defect concentration alone is usually not high enough to achieve high ionic conductivity. The cation vacancy or interstitial defect concentration can often be increased by aliovalent doping. For example, by replacing Ta with Zr, 12.5% excess Li can be introduced into the $LiTaSiO_5$ structure as interstitial defects, lowering the activation energy by 0.31 eV and increasing the room temperature ionic conductivity by more than two orders of magnitude.[43]

1.3.4 Common ceramic solid electrolytes

SEs with various chemistries and structures have been reported. Several of the representative SEs with high room temperature conductivities have been listed in table 1.1. A large majority of the SEs with high conductivities can be classed into two large categories based on their anion chemistry: sulfide-based or oxide-based SEs.

Structure type	Material	σ (S cm^{-1})	E_a (eV)	Reference
Amorphous	LiPON	6.40×10^{-6}	0.47	[44]
	$75Li_2S–25P_2S_5$	2×10^{-4}	0.35	[45]
LGPS-type	$Li_{10}GeP_2S_{12}$	1.2×10^{-2}	0.25	[37]
	$Li_{9.54}Si_{1.74}P_{1.44}S_{11.7}Cl$	2.5×10^{-2}	0.24	[35]
Argyrodite	Li_6PS_5Cl	1.3×10^{-3}	0.33	[46]
Garnet	$Li_7La_3Zr_2O_{12}$	2.4×10^{-4}	0.31	[47]
NASICON	$Li_{1.2}Al_{0.2}Ti_{1.8}(PO_4)_3$	5×10^{-3}	0.29	[48]
(Anti)Perovskite	$Li_{0.38}La_{0.56}Ti_{0.99}Al_{0.01}O_3$	3.17×10^{-4}	0.36	[49]
	$Li_3OCl_{0.5}Br_{0.5}$	1.94×10^{-3}	0.18	[50]

Table 1.1: Selected SEs with different structure types that show high room temperature conductivities.

Sulfide materials have good anion chemistry because of sulfur's large ionic size and high polarizability. Many sulfide SEs can achieve very high room temperature ionic conductivity, even surpassing that for conventional liquid electrolytes. $Li_{10}GeP_2S_{12}$ can reach a room temperature conductivity up to 1.2×10^{-2} S cm^{-1}. Its conductivity can be further increased by Si and Cl doping, reaching a room temperature conductivity up to 2.5×10^{-2} S cm^{-1}.[35] Other than the anion chemistry, the bcc cubic anion sub-lattice structure also contributes to LGPS-type SE's high ionic conductivity. Several other crystalline phases in this chemical space have also been shown to have high ionic conductivities on the order of 10^{-3} S cm^{-1}, including $Li_7P_3S_{11}$ and Li_6PS_5Cl.[51] Many other sulfide SEs originate from the Li_2S-P_2S_5 chemical space. One of the early practical sulfide SEs is the amorphous $75Li_2S–25P_2S_5$ (LPS) obtained via mechanical milling, which can achieve a conductivity of 2×10^{-4} S cm^{-1}.[45] The increased Li site energy in the metastable amorphous structure likely contributes to the high ionic conductivity. However, the factors controlling the conductivity in such an amorphous structure is still unclear. LPS has been widely used in SSB research because of its low cost and simple fabrication method and therefore is used as a model SE material in Chapters 3 and 4.

Another important group of ceramic SEs is the oxide-based SEs. Garnet-type materials such as $Li_5La_3Nb_2O_{12}$ and $Li_5La_3Ta_2O_{12}$ has been found to allow fast Li ion conduction as early as 2003.[52] Their initially low room temperature conductivity (~10^{-6} S cm^{-1}) can be greatly improved by substituting in Zr, forming a Li-rich $Li_7La_3Zr_2O_{12}$ (LLZO) phase. LLZO can achieve a high ionic conductivity of 2.4×10^{-4} S cm^{-1} with a low activation energy of 0.31 eV.[47] Another type of oxide SE is based on the perovskite (ABO_3) structure. The early reported $Li_{0.34}La_{0.51}TiO_{2.94}$ (LLTO) perovskite already exhibit bulk ionic conductivity up to 10^{-3} S cm^{-1}.[53] The conductivity of these perovskite SEs are also very sensitive to the Li content and can be modified through various cation doping.[54] However, LLTO is not an ideal candidate for SE because it is not stable against Li metal or at low Li potential, and will have Li insertion and reduction of Ti^{4+} to Ti^{3+}. Oxide materials with NASICON-like structure have also been studied as SEs. NASICON-like ceramic electrolytes have a formula of $AM_2(PO_4)_3$, where A site is occupied with alkali metal ions such as Li^+ or Na^+, and M site is occupied with higher valence cations. Similar to the garnet and perovskite compounds, the conductivity of NASICON conductors are highly sensitive to the Li content in the structure. By substitution of Ti^{4+} with Al^{3+}, the Li content in the $LiTi_2(PO_4)_3$ NASICON can be increased, and the resulting $Li_{1.2}Al_{0.2}Ti_{1.8}(PO_4)_3$ material exhibits an ionic conductivity of 5×10^{-3} S cm^{-1}, three orders of magnitude higher than that of the undoped

structure.[48] However, the presence of Ti^{4+} in the structure makes many NASICON materials suffer from the instability against Li metal anode.

1.3.5 Current issues for SSBs

Despite the advantages mentioned above, SSBs currently still cannot compete with LIBs commercially. The large-scale production of high-energy-density SSBs with long cycle life still faces many challenges, as shown in Figure 1.8. Three main challenges for SSBs are: 1) Poor chemical stability at various interfaces. Many SEs do not have a wide voltage window and can decompose or react with electrode materials. The resulting reaction layer can be a poor ion conductor and increase the interfacial resistance. 2) Forming and maintaining intimate particle contact. Mechanical stability is also difficult to achieve and maintain at the cathode-SE interface. The rigid SEs cannot accommodate the large volume change of active materials during cycling and can cause contact loss during cycling. The mechanical and chemical instability at various interfaces creates a large cell overpotential, resulting in a low energy density and severe capacity fade. 3) Fabrication challenges for high-energy-density SSBs. Figure 1.5 shows the energy density of SSBs is highly dependent on the separator thickness and the cathode loading. Reducing the separator thickness can lower its uniformity and mechanical integrity, and increasing the cathode loading will reduce the ion percolation pathway in the cathode composite. Therefore, reducing the SE separator thickness and increasing cathode loading require careful engineering and optimization for large-scale bulk-type SSB fabrications. Finally, the use of a Li metal anode brings another set of issues, including the contact loss during Li plating/stripping and dendrite growth.[55-57] They are less related to the content of this dissertation, and will not be discussed in detail.

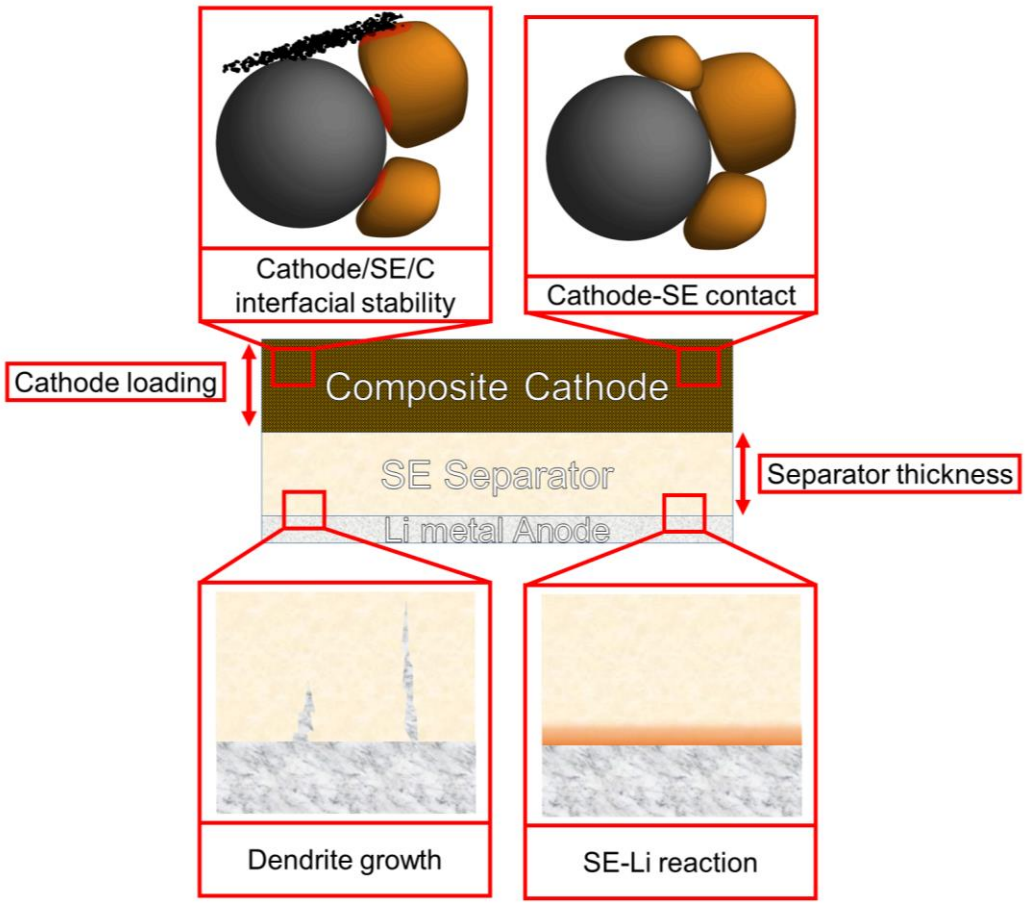

Figure 1.8: Schematic of major issues in SSB production and cycling.

1.3.5.1 Solid electrolyte chemical stability

During cycling, the SE in the SSB experiences different Li chemical potentials at various interfaces. For SSBs to achieve long-term stable cycling, the SE must be stable or form a passivation layer at these interfaces. The SE stability consists of two parts: the intrinsic stability and the reactivity with electrode materials.

The intrinsic stability of SE describes the chemical potential window (or the voltage window) within which the SE is thermodynamically stable. When the SE experiences a Li chemical potential lower than its stability window, usually at the cathode side, the SE can be oxidized, and Li can be extracted from the structure. When the chemical potential is higher than the SE stability window at the anode side, the SE can be reduced and decompose to Li-rich phases. Therefore, a SE must have a stable voltage window larger than the cell operating voltage window or have favorable decomposition products at the interfaces.

SE stability window can be determined both experimentally and computationally. Early experimental attempts to determine the SE stability window relied on the cyclic voltammetry (CV) method. The test cell usually consists of a SE pellet with two current collectors attached on both sides. By cycling the cell across a large voltage range, it is expected that decomposition of the SE can be observed by an increase in current. However, the limited contact area between the SE and the current collectors only allows a small amount of SE to decompose, resulting in a very small current change. This has caused many overestimations of the stability windows for many

conductors, including LGPS, Na_3PS_4, and LLZO.[37,58,59] A more accurate measurement can be done by mixing the SEs with electronic conductors such as carbon, which increases the SE decomposition amount and the current signal. Measurements done with such a method shows more reliable, but much reduced stability windows for a variety of SEs. For example, LGPS, which was initially believed to be stable against Li metal and stable up to 5 V, was shown to be reduced below 1.6 V against Li metal and oxidized above 2.7 V.[60] Computational methods have also been used to determine the SE windows. By constructing the relevant 0 K grand potential phase diagrams using DFT calculated energies, the stability of the SE under certain Li chemical potential range can be determined. The calculated voltage windows show good agreement with experimental results.[60-62] This computational approach allows for the high-throughput determination of many SE voltage windows, which can be seen in figure 1.9.

From figure 1.9, it is clear that the anion chemistry mostly determines the upper voltage limits of SEs. This is because the oxidation limit is determined by the highest occupied electron states, which are often the anion states. Among the different anion chemistries, fluorides exhibit the highest oxidation limit because of fluorine ion's high electronegativity. However, currently, there is no fluoride SE that has high ionic conductivities. Sulfide SEs, which have very high ionic conductivity, often cannot withstand voltage higher than 2.5 V. This leads to oxidation of SEs during cycling, which has been observed in many sulfide systems.[63,64] The sulfide SEs are also not stable at the anode side and start to decompose below 2 V. In comparison, some of the oxide SEs have a much wider voltage window. LLZO, for example, has a reduction limit close to Li metal and oxidation limit above 3 V.

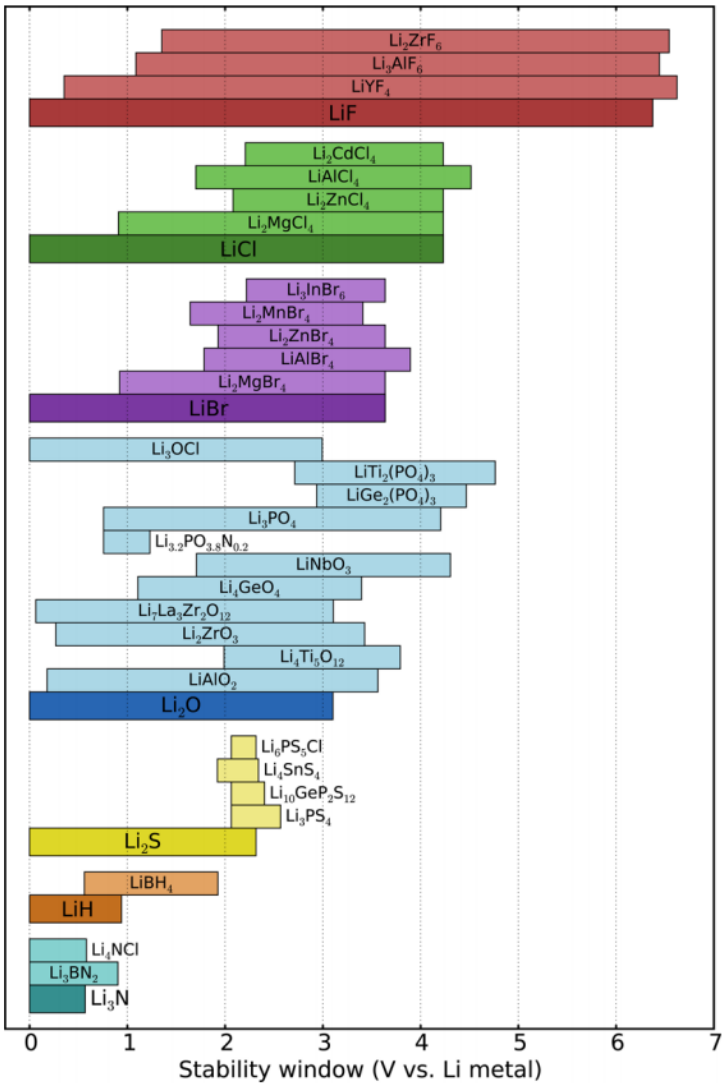

Figure 1.9: Electrochemical stability windows of various electrolyte materials grouped by anion.[62]

The other aspect of the SE chemical stability is the reactivity with the cathode material. In SSBs, the SE and cathode are in contact throughout the cycling process, and there is often a thermodynamic driving force for them to react at the interface. Sulfide SEs are particularly reactivity with common oxide cathode materials. Thiophosphate SEs can often take up oxygen from the oxide cathode to form the more stable phosphate compounds and transition metal sulfides.[62,65] This atomic inter-diffusion and interfacial layer formation have been experimental observed in $LiCoO_2$ and LPS system, and are shown to be the cause for the impedance increase during cycling.[66] Cathode coating has been widely used as a method to prevent the interfacial reaction between cathode and SE. Many coating materials, such as $LiNbO_3$,[67] $Li_4Ti_5O_{12}$,[68] Li_3BO_3,[69], and $Li_2O–ZrO_2$,[70] has been tested and show various effectiveness in preventing the interfacial reaction. It should be noted that the similar to the SEs, coating materials also have to have stability window higher than the cell operating window. Since the coating is thin, the ionic conductivity requirement for coating materials are less strict, and a recent high-throughput computational search has produced several promising coating material candidates.[71]

1.3.5.2 Mechanical issues in SSBs

By replacing the liquid electrolyte in LIBs with SEs, the ion transport within SEs and between SEs and cathode materials requires the crossing of solid particle boundaries, which requires mechanical contact between particles. Insufficient particle contact increases the interfacial resistance and cell overpotential, resulting in under-utilization of active materials. Forming and maintaining intimate contact between particles is one of the major challenges in SSBs.

Ensuring intimate particle contact is critical for SSB fabrication and highly dependent on the mechanical properties of the SEs. Mechanical pressing is the most common way to form the electrolyte pellet and the composite electrode in SSBs. This method is particularly suited for sulfide-based SEs because they have relatively low Young's modulus (~20 GPa) and harness (~2 GPa).[72,73] This favorable mechanical property allows the sulfide SE to undergo large deformation under 100-MPa-level pressure, forming intimate contact between particles.[74] Forming good particle-particle contact is much more difficult for the oxide-based SEs. Oxide SEs such as LLZO have very different mechanical properties from sulfide SEs, with large Young's modulus (~150 GPa) and hardness (~6 GPa).[75] This means they are less likely to deform under cold pressing, and their densification is aided with additional sintering step. However, the high-temperature sintering can promote undesired side reactions between the SE and the cathode, creating large interfacial resistance and high overpotential.[76,77]

Maintaining intimate particle contact during cycling is another mechanical challenge for SSBs. It is well-known that the common layered oxide cathodes exhibit large volume change during cycling.[78,79] Such volume change cannot be fully accommodated by the elastic deformation of the surrounding SEs and can cause contact loss between cathode and SE during cycling.

1.3.5.3 Practical issues in SSB fabrication

Figure 1.5 shows the impact of cathode loading and separator thickness on the energy density of SSBs. Developing fabrication methods to allow increased cathode loading and reduced the separator thickness is critical.

Current cathode loading of 60–70 wt% significantly limits the energy density of SSBs.[35,70,80] To increase the cathode loading, the amount of SE and carbon in the cathode composite need to be reduced while maintaining the ionic and electronic pathway for the active material. This requires further optimization of the composite cathode morphology (*i.e.*, how the cathode, SE, carbon, and possibly binder are distributed). Several studies have separately shown that the cathode active material and SE particle sizes affect the morphology of the cold-pressed cathode composite and the full-cell performance.[81-84] Smaller SE particle size is expected to form better percolation networks in the composite cathode. Chapter 4 will explore in detail this particle size ratio effect on the cathode loading.

The current separator thickness in SSBs, which are several hundreds of microns, is much thicker than that in traditional LIBs, which are often thinner than 10 μm. To achieve a competitive energy density in SSBs, a thin separator (< 50 μm) is needed. Although several thin-film fabrication methods have been used to produce thin SE separators at the lab scale, including radio-frequency magnetron sputtering[85-87], pulsed laser deposition[88-90], and atomic layer deposition[91-93], such methods cannot be applied to large-scale production because of the high cost and low throughput. Thin SE separators can also be made by tape casting, which is a scalable process and widely used in current LIB production. Less-than-100-μm-thick tape-casted SE films have been demonstrated for both oxide and sulfide SEs. [94,95] Tape-casted SE film may require polymer

binders or scaffolds during slurry casting to improve their mechanical strength, which will slightly lower the ionic conductivity of the separator.[80,95]

1.4 Dissertation overview

This dissertation explores the chemical and mechanical interfacial stability issues in the SSBs and methods to improve their energy density. Chapter 2 focuses on chemical stability in SSBs. Combined theory and experimental results show the highly reactive nature of sulfide SEs during SSB cycling and highlight the importance of interfacial engineering in SSBs. Chapter 3 characterizes the mechanical degradation during SSB cycling. Reconstructed 3D tomography data show the severity of the contact loss between SE and cathode after long-term cycling and its effect on battery performance. Chapter 4 proposes a method to increase the cathode loading in SSBs. Both experimental and computational results suggest that optimizing the particle size ratio of the SE and cathode active materials can improve the cathode loading and the full cell energy density.

Chapter 2 - Compatibility Issues between Electrodes and Electrolytes in Solid-State Batteries

2.1 Foreword

The work presented in this chapter was published by Y. Tian, T. Shi, W. D. Richards, J. Li, J. C. Kim, S. H. Bo, G. Ceder, in Energy & Environmental Science, vol. 10, article number 1150 (2017), and is reproduced here with the permission of co-authors.

2.2 Abstract

Remarkable success has been achieved in the discovery of ceramic alkali superionic conductors as electrolytes in solid-state batteries; however, obtaining a stable interface between these electrolytes and electrodes is difficult. Only limited studies on the compatibility between electrodes and solid electrolytes have been reported, partially because of the need for expensive instrumentation and special cell designs. Without simple yet powerful tools, these compatibility issues cannot be systematically investigated, thus hindering the generalization of design rules for the integration of solid-state battery components. Herein, we present a methodology that combines density functional theory calculations and simple experimental techniques such as X-ray diffraction, simultaneous differential scanning calorimetry and thermal gravimetric analysis, and electrochemistry to efficiently screen the compatibility of numerous electrode/electrolyte pairs. We systemically distinguish between the electrochemical stability of the solid-state conductor, which is relevant wherever the electrolyte contacts an electron pathway, and the electrochemical stability of the electrode/electrolyte interfaces. For the solid electrolyte, we are able to computationally derive an absolute thermodynamic stability voltage window, which is small for Na_3PS_4 and Na_3PSe_4, and a larger voltage window that can be kinetically stabilized. The experimental stability, when measured with reliable techniques, falls between these thermodynamic and kinetic limits. Employing a Na solid-state system as an example, we demonstrate the efficiency of our method by finding the most stable system ($NaCrO_2$|Na_3PS_4|Na–Sn) within a selected chemical space (more than 20 different combinations of electrodes and electrolytes). Relevant selection criteria for the cathode, electrolyte, and anode in solid-state batteries are also derived from this study. The current method not only provides an essential guide for integrating all-solid-state battery components but can also significantly accelerate the expansion of the electrolyte/electrode compatibility data.

2.3 Introduction

Pioneered by the study of microbatteries, solid-state batteries have recently attracted significant attention[96-98] because of their advantages compared with conventional batteries employing liquid electrolytes. The use of a ceramic solid-state electrolyte not only eliminates the safety hazards associated with flammable organic liquid electrolytes but also opens up the possibility of using novel high-capacity electrodes, such as sulfur cathodes and Na or Li metal anodes. These high-capacity electrodes have proven problematic in liquid systems, partially because of reactivity and/or dissolution with the electrolyte, and poor metal deposition morphology in liquid electrolytes, often leading to dendrite growth[96,99]. When built with stable interfaces, solid state batteries can also minimize the side reactions that occur in liquid electrolyte batteries, resulting in high coulombic efficiency and ultra-long cycle life[100,101]. Recently, all-solid-state batteries utilizing sulfide-based superionic conductors have even achieved superior performance in terms of power

density compared with traditional Li-ion batteries (LIBs) thanks to the discovery of lithium superionic conductors with ionic conductivities of 25 mS cm^{-1}, one magnitude higher than those of state-of-art liquid electrolytes[35,102-105].

The main research focus in all-solid-state batteries has been on finding fast ionic conductors, which has resulted in many newly discovered conductors with ionic conductivities close to or even surpassing those of liquid electrolytes. Given that the basic structural and chemical features for high alkali ion conductivity are now reasonably well understood[39,106], it is likely even better conductors will be developed. In Li-ion systems, some NASICON-, perovskite- and garnet-type oxides exhibit room-temperature (RT) conductivities of approximately 1 mS cm^{-1} or higher but suffer from poor contact with electrodes because of difficulties in pellet pressing and sintering[53,98,107-110]. Sulfide-based solid electrolytes such as $Li_{10}GeP_2S_{12}$ and Li_2S-P_2S_5 exhibit conductivities greater than 10 mS cm^{-1} [35,58,106,111-113], but generally have limited voltage stability windows, which makes electrode selection a difficult task[114]. In some cases, an electrode coating is applied to mitigate this issue; however, the coating process is often imperfect or difficult to scale[68,70,115,116]. In parallel to the developments in solid-state lithium conductors, promising fast Na-ion conductors have also been recently discovered and applied in Na-ion batteries (NIBs)[103,104,117-119]. However, it is similarly challenging to find a Na conductor with all the desired properties for all-solid-state battery applications, namely high conductivity, compatibility with both anodes and cathodes, processability, and good mechanical properties.

Clearly, the bottleneck of all-solid-state battery development is no longer maximizing the ionic conductivity of solid electrolytes but has instead shifted toward the integration of the solid electrolyte and electrodes. This challenge of cell integration is largely associated with maintaining chemical and mechanical stabilities between the electrodes and electrolytes during battery operation, both of which by itself is a major obstacle for solid-state battery development. The compatibility of electrodes and electrolytes is largely determined by the properties of the electrode/electrolyte interface. A good interface between a solid electrolyte and electrode requires fast ion transport, maximum contact area, and chemical stability during cycling. Indeed, in detailed studies, previously claimed stable electrolyte/electrode pairs have often found to degrade through chemical or electrochemical reactions[106,109,114,120,121].

In this work, we focus on the chemical aspect of the cell integration challenge, and present a methodology that combines computational predictions with fast, simple experimental tests that can efficiently screen the compatibility of numerous electrode/electrolyte pairs. We use layered Na transition metal oxide cathodes ($NaMO_2$, M = Cr, Mn, Fe, Co, Ni)[122-126], Na metal or Na–Sn alloy anodes[127,128], and two recently reported solid electrolytes with high ionic conductivities (Na_3PS_4[113] and Na_3PSe_4[102]) as examples to demonstrate our methodology. The Na ion system was selected for several reasons. First, NIBs have attracted significant attention because of the lower cost and greater abundance of their materials compared with those used in LIBs[129-131]. Second, the Na system provides a wider chemical space to explore for cathode materials, enabling synthesis and cycling of many electrode materials for which the Li analogues are electrochemically inactive, such as layered $NaFeO_2$[124,129,131,132]. Finally, compatibility issues have not been systematically studied in the Na solid-state system, which provides us with an opportunity to demonstrate the efficiency of our screening method when applied to unknown systems.

In the following discussion, we will start by introducing the compatibility issues facing solid-state batteries as well as the methodology to examine these issues. Then, the results with respect

to the electrochemical stability of the electrolytes and chemical compatibility between the electrodes and electrolytes will be presented. The manuscript concludes with a discussion of the (1) main chemical challenge associated with utilizing an oxide cathode and thiophosphate solid electrolyte, (2) importance of understanding both the chemical and electrochemical decomposition pathways of electrolytes and electrode/electrolyte composites, and (3) role of thermodynamics and kinetics in these reactions. Possible strategies and selection criteria to integrate all-solid-state battery components will also be proposed.

2.4 Methodology

Three factors mainly govern the choice of components for all-solid-state batteries. Taken Na solid-state system as an example, the three factors are graphically illustrated in Figure 2.1 and are discussed in detail below:

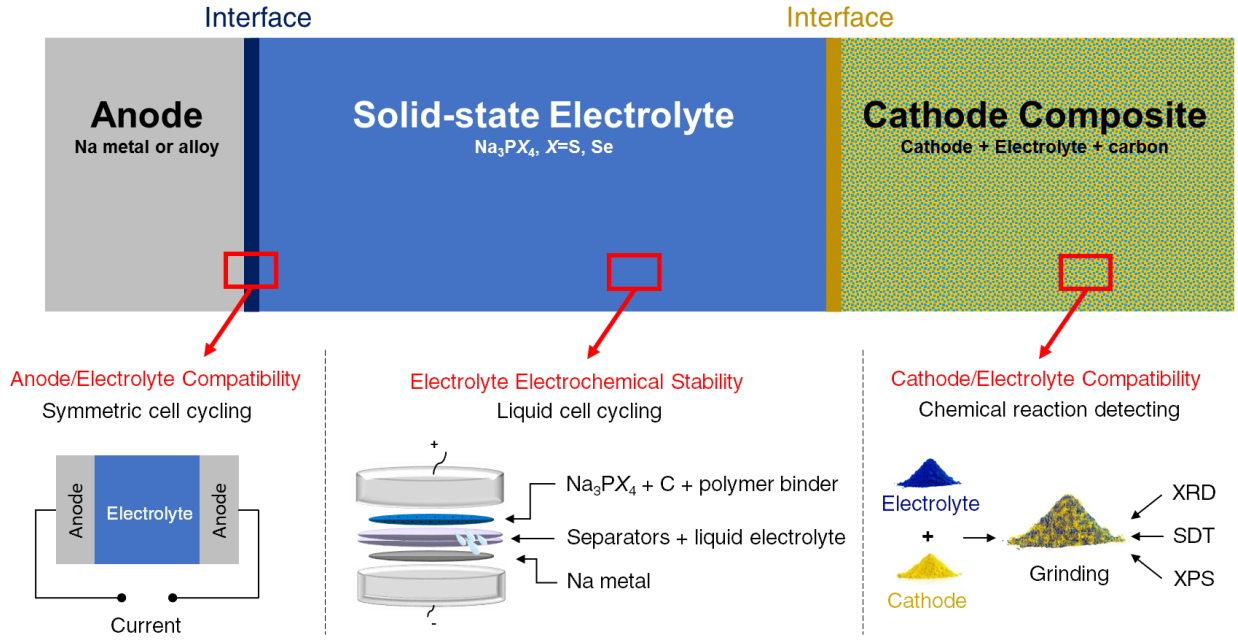

Figure 2.1: Problems addressed and methods used. Summary of compatibility and stability problems in all-solid-state batteries and the experimental methods for assessing these issues. The sodium system was selected as a specific example utilizing the methods.

1) *Voltage window of the solid electrolyte.* The voltage window of the electrolyte determines the cycling range and selection of both electrodes and should thus be considered and determined first.

   Prior experimental insights regarding the electrochemical stability of solid-state electrolytes may require reinterpretation. Determination of the stable electrochemical window of a solid electrolyte has been traditionally performed using cyclic voltammetry (CV) [37,46,58,133]. In this method, the solid electrolyte is pressed into pellets and cycled with Li or Na metal on one side and an inert metal (such as stainless steel, Au, or Pt) on the other side. However, CV often overestimates the electrochemical stability limits of electrolytes. The bulk electrolyte is likely not in equilibrium during a CV scan because of the fast scanning rate and/or imperfect contact with the metal electrodes. Furthermore, because of the poor electronic conductivity of solid electrolytes, the overall decomposition

reaction is often slow or limited to a thin region at the interface, thereby limiting the degradation current that can be observed in a CV scan. The situation is very different in a real cell configuration, where the electrolyte is mixed with carbon and the cathode material, providing a facile electron transfer pathway that promotes electrolyte redox reactions. Finally, the relatively small decomposition current detected by the CV method (sometimes less than 1 μA) is difficult to notice compared with the large current created by metal deposition/stripping at low voltage and is often ignored in the CV method. However, this small current could have a catastrophic effect on the long-term cycling of the full cell. Indeed, solid electrolytes previously claimed to be stable based on CV scans[37] were later upon more detailed investigation, found to be reactive at typical anode and cathode voltages[60], in agreement with theoretical predictions[134,135].

Other electrochemical techniques, such as polarization experiments, should be complemented with CV methods to determine the stability window of the solid electrolyte more accurately. In such experiment, the electrolyte is made into electrode and polarized to a given potential or with a constant current. The electrolyte is considered stable at such potential if the capacity delivered below (or above) this potential is close to zero during a galvanostatic or potentiostatic charge (or discharge). In our work, the stability windows of selected electrolytes (Na_3PS_4 and Na_3PSe_4) were first computed using density functional theory (DFT) calculations[114]. The results were then compared with experimental results obtained from galvanostatic charging/discharging. A similar method was recently employed to evaluate the electrochemical stability windows of $Li_7La_3Zr_2O_{12}$ garnet and $Li_{10}GeP_2S_{12}$, where the DFT computed and experimentally determined stability windows were in excellent agreement[60]. The synthesized solid electrolytes were ground into fine powders and then mixed with carbon and polymer binders to form film-type working electrodes, which were assembled in Swagelok cells with a liquid electrolyte against Na metal. By slowly cycling this cell, the voltage experienced by the bulk electrolyte materials is much better represented by the cell voltage, and a more accurate estimation of the stability window of the materials can be provided. The corresponding charge (or discharge) capacities also indicate whether the electrolyte decomposition is self-limiting. A self-limiting decomposition reaction can be beneficial in widening the electrochemical stability of the electrolyte depending on the physical properties (e.g., ionic and electronic conductivities) of the decomposition products.

2) *Possible reaction between cathode and solid electrolyte.* Absolute stability between the cathode and electrolyte is difficult to achieve, and the products of the reaction between the cathode and solid electrolyte can form an interfacial layer between the two. Depending on its properties, this interfacial layer can be detrimental or beneficial to the ionic transport between the two components. A good interface between the electrode and electrolyte must be self-passivating while still being permeable to the working ions.

   Based on this information, we tested the compatibility of electrodes and electrolytes by mixing the electrolyte and electrode powders at room temperature. Any bulk change detectable by X-ray diffraction (XRD) indicates that the selected electrolyte and electrode materials are incompatible. The possible reactions between electrodes and electrolytes at elevated temperatures were also evaluated using simultaneous differential scanning calorimetry and thermal gravimetric analysis (SDT) and XRD to determine the onset temperature of reaction and corresponding reaction products. Comparison of these results

with the DFT-computed thermodynamic reaction products enabled us to assess the role of kinetics in the electrode/electrolyte reactions, providing additional mechanistic insights.
Besides testing the reaction of the electrolyte with the as-synthesized cathode, compatibility with the charged cathode at high voltages is also important. At higher potential the strong oxidative power of the charged cathode will likely promote the electrolyte decomposition for chalcogenide systems. This chemical compatibility, however, has not yet been systematically investigated.
To investigate the aforementioned issue, partially charged cathodes were prepared through chemical oxidation with highly concentrated iodine in acetonitrile (CH_3CN), resulting in cathode powders equivalent to being charged to approximately 3.7 V against Na metal[136,137]. The reactions between the charged cathodes and electrolytes were then studied in a similar manner as discussed above.

3) *Possible reaction between anode and solid electrolyte.* The compatibility between the anode and electrolyte was examined by cycling anode/electrolyte/anode symmetric cells. If the anode and electrolyte react to form a poorly ionic conductive interfacial layer, the cell potential will increase as the reaction progresses. To prevent possible potential increase due to the mechanical loss of contact, a specially designed pressure cell is used to ensure good contact between electrolyte and electrodes during cycling. Therefore, an increase in the charge and discharge voltages during galvanostatic cycling often signifies an unstable interface between the anode and electrolyte.

2.5 Results

I. Electrolyte electrochemical stability

The calculated voltage stability window and decomposition products of Na_3PS_4 and Na_3PSe_4 are shown in Figure 2.2(a) and 2.2(b), respectively. These figures indicate which products the conductor converts into when Na is supplied and extracted at a given potential. The *x*-axis represents the capacity generated when these decomposition reactions occur per gram of conductor consumed. The results in Figure 2.2(a) indicate that Na_3PS_4 is electrochemically only stable from 1.55 to 2.25 V against Na metal. Below 1.55 V, Na_3PS_4 can be reduced and converted into Na_2S and other Na–P compounds. Above 2.25 V, in contrast, Na is extracted from Na_3PS_4, leading to decomposition into Na-deficient phases such as P_2S_7 and S. Similarly, according to Figure 2.2(b), Na_3PSe_4 is stable from 1.80 to 2.15 V against Na metal and decomposes into Na_2Se and other Na–P compounds below 1.80 V and Na-deficient phases such as PSe and Se above 2.15 V. Of note is that our calculated stability window is much narrower than experimental values claimed from CV measurements, but in agreement with other theory work.[113,138] This discrepancy results either from reaction kinetics, which would delay the onset of decomposition, or intrinsic limitations of the CV measurements. Based on our experimental results, as will be discussed below, the latter is more likely.

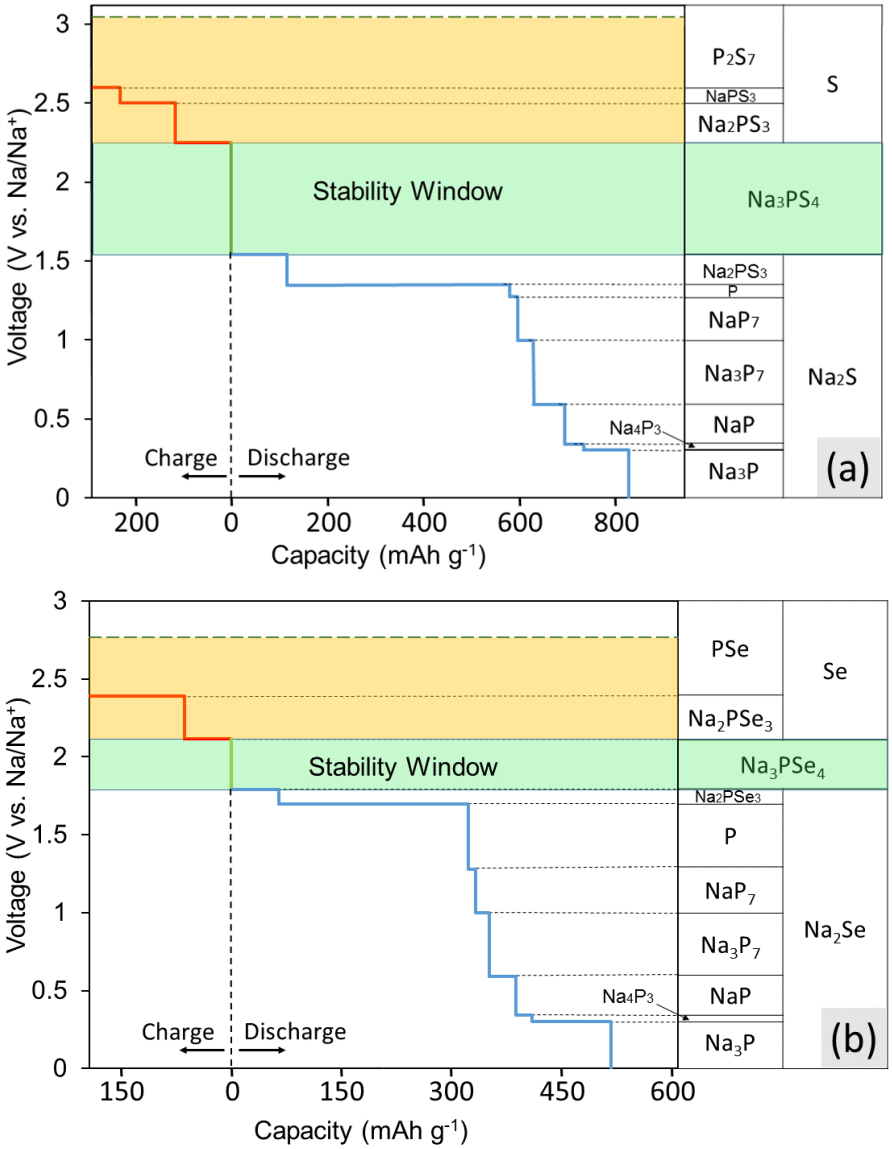

Figure 2.2: Computed voltage windows for the solid electrolytes. Calculated stability window and decomposition products for (a) Na_3PS_4 and (b) Na_3PSe_4. The green shaded region is the thermodynamically stable voltage window, and the yellow shaded region is the additional voltage range that could be kinetically stabilized.

These calculated voltages assume that diffusion kinetics are not limiting, and thus provide a lower bound of the Na extraction voltage. To investigate the upper limiting case, the voltage for topotactic desodiation of the conductors was calculated. The calculated results indicate that Na_3PS_4 and Na_3PSe_4 lose Na at 3.05 V and 2.75 V, respectively. We found furthermore that the voltage for subsequent extraction of Na is lower. Note that these two values indeed provide absolute upper bound for the Na_3PX_4 stability window, as the Na-ion and electron extraction are unlikely to be kinetically limited due to the faster Na-ion mobility in these materials.

To experimentally determine the electrochemical stability window of the electrolyte materials, Na_3PX_4 (X = S, Se) cathodes were "charged" (oxidized) or "discharged" (reduced) at constant current between 0.5 V to 4.0 V. Upon charging, Na_3PS_4 exhibited negligible capacity at the

beginning of charging (Figure 2.3(a)). However, as the voltage increased above ~2.65 V, a voltage dip followed by a substantial capacity delivered at approximately 2.7 V was observed. The initial voltage rise is likely due to a nucleation or other activation process, needed to generate the decomposition products of Na_3PS_4. Therefore, we can assume that the voltage dip at approximately 2.5 V is the onset decomposition voltage of Na_3PS_4. Approximately 2.5 Na per f.u. can be extracted from Na_3PS_4 until the cut-off voltage of 4.0 V is reached. The "fully charged" Na_3PS_4 cathode composite turns completely amorphous as observed in XRD (Figure 2.3(c)).

During the discharging process, a sloping voltage region is first observed at approximately 1.8 V, suggesting that Na_3PS_4 is likely electrochemically unstable below this voltage. Interestingly, fully discharging to the cut-off voltage of 0.5 V only results in a very low capacity (i.e., 0.08 Na intercalation per formula), and the "fully discharged" Na_3PS_4 shows almost no structural change compared with the pristine cathode composite (Figure 2.3(c)). One possible reason is that Na_3PS_4 might be passivated by the decomposition products upon discharging. This passivating process may prevent further decomposition of Na_3PS_4 and widens the apparent reduction limit of Na_3PS_4. Based on the discussion above, we conclude that the electrochemical stability window of Na_3PS_4 lies within the range 1.8–2.5 V, which is in much better agreement with the DFT predictions than reported CV measurements, further underscoring the limited reliability of CV techniques to determine the stability limits of solid electrolytes.

Similarly, the stability window of Na_3PSe_4 was experimentally determined by charging and discharging the Na_3PSe_4 (mixed with carbon) cathode composite. During the charging process, the decomposition of Na_3PSe_4 starts at approximately 2.33 V, where a substantial capacity of 110 mAh/g or 1.5 Na per formula was delivered in the sloping voltage region of 2.33–2.50 V. Based on DFT calculations, this decomposition process is most likely associated with the production of Se and Na_2PSe_3. The decomposition products of the "fully charged" Na_3PSe_4 was experimentally determined by both *ex situ* and *in situ* XRD. In the *ex situ* XRD results presented in Figure 2.3(d), new Se peaks are observed after the Na_3PSe_4 cathode composite is "fully charged", which is in almost perfect agreement with the DFT calculations; in the *in situ* XRD results (Figure 2.4), Se was detected to grow in quantity at the expense of Na_3PSe_4, although the other predicted product (i.e., Na_2PSe_3) is not observed. We suspect that Na_2PSe_3 might be present as an amorphous phase. The prolonged voltage plateau at approximately 2.50 V might be a result of the redox shuttle effect caused by dissolved polyselenide molecules[139,140], and the voltage fluctuation could be related to the reaction of the Na metal with the dissolved decomposition products. When the cell was opened after the charging process, the separators and Na metal had both become brown, indirectly supporting the above explanation of the voltage fluctuation. During the discharge process, a noticeable redox reaction occurs at approximately 2.10 V. Based on DFT calculations, this process is associated with the production of Na_2Se and Na_2PSe_3. Overall, the stability window of Na_3PSe_4 was determined to be 2.10–2.35 V, which is again closer to our theoretical predictions than to the CV measurement (Table 2.5).

We note the experimentally determined reduction decomposition voltages are higher than the computational results for both Na_3PS_4 and Na_3PSe_4. This can be attributed to the presence of a small amount of the sulfur or selenium in the as-prepared Na_3PS_4 or Na_3PSe_4 samples. The reduction of sulfur or selenium occurs at approximately 2 V[141], which can be taken to explain the small capacity observed experimentally. Alternatively, the capacity observed near 2 V is due to Na intercalation into the conductors. Because the 2 V process may not be inherently related to the conductors themselves, the experimentally determined reduction voltages should be taken as tentative.

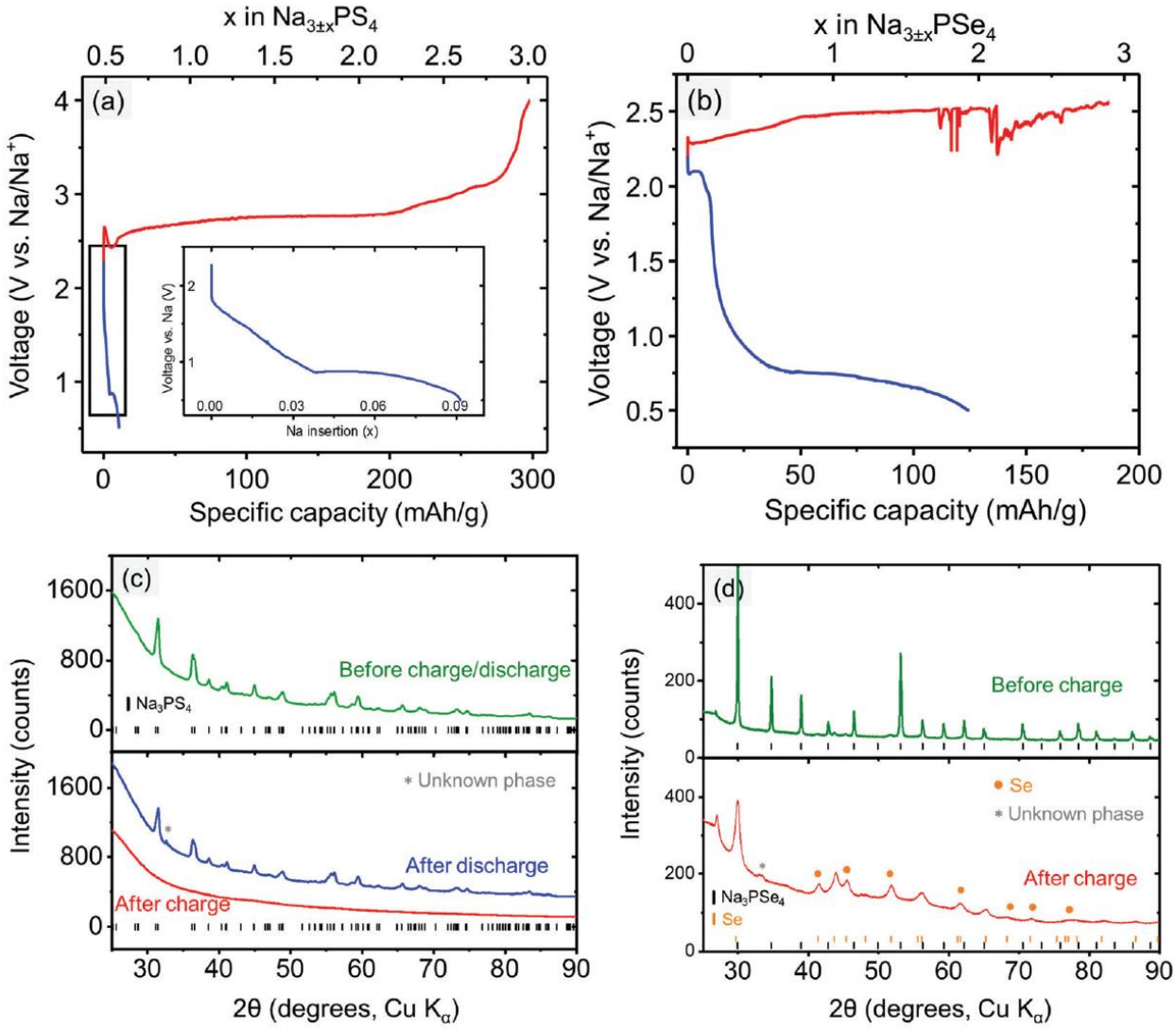

Figure 2.3: Experimental voltage windows for the solid electrolytes. Electrochemical cycling of the Na_3PX_4 (mixed with carbon) cathode composite at constant current (2.604 mA/g for Na_3PS_4 and 2.404 mA/g for Na_3PSe_4), showing the stability window of (a) Na_3PS_4 and (b) Na_3PSe_4. Diffraction patterns of the (c) Na_3PS_4 cathode composite before and after being fully charged/discharged and (d) Na_3PSe_4 cathode composite before and after being fully charged.

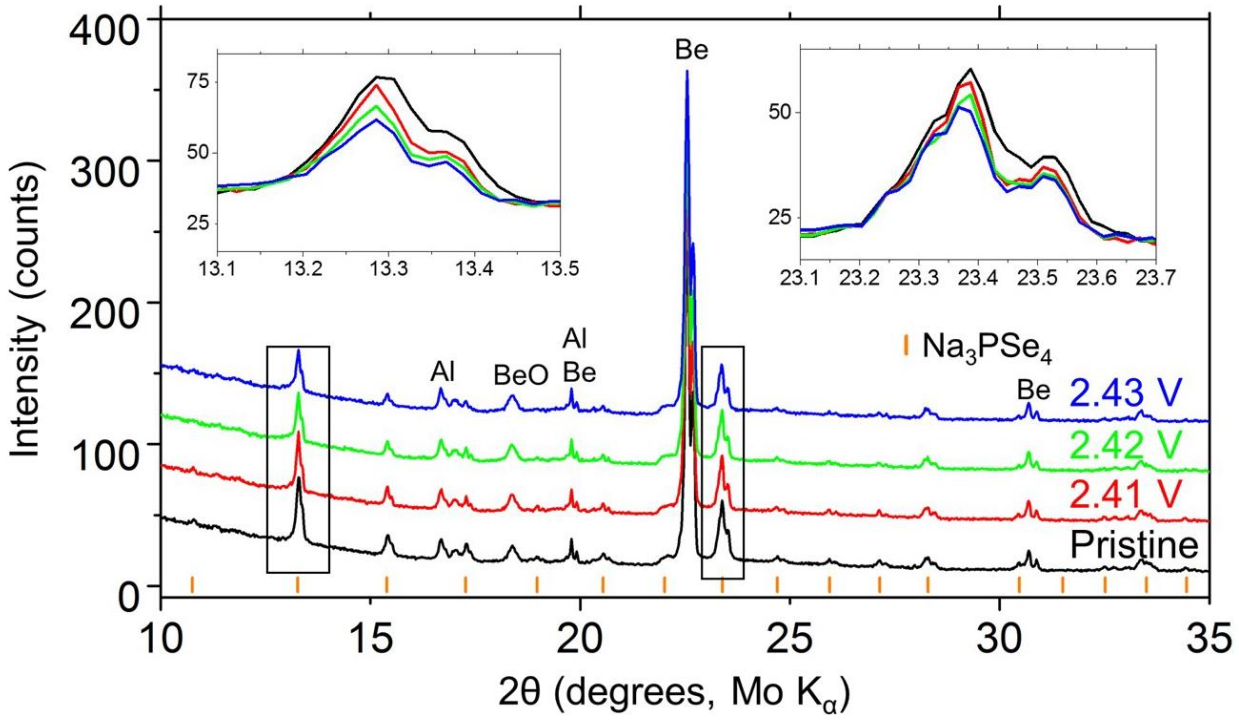

Figure 2.4: Evidence of solid electrolyte decomposition. *In situ* XRD patterns of Na_3PSe_4 cathode composite during the charging process. The insets show the intensity change, demonstrating the growth of Se at the expense of Na_3PSe_4.

II. Compatibility between cathode and electrolyte

1) DFT-predicted products of cathode/electrolyte reactions

To obtain an estimate of the chemical stability of each interface, we used DFT calculations to calculate the maximum mixing energy of the cathode/electrolyte compositions using methodology similar to that of previous work[114]. The maximum mixing energies and their corresponding reaction products, were calculated for all combinations of the cathodes ($NaMO_2$, M = Cr, Mn, Fe, Co, Ni) and electrolytes (Na_3PX_4, X = S, Se). To show the compatibility at different status of charge, this procedure was repeated for partially desodiated cathodes $Na_{0.5}MO_2$. The calculation results, summarized in Table 2.1, indicate that none of the oxide and chalcogenide pairs are chemically absolutely stable. Because there are many possible reactions that result in similar mixing energies, and because which one actually forms depends on both thermodynamic and kinetic factors, a full list of the reaction products along the entire tie line is summarized in Table 2.2. Because these reactions require significant bulk diffusion, they can be expected to localize to a small interfacial region unless aided by high temperatures.

The reactions between the Na_xMO_2 (x = 1.0 pristine or x = 0.5 desodiated) cathode and Na_3PX_4 electrolyte can be broadly categorized into two classes (often occurring together):

1) Anion exchange reactions. For instance, mixing $NaCrO_2$ and Na_3PX_4 (X = S, Se) can produce $NaCrX_2$ (X = S, Se) and Na_3PO_4. The exchange of some oxygen from the cathode with the chalcogenide from the electrolyte to form Na_3PO_4 and metal-chalcogenides is favorable for all the systems we investigated.

2) Complex redox reactions involving multiple phases with significant structural rearrangements. For example, mixing $NaNiO_2$ and Na_3PX_4 (X = S, Se) leads to the production of more than three decomposition products and involves transition metal reduction.

Table 2.1: DFT calculations for the products of the reaction between Na_xMO_2 (x = 0.5 or 1.0) and Na_3PX_4.

		$NaCrO_2$	$NaMnO_2$	$NaFeO_2$	$NaCoO_2$	$NaNiO_2$
Na_3PS_4	Reaction products	Na_3PO_4 $NaCrS_2$	Na_3PO_4 $NaMnS_2$*	Na_3PO_4 $Na_{3/2}(FeS_2)$ FeS_2	Na_3PO_4 $NaCoS_2$	Na_3PO_4 Na_2S Na_2SO_4 $Na_2Ni_3S_4$*
	Reaction energy (eV/atom)	-0.0970	-0.2649	-0.2652	-0.3516	-0.4394
Na_3PSe_4	Reaction products	Na_3PO_4 $NaCrSe_2$	Na_3PO_4 $NaMnSe_2$*	Na_3PO_4 Na_2Se $FeSe_2$ $FeSe$	Na_3PO_4 Na_2Se Co_9Se_8 Co_5Se_8*	Na_3PO_4 Na_2Se Ni_5Se_8* Ni_3Se_4
	Reaction energy (eV/atom)	-0.1325	-0.2138	-0.2615	-0.3695	-0.4541
		$Na_{0.5}CrO_2$	$Na_{0.5}MnO_2$	$Na_{0.5}FeO_2$	$Na_{0.5}CoO_2$	$Na_{0.5}NiO_2$
Na_3PS_4	Reaction products	Na_3PO_4 $NaCrS_2$ S Cr_2O_3	Na_3PO_4 Na_2SO_4 MnS $Na_4Mn_3S_5$*	Na_3PO_4 $Na_{3/2}(FeS_2)$ FeS_2	Na_3PO_4 Na_2S Na_2SO_4 Co_9S_8	Na_3PO_4 Na_2SO_4 Ni_9S_8 Ni_3S_2
	Reaction energy (eV/atom)	-0.1429	-0.3156	-0.3514	-0.4376	-0.5580
Na_3PSe_4	Reaction products	Na_3PO_4 $Na_{1/3}(CrSe_2)$ $Na_{2/3}(CrSe_2)$	Na_3PO_4 $Na_{1/3}(MnSe_2)Na_6MnSe_4$ MnO	Na_3PO_4 Na_2Se $FeSe_2$ $FeSe$	Na_3PO_4 Na_2Se Co_5Se_8* $CoSe_2$	Na_3PO_4 Na_2Se Ni_5Se_8* $NiSe_2$
	Reaction energy (eV/atom)	-0.1985	-0.2848	-0.3730	-0.4558	-0.5463

* denotes compounds which are created through chemical substitution of compounds which are present in the Inorganic Crystal Structure Database (ICSD)

Table 2.2: DFT calculations for all possible products of the reaction between Na_xMO_2 (x = 0.5 or 1.0) and Na_3PX_4

	$NaCrO_2$	$NaMnO_2$	$NaFeO_2$	$NaCoO_2$	$NaNiO_2$
Na_3PS_4	Na_3PO_4, Na_3PS_4, $NaCrO_2$, Na_3PSO_3, Na_3PS_3O, $Na_3P(SO)_2$, $NaCrS_2$	Na_2SO_4, Na_3PO_4, Na_3PS_4, Na_3PSO_3, Na_3PS_3O, $NaMnS_2$, MnS, MnO, $NaMnO_2$, $Na_3P(SO)_2$, Na_2MnS_2, $Na_4Mn_3S_5$	Na_2SO_4, Na_3PO_4, Na_3PS_4, $NaFeO_2$, Na_3PSO_3, Na_3PS_3O, FeS_2, Fe_3O_4, $Na_3P(SO)_2$, $Na_3(FeS_2)_2$	Na_2SO_4, Co, Na_3PO_4, Na_3PS_4, $NaCoO_2$, Na_3CoO_3, Co_9S_8, $NaCoS_2$, Na_2S, Na_3PSO_3, Na_3PS_3O, $Na_3P(SO)_2$	Ni_3S_4, Ni_3S_2, Na_2SO_4, $Na_6S_2O_9$, Na_3PO_4, Ni, Na_3PS_4, Na_3PSO_3, Na_2S, NaS, NiO, Na_3PS_3O, Na_4NiO_3, $Na_3P(SO)_2$, $Na_2Ni_3S_4$
Na_3PSe_4	Na_3PSe_4, Cr_2O_3, Na_3PO_4, $Na_4P_2O_7$, Na_3PSeO_3, $NaCrO_2$, $NaCrSe_2$, Na_3PSe_3O, Na_2Se	Na_3PSe_4, Na_2MnSe_3, $NaMnO_2$, NaSe, Mn_3O_4, MnO, $NaMnPO_4$, Na_2Se, Na_3PO_4	Na_3PSe_4, $FeSe_2$, FeSe, Na_3PSe_3O, Na_3PO_4, $Na_4P_2O_7$, Fe_2O_3, $NaFeO_2$, Na_3PSeO_3, Fe_2P, FeP, Fe_3O_4, FeO, Na_2Se	Na_3PSe_4, Na_3PSe_3O, $CoSe_2$, $Na_4P_2O_7$, Co_9Se_8, $NaCoO_2$, $NaCo_7O_{11}$, Na_3PSeO_3, Co_2P, Co_3O_4, CoO, Co_5Se_8, Na_2Se, Na_3PO_4	Na_3PSe_4, Ni_2P, Ni_3Se_4, NiO, $Na_4P_2O_7$, $Ni_{12}P_5$, Na_5NiO_4, Na_3PSeO_3, Ni_5Se_8, Na_2SeO_3, $NiSe_2$, NaSe, Na_3PSe_3O, Na_2Se, Na_3PO_4

(Continued)

	$Na_{0.5}CrO_2$	$Na_{0.5}MnO_2$	$Na_{0.5}FeO_2$	$Na_{0.5}CoO_2$	$Na_{0.5}NiO_2$
Na_3PS_4	Na_2SO_4, Cr_2O_3, Na_3PO_4, $Na_6Cr(SO_4)_4$, Na_3PS_4, $Na_4P_2O_7$, $NaCrO_2$, $Na_3Cr(PO_4)_2$, Na_2PS_3, Na_3PSO_3, $Na_3P(SO)_2$, S, $Na_{2/3}CrS_2$, $Na_3Cr_2(PS_4)_3$, Na_3PS_3O, $NaCrS_2$	Na_2SO_4, $NaMnO_2$, $NaMnS_2$, Na_3PS_4, MnS, Mn_3S_4, Na_3PS_3O, Na_3PSO_3, MnO, $Na_3P(SO)_2$, Na_2MnS_2, $Na_4Mn_3S_5$, $Na_{1/3}MnS_2$, $Na_{2/3}MnS_2$, Na_3PO4	Na_2SO_4, Na_3PO_4, Na_3PS_4, $NaFeO_2$, Na_3PSO_3, Na_3PS_3O, FeS_2, Fe_3O_4, $Na_3P(SO)_2$, $Na_{3/2}FeS_2$	Na_2SO_4, Co, Na_3PO_4, Na_3PS_4, $NaCoO_2$, Co_9S_8, $NaCoS_2$, Na_2S, Na_3PSO_3, Na_3PS_3O, CoS_2, $Na_3P(SO)_2$, $Na_{2/3}CoS_2$, CoO	Na_2SO_4, $NaNiPO_4$, $Na_6S_2O_9$, Na_3PO_4, Ni_3S_4, Ni, Na_3PS_4, NaS, Na_2S, Na_3PSO_3, NaS_2, Ni_9S_8, Ni_3S_2, $Na_3P(SO)_2$, Na_3PS_3O, $Na_2Ni_3S_4$, NiO
Na_3PSe_4	$Na_2CrP_2O_7$, Cr_2O_3, Na_3PO_4, $Na_4P_2O_7$, Na_3PSe_4, Na_2SeO_3, $NaCrSe_2$, $Na_3Cr(PO_4)_2$, $NaCrO_2$, $NaSe_2$, NaSe, Na_3PSe_3O, Se	$MnSe_2$, Na_3PSe_4, Na_2MnSe_3, $NaMnO_2$, MnO, $NaSe_2$, Mn_3O_4, Na_2SeO_3, NaSe, $NaMnPO_4$, Na_3PO_4	Na_3PSe_4, $FeSe_2$, FeSe, Na_3PSe_3O, Na_3PO_4, $Na_4P_2O_7$, Fe_2O_3, FeO, Na_3PSeO_3, $NaSe_2$, Fe_2P, FeP, Na_2SeO_3, $NaFeO_2$, NaSe, Fe_3O_4, Na_2Se	Na_3PSe_4, Na_3PSe_3O, $CoSe_2$, $Na_4P_2O_7$, $NaCo_7O_{11}$, Na_3PSeO_3, Na_2SeO_3, Co_3O_4, Co_2P, Na_2Se, Co_5Se_8, CoO, Na_3PO_4	Na_3PSe_4, Ni_2P, Na_3PSe_3O, NiO, $Na_4P_2O_7$, Na_2SeO_4, Na_4SeO_5, Na_3PSeO_3, Na_2SeO_3, Ni_5Se_8, $NiSe_2$, NaSe, $Ni_{12}P_5$, Na_2Se, Na_3PO4

2) Experimental verification of the reactions between the pristine cathode and electrolyte

The compatibility of the pristine cathode and electrolyte was first investigated at room temperature. Diffraction patterns before and after mixing the selected electrode and electrolyte materials at room temperature are shown in Figure 2.5. Figure 2.5 (a-d) shows that the diffraction patterns of $NaCrO_2$ and $NaMnO_2$ mixed with Na_3PS_4 or Na_3PSe_4 are almost the same as the sum the patterns of the individual components, suggesting that no bulk reaction occurs in these paired materials after mixing at room temperature. In contrast, peak shifts and/or peak shape changes are observed after mixing $NaFeO_2$, $NaCoO_2$, or $NaNiO_2$ with Na_3PSe_4 (Figure 2.5 (e-j)), indicating a change in lattice dimension and/or symmetry. The majority of peaks that show noticeable differences are associated with Na_3PSe_4, which we believe is caused by either an anion exchange process creating intermediate $Na_3PO_xSe_{4-x}$ phases or topotactic Na extraction from Na_3PSe_4 accompanied by Se^{2-} oxidation. Through this simple test, our experiments already indicate that $NaFeO_2$, $NaCoO_2$, and

$NaNiO_2$ cathodes are likely incompatible with Na_3PSe_4. The compatibility between the selected cathode and electrolyte materials at elevated temperatures were tested by SDT, and the onset temperatures of the reactions of the cathode/electrolyte pairs are summarized in Table 2.3. It is noted that the SDT results show that $NaCoO_2$ and $NaNiO_2$ are not compatible with Na_3PS_4 at very low temperatures, close to RT (47°C and 30°C, respectively), even though no peak change in XRD can be observed after mixing them at RT (Figure 2.5 f and h). Unless other strategies such as protective barrier coatings are utilized to improve the compatibility of these electrodes (i.e. $NaFeO_2$, $NaCoO_2$, or $NaNiO_2$) with Na_3PX_4 electrolytes, alternative pairs should be sought.

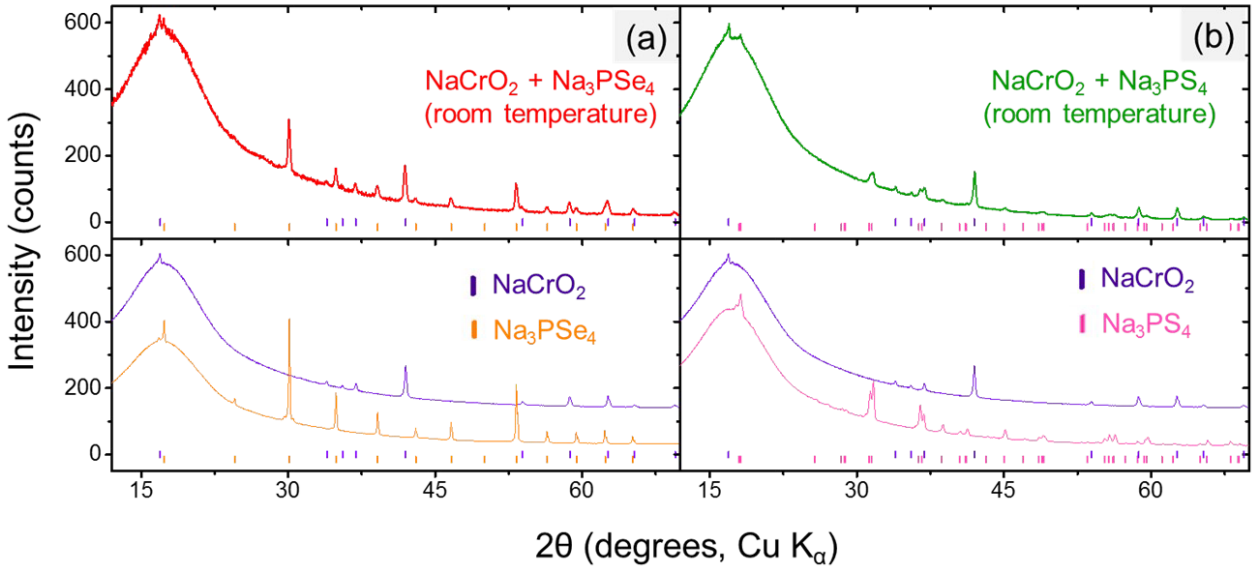

Figure 2.5: Reactivity between electrodes and solid electrolytes. (a–b) Diffraction patterns of $NaCrO_2$, Na_3PX_4, and mixture of the paired materials at RT (25°C); the tick marks indicate $NaCrO_2$ (purple, top) and Na_3PX_4 (orange for Na_3PSe_4, pink for Na_3PS_4, bottom) peaks. The diffraction pattern of the mixed materials is almost the same as the sum of those of each individual component, suggesting that no bulk reaction occurs between $NaCrO_2$ and Na_3PX_4 after mixing at RT.

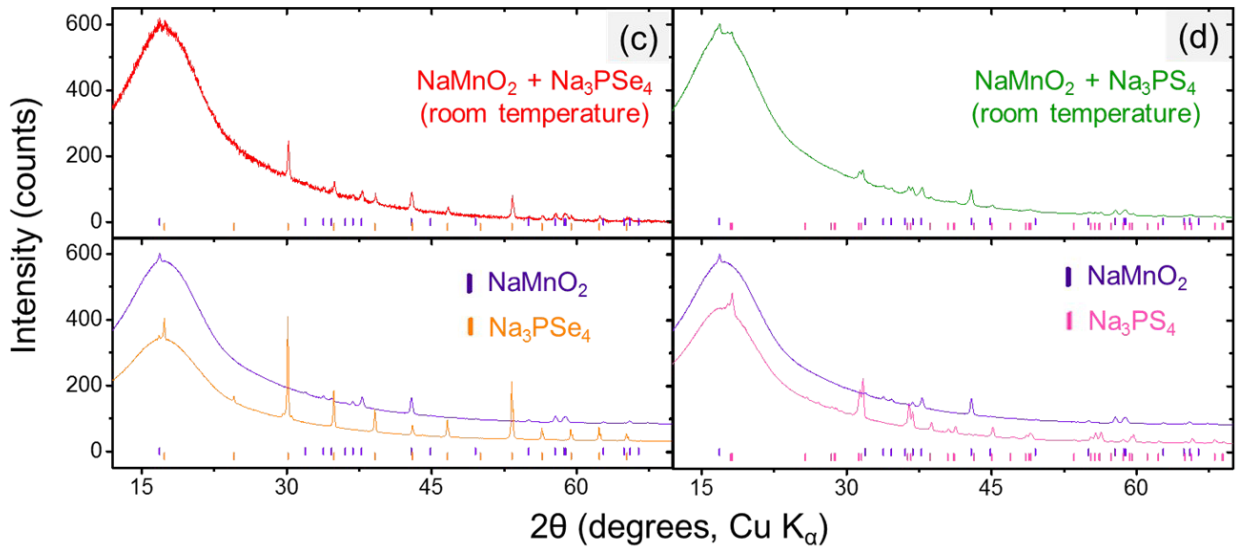

Figure 2.5: Reactivity between electrodes and solid electrolytes. (c–d) Diffraction patterns of $NaMnO_2$, Na_3PX_4, and a mixture of the paired materials at RT (25°C); the tick marks indicate $NaMnO_2$ (purple, top) and Na_3PX_4 (orange for Na_3PSe_4, pink for Na_3PS_4, bottom) peaks. No bulk reaction is observed between NaMnO2 and Na3PX4 after mixing at RT.

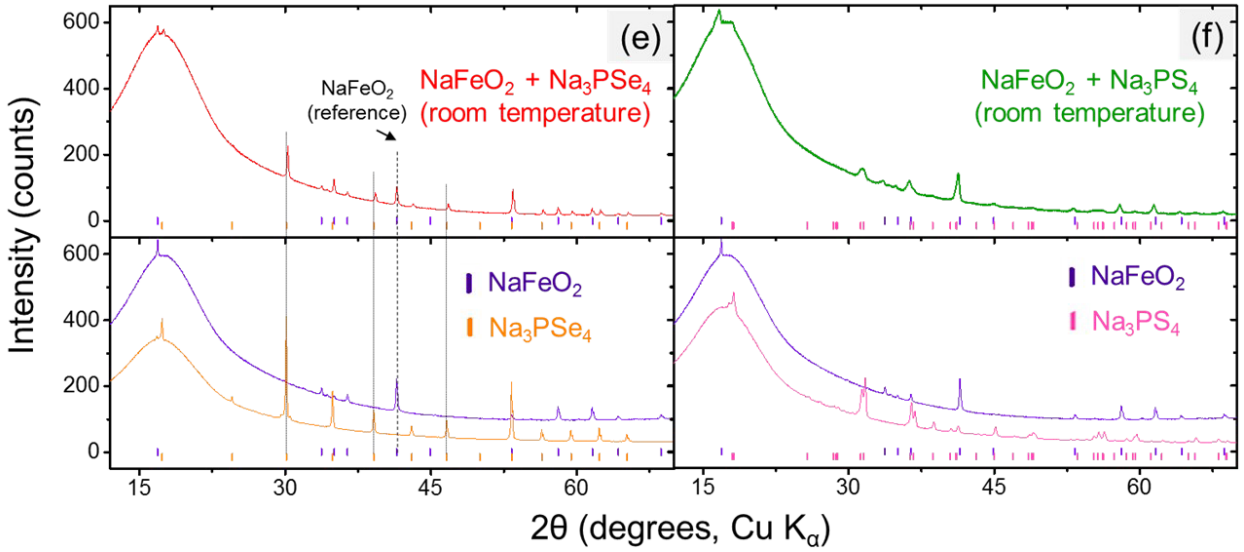

Figure 2.5: (e–f) Diffraction patterns of $NaFeO_2$, Na_3PX_4, and a mixture of the paired materials RT (25°C); the tick marks indicate $NaFeO_2$ (purple, top) and Na_3PX_4 (orange for Na_3PSe_4, pink for Na_3PS_4, bottom) peaks. Peak shifts are observed in (e) at 30°, 39°, and 46°, indicating that $NaFeO_2$ reacts with Na_3PSe_4 at RT. Note that only peak shifts of Na_3PSe_4 are observed (one peak of $NaFeO_2$ is marked as reference). No bulk reaction is observed between $NaCrO_2$ and Na_3PS_4 after mixing at RT in (f).

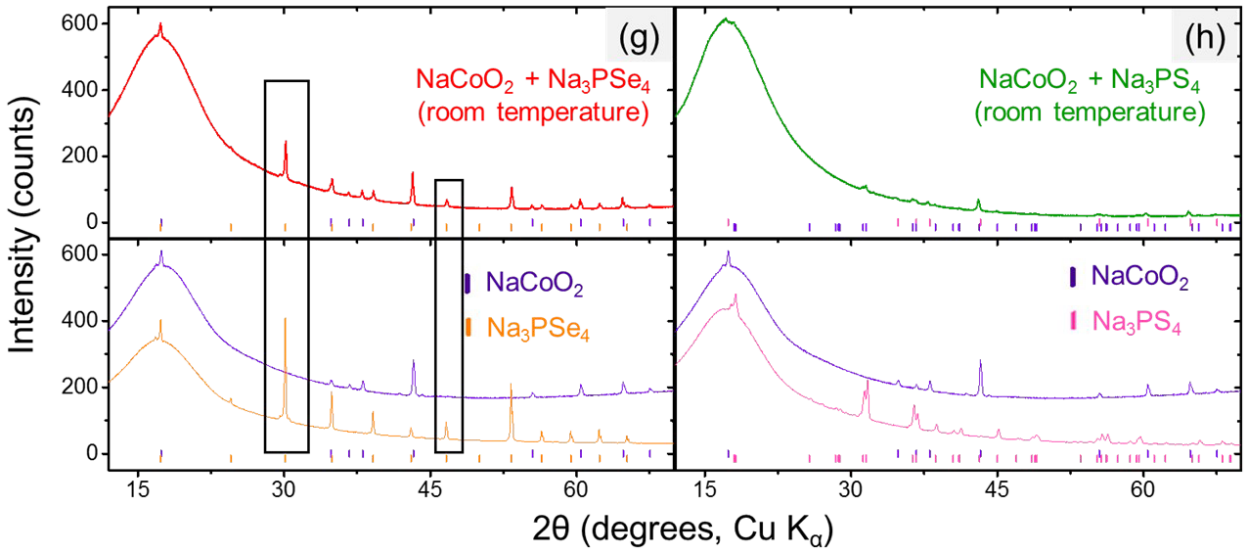

Figure 2.5: (g–h) Diffraction patterns of $NaCoO_2$, Na_3PX_4, and a mixture of the paired materials at RT (25°C); the tick marks indicate $NaCoO_2$ (purple, top) and Na_3PX_4 (orange for Na_3PSe_4, pink for Na_3PS_4, bottom) peaks. Peak shape changes are observed in (g) at 30° and 46°, indicating that $NaCoO_2$ reacts with Na_3PSe_4 at RT. No bulk reaction is observed between $NaCoO_2$ and Na_3PS_4 after mixing at RT in (h).

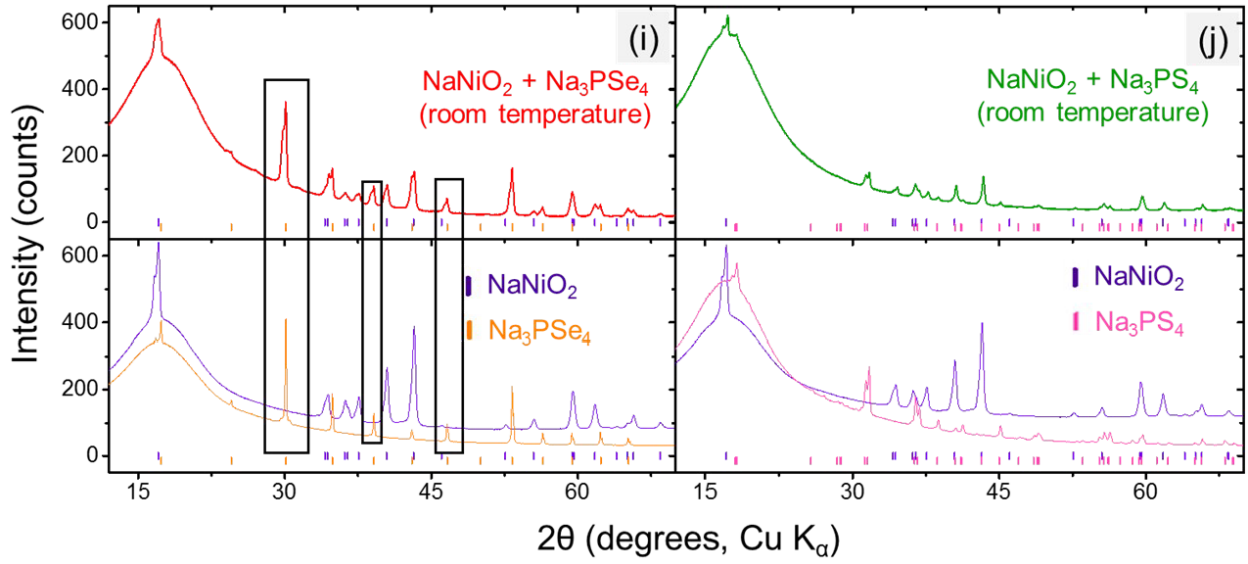

Figure 2.5: (i–j) Diffraction patterns of $NaNiO_2$, Na_3PX_4, and a mixture of the paired materials at RT (25°C); the tick marks indicate $NaNiO_2$ (purple, top) and Na_3PX_4 (orange for Na_3PSe_4, pink for Na_3PS_4, bottom) peaks. Peak shape changes are observed in (i) at 30°, 39°, and 46°, indicating that $NaNiO_2$ reacts with Na_3PSe_4 at RT. No bulk reaction is observed between $NaNiO_2$ and Na_3PS_4 after mixing at RT in (j).

Table 2.3: Onset temperatures of the reactions between NaMO$_2$ and Na$_3$PX_4

	$NaCrO_2$	$NaMnO_2$	$NaFeO_2$	$NaCoO_2$	$NaNiO_2$
Na_3PS_4	500°C	330°C	270°C	47°C	30°C
Na_3PSe_4	380°C	220°C	25°C*	25°C*	25°C*

* when a bulk change was observed after mixing paired materials at RT, we tentatively assigned 25°C as the onset temperature of the reaction

According to the onset temperature of each reaction between NaMO$_2$ and Na$_3$PX_4 listed in Table 2.3, two reaction trends are observed:

1) From $NaCrO_2$ to $NaNiO_2$, the onset temperature decreases, indicating a reduction of the kinetic barrier, which may be related to an increase of the driving force of each reaction (Table 2.1).
2) From Na_3PS_4 to Na_3PSe_4, the onset temperature also decreases.

The cathode–electrolyte pairs for which no bulk reactions were observed close to RT (i.e., $NaCrO_2$ and $NaMnO_2$ with Na$_3$PX_4) were subjected to combined SDT and XRD characterization. These simple tests were quite informative, as they provided insight into the intriguing interplay between thermodynamics and kinetics in the decomposition reactions. Taking $NaCrO_2$ and Na$_3$PX_4 as an example, when these mixtures were heated to below approximately 300°C, no bulk reaction was observed in the XRD results (Figure 2.6(a, b)). This finding suggests that $NaCrO_2$ and Na$_3$PX_4 should be a relatively stable pair that could be used in solid-state batteries at RT. When the reaction temperature was raised to 500°C, $NaCrSe_2$ (along with excess $NaCrO_2$) was observed in the final products of the reaction between $NaCrO_2$ and Na_3PSe_4 (green line in Figure 2.6(b)), which partially agrees with the DFT calculation result in Table 2.1. No other P-containing phases were observed in the XRD result. Because no substantial mass loss (<0.6%) was observed upon heating to 500°C (Figure 2.6(d)), P-containing phases should still be present in the mixture but in amorphous form. Taken together with the DFT prediction (Table 2.1), we suspect that amorphous Na_3PO_4 is present in the heated mixture. However, when the conductor was changed to Na_3PS_4, the calculated reaction products between $NaCrO_2$ and Na_3PS_4 with the highest driving force (i.e. $NaCrS_2$ and Na_3PO_4) were not observed after heating to 500°C. Instead, Na_3PS_3O (together with both precursors $NaCrO_2$ and Na_3PS_4) was observed (green line in Figure 2.6(a)). It is not until 700°C that the predicted product $NaCrS_2$ (together with excess $NaCrO_2$) starts to appear with the disappearance of Na_3PS_3O (orange line in Figure 2.6(a)). Although the predicted $NaCrS_2$ might be present in the heated mixture in amorphous form, the presence of Na_3PS_3O in lieu of the predicted product Na_3PO_4 may indicate a preference for intermediate reaction products over the stable thermodynamic states unless the temperature is very high. We also note from Table 2.1 that the reaction energy between $NaCrO_2$ and the selenide conductor is substantially higher than with the sulfide conductor.

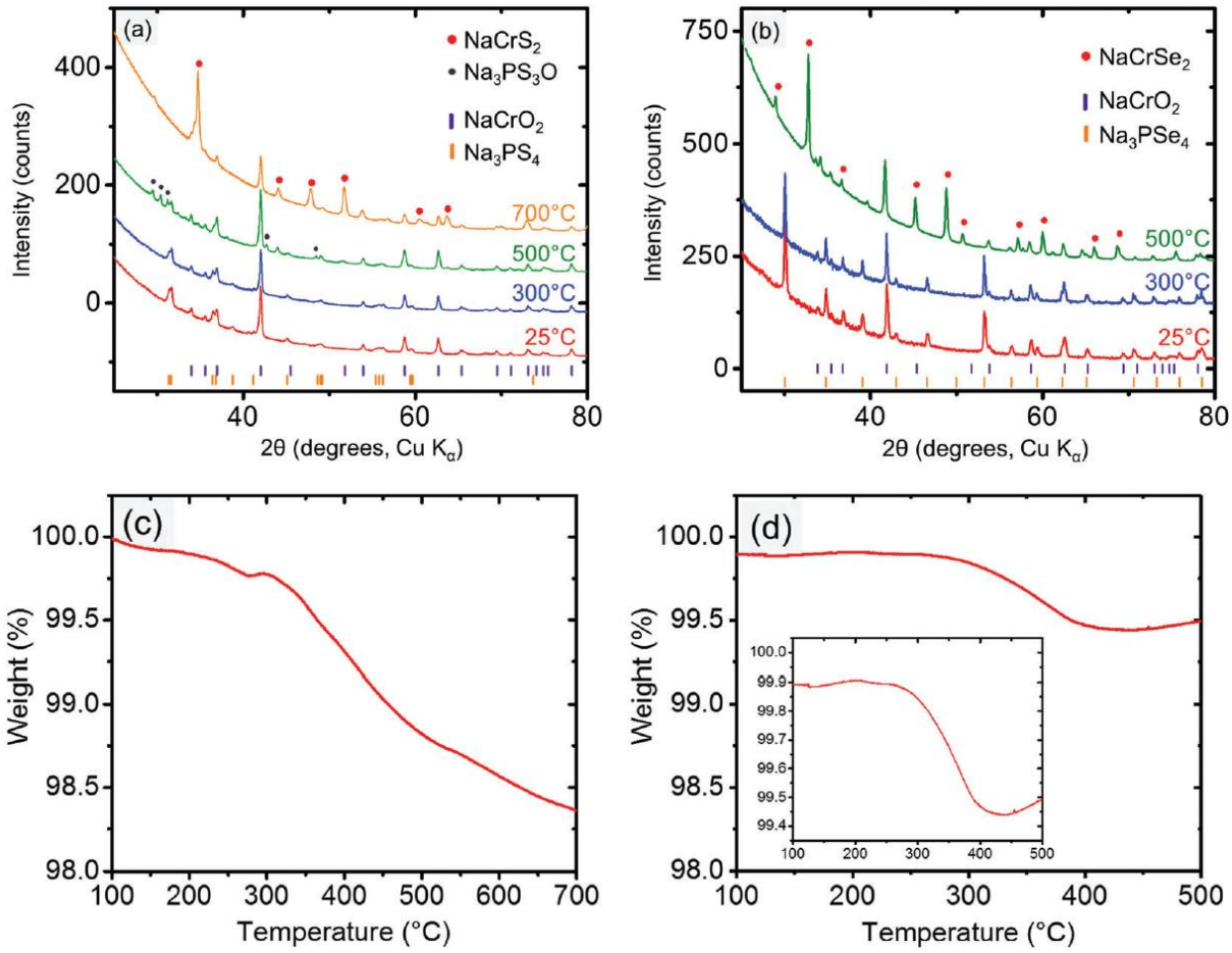

Figure 2.6: Characterization of the reaction products. XRD patterns of the reaction products of (a) $NaCrO_2$ and Na_3PS_4 at RT, 300°C, 500°C, and 700°C, and (b) $NaCrO_2$ and Na_3PSe_4 at RT (25°C), 300°C, and 500°C. The tick marks indicate the peaks for the reactants $NaCrO_2$ (purple, top) and Na_3PX_4 (orange, bottom). TGA measurements (total weight) of the reactions between (c) $NaCrO_2$ and Na_3PS_4 and (d) $NaCrO_2$ and Na_3PSe_4. The weight axis is shown in the same scale to emphasize the higher reactivity of S-based compound.

3) Chemical reactions between desodiated cathode and electrolyte

The compatibility between the partially desodiated cathode Na_xMO_2 ($x < 1.0$) and electrolyte Na_3PX_4 is equally important for the stable cycling of all-solid-state batteries and was also investigated. We first prepared the chemically desodiated $NaCrO_2$, $NaCoO_2$, $NaFeO_2$, and $NaNiO_2$ samples using a highly-concentrated iodine solution in acetonitrile, which is equivalent to oxidation at ~3.7 V[142]. The same process always yields amorphous desodiated $NaMnO_2$, likely due to Mn dissolution into the acetonitrile solvent[143]. Desodiated $NaMnO_2$ was therefore excluded in our study. The diffraction patterns for desodiated $NaCrO_2$, $NaCoO_2$, $NaFeO_2$, and $NaNiO_2$ are presented in Figure 2.7. The products after chemical desodiation were $Na_{0.5}CrO_2$, $Na_{0.5}FeO_2$ + β-$NaFeO_2$, $Na_{0.5}CoO_2$, and $Na_{0.5}NiO_2$ + $Na_{0.4}NiO_2$, respectively. The Na compositions

of Na_xMO_2 compounds were estimated based on comparisons of the refined lattice parameters and electrochemical capacity with previous literature. Interestingly, β-$NaFeO_2$ was generated after chemical desodiation of $NaFeO_2$, which may be one of the causes of the observed irreversibility in $NaFeO_2$, as β-$NaFeO_2$ is not electrochemically active according to our electrochemical measurements (Figure 2.9).

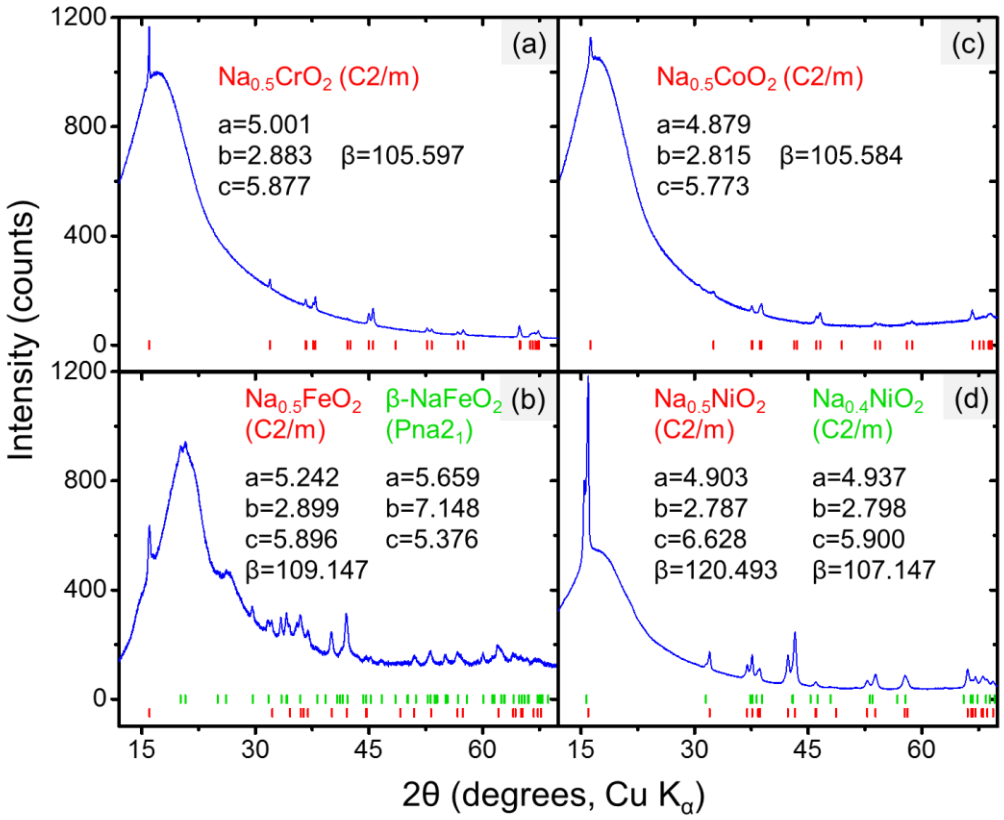

Figure 2.7: Characterization of desodiated compounds. Diffraction patterns of desodiated compound(s) of (a) $NaCrO_2$, (b) $NaFeO_2$, (c) $NaCoO_2$, and (d) $NaNiO_2$. The peak positions and refined structure data are also displayed; the hump at ~15° in all four figures originates from the Kapton sample holder (the diffraction pattern of the empty sample holder is presented in Figure 2.8).

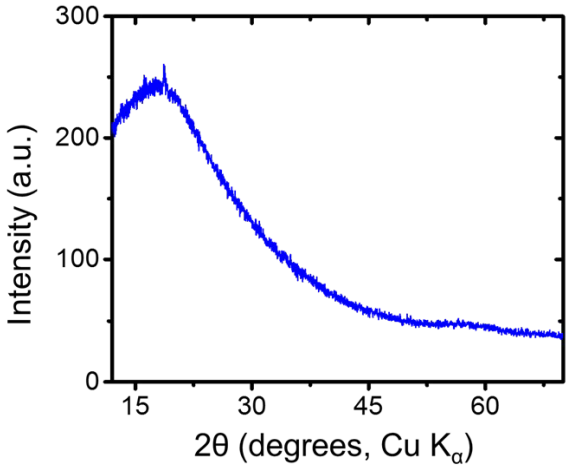

Figure 2.8: Diffraction pattern of Kapton sample holder.

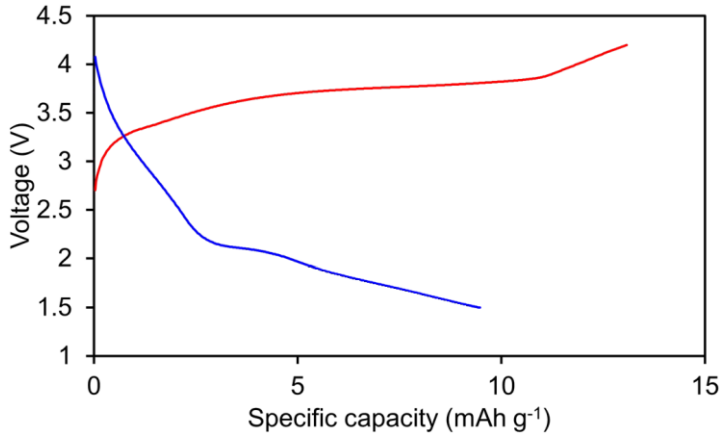

Figure 2.9: Electrochemical measurement of β-$NaFeO_2$. Cut-off voltage: 4.0 V for charging, 1.5 V for discharging. The low capacity demonstrates the electrochemical inactivity of β-$NaFeO_2$.

When the partially desodiated samples were mixed with Na_3PX_4, only $Na_{0.5}CrO_2$ was observed to be compatible with Na_3PX_4 at RT (i.e., no bulk reaction was observed in the XRD results, see Figure 2.10(a, b)). All of the other partially desodiated samples reacted with the electrolyte, and some of the reactions were rather violent. For example, when partially desodiated $NaNiO_2$ was mixed with Na_3PX_4 in an Ar glove box, sparks were immediately generated and the powder color changed to dark red.

Because $Na_{0.5}CrO_2$ is the only compound compatible with Na_3PX_4 at RT among our observations, further studies with XRD and SDT at elevated temperatures were performed. In the XRD of mixed $Na_{0.5}CrO_2$ and Na_3PX_4, we observed that fully sodiated $NaCrO_2$ was regenerated after heating the mixture to 300°C in reactions with both Na_3PSe_4 (Figure 2.10(a)) and Na_3PS_4 (Figure 2.10(b)), suggesting that Na is extracted from the Na_3PX_4 electrolyte and inserted into $Na_{0.5}CrO_2$, consistent with the thermodynamic anodic potentials predicted for the Na_3PX_4 electrolytes (2.25 V for Na_3PS_4 and 2.15 V for Na_3PSe_4), which are well below the $Na_{0.5}CrO_2$ voltage (~3.7 V vs. Na/Na^+).

This Na insertion to $Na_{0.5}CrO_2$ is similar to a self-discharge reaction, as often observed in rechargeable batteries, leading to decomposition of the electrolyte (i.e. Na_3PX_4). As shown in Figure 2.2, S or Se is likely generated in the decomposition products by oxidizing Na_3PX_4. In the

reaction between $Na_{0.5}CrO_2$ and Na_3PSe_4, the generation of Se can indeed be observed in our differential scanning calorimetry (DSC) measurements (Figure 2.10(c)), where an endothermal peak is observed at approximately 220°C, corresponding to the melting point of Se (220.8°C). The following exothermal peak is attributed to the heat generation of the bulk reaction. In contrast, the generation of S cannot be observed in the reaction between $Na_{0.5}CrO_2$ and Na_3PS_4. In the DSC result for the reaction between $Na_{0.5}CrO_2$ and Na_3PS_4 in Figure 2.10(d), only one exothermal peak is observed at approximately 260°C reflecting the heat generation of the reaction.

The surface reaction at RT between $Na_{0.5}CrO_2$ and Na_3PX_4 was investigated by X-ray photoelectron spectroscopy (XPS). After mixing $Na_{0.5}CrO_2$ and Na_3PX_4 at RT, XPS measurements were performed on the Cr 2p peaks of the mixture. The Cr 2p reference peak positions in Cr^{3+} and Cr^{4+} were obtained by fitting the Cr $2p_{1/2}$ and $2p_{3/2}$ peaks in $NaCrO_2$ (Cr^{3+} only) and $Na_{0.5}CrO_2$ (Cr^{3+}: Cr^{4+} = 1:1), respectively (Figure 2.11(c, d)). The XPS spectrum of the Cr 2p peaks in the mixture of $Na_{0.5}CrO_2$ and Na_3PSe_4 is presented in Figure 2.11(b), and the fitting result indicates that the Cr^{3+}/Cr^{4+} ratio changed from approximately 1.0 in $Na_{0.5}CrO_2$ to 2.423 in the mixed material (Table 2.4). The reduction of Cr^{4+} indicates an insertion of Na to $Na_{0.5}CrO_2$. This surface reaction between $Na_{0.5}CrO_2$ and Na_3PSe_4 at RT cannot be detected in XRD (Figure 2.10(a)), reflecting a slow kinetics and/or a self-passivation reaction mechanism. It is likely that the reaction products form a passivation layer and prevent further reaction, which explains why no bulk reaction is observed at RT in XRD. Based on the above discussion, the surface reaction is likely associated with the production of Se. As the temperature increases to the melting point of Se, the passivation layer becomes unstable and further reaction is activated, which is in good agreement with our observation in DSC (Figure 2.10(c)). When $Na_{0.5}CrO_2$ was mixed with Na_3PS_4, a lower Cr^{3+}/Cr^{4+} ratio increase (i.e. less Cr^{4+} reduction) was observed (Table 2.4), indicating that less Na was extracted from Na_3PS_4 in the reaction between $Na_{0.5}CrO_2$ and Na_3PS_4. This observation is likely due to the slightly lower reactivity of Na_3PS_4, which is in line with the onset temperatures of the reaction between $NaMO_2$ and Na_3PX_4 (Table 2.3).

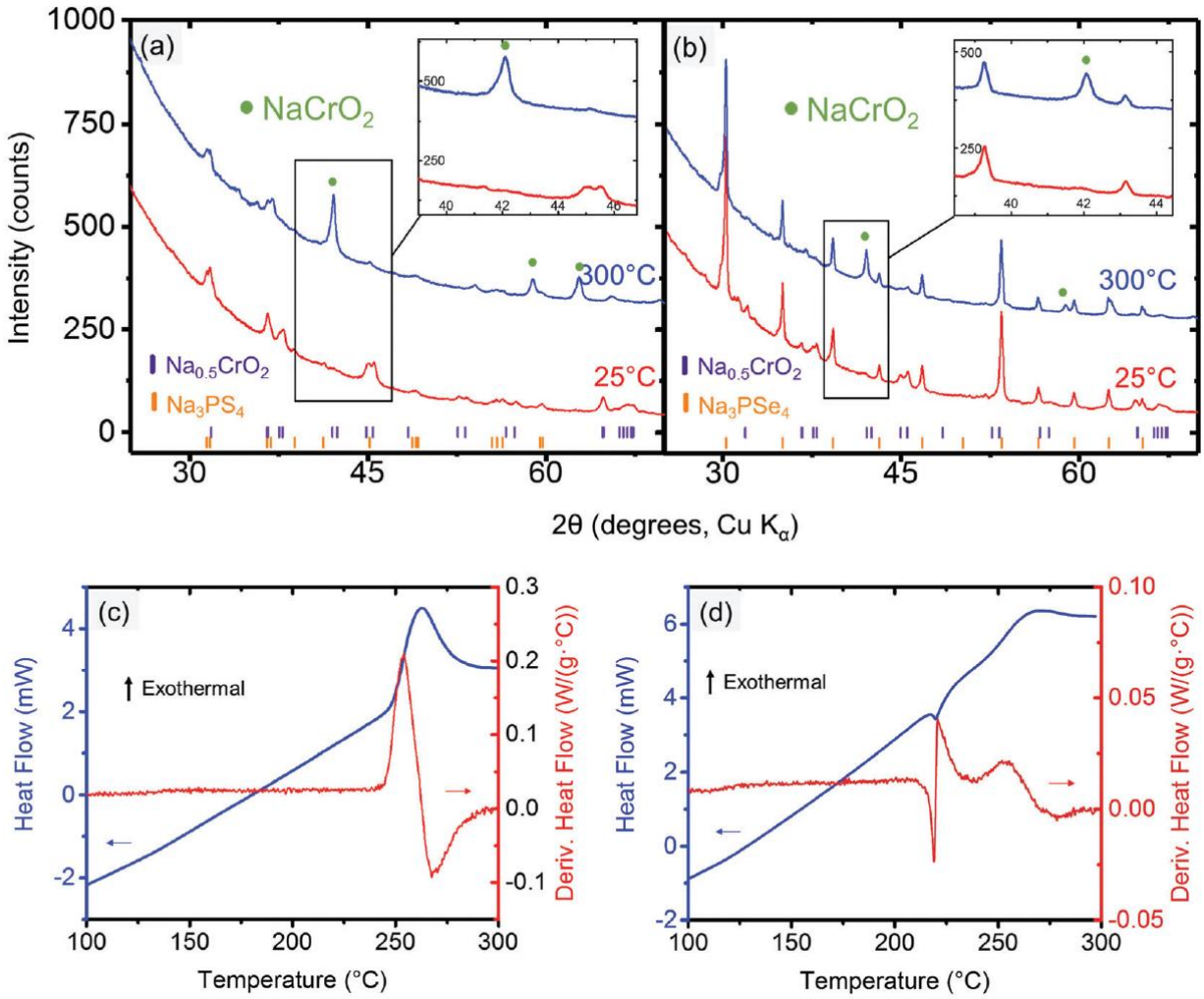

Figure 2.10: Reaction products of desodiated cathodes and solid electrolytes. XRD results for reaction between (a) $Na_{0.5}CrO_2$ and Na_3PS_4 and (b) $Na_{0.5}CrO_2$ and Na_3PSe_4 at RT (25°C) and 300°C. DSC results for reaction between (c) $Na_{0.5}CrO_2$ and Na_3PS_4 and (d) $Na_{0.5}CrO_2$ and Na_3PSe_4.

Table 2.4: XPS data fitting results for Cr 2p peaks

Sample	Component	Peak Position (eV)		Area (a.u.)		Cr^{3+}/Cr^{4+} Ratio
		$2p_{3/2}$	$2p_{1/2}$	$2p_{3/2}$	$2p_{1/2}$	
$Na_{0.5}CrO_2/Na_3PS_4$ RT Mixture	Cr^{3+}	577.03	586.52	299	149	1.869
	Cr^{4+}	579.09	588.52	160	80	
$Na_{0.5}CrO_2/Na_3PSe_4$ RT Mixture	Cr^{3+}	577.03	586.52	344	172	2.423
	Cr^{4+}	579.09	588.52	142	71	
$Na_{0.5}CrO_2$	Cr^{3+}	577.03	586.52	470	234	0.997
	Cr^{4+}	579.09	588.52	484	242	
$NaCrO_2$	Cr^{3+}	577.03	586.52	661	331	/

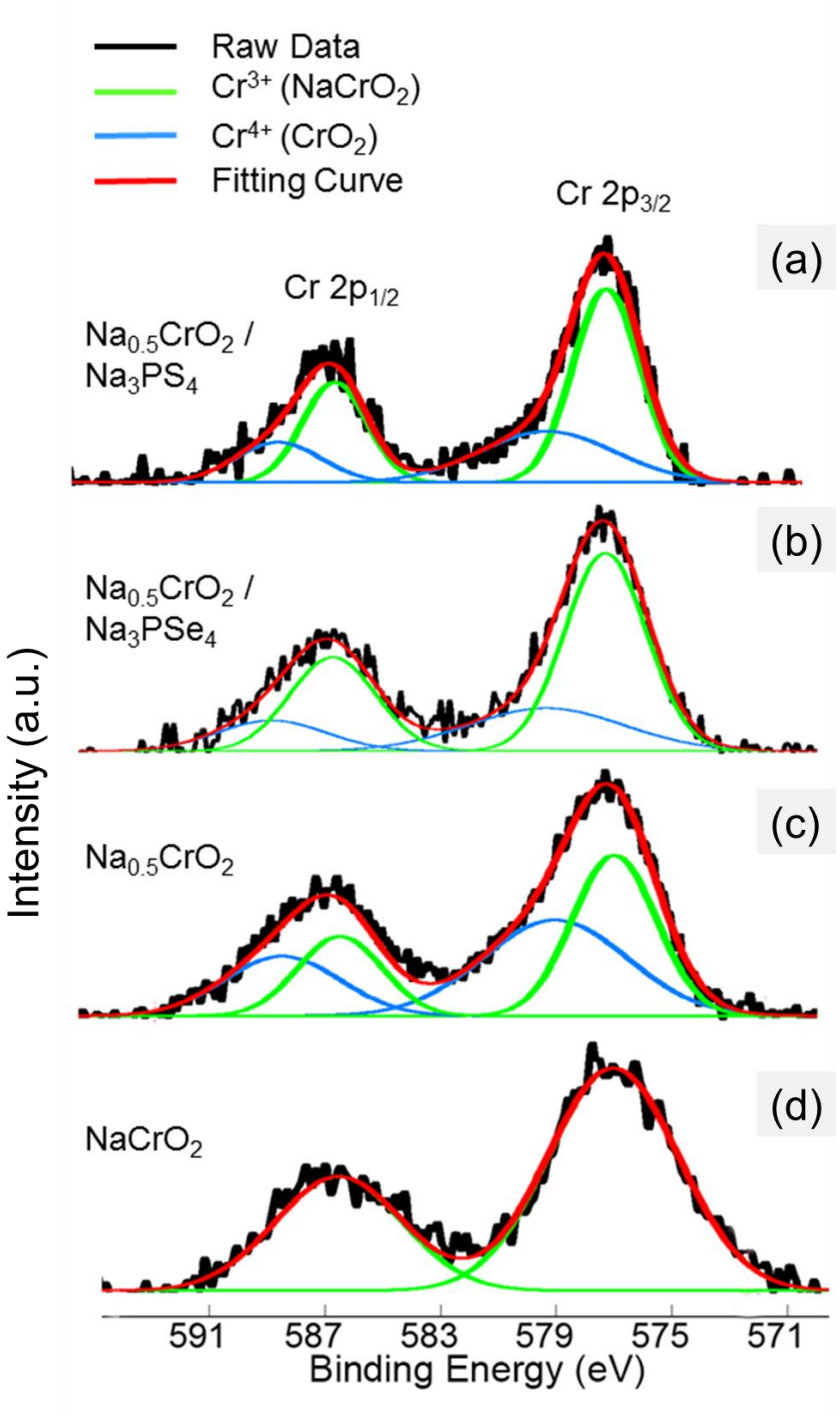

Figure 2.11: XPS characterization of the reaction product. XPS spectra of Cr 2p from the surfaces of (a) mixture of $Na_{0.5}CrO_2$ and Na_3PS_4 at RT (25°C), (b) mixture of $Na_{0.5}CrO_2$ and Na_3PSe_4 at RT (25°C), (c) $Na_{0.5}CrO_2$, and (d) $NaCrO_2$.

III. Compatibility between anode and electrolyte

The compatibility between the electrolyte and anode was investigated by cycling the Na/electrolyte/Na symmetric cells under a constant current density (typically 0.1 or 0.2 mA/cm^2).

The symmetric cell was first galvanostatically cycled at 1 min per cycle. An increasing voltage during cycling is observed in Figure 2.12(a) even at very low current density (0.1 mA/cm^2), suggesting an unstable metal/electrolyte interface. The cell failed after approximately 11.4 h of cycling, when Na_3PSe_4 was fully decomposed into amorphous phases (Figure 2.12(b)), likely Na_3P and Na_2Se based on our DFT calculations (Figure 2.2(b)). Thus, we conclude that Na_3PSe_4 is not compatible with a Na metal anode.

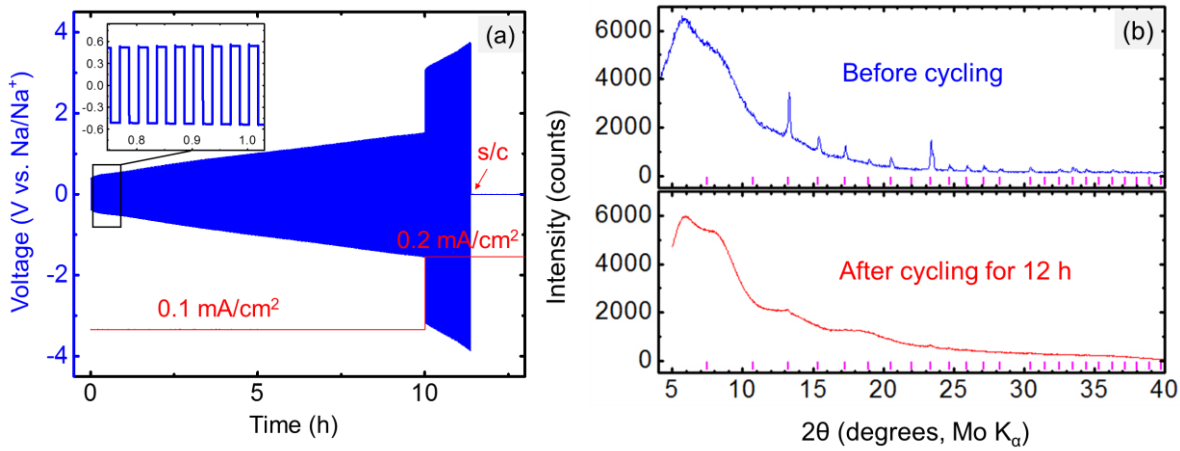

Figure 2.12: Characterization of the Na anode instability. (a) Electrochemical cycle for Na|Na_3PSe_4|Na symmetric cell; a short circuit (s/c) occurred after cycling for 11.4 h. (b) XRD results for Na_3PSe_4 (mixed with carbon) before and after cycling for 12 h (1 min per cycle); the tick marks indicate Na_3PSe_4 peaks.

To improve the compatibility between the anode and electrolyte, a "Na_2Sn" alloy with higher potential (~0.3 V vs. Na/Na$^+$) was synthesized. According to the Na–Sn binary phase diagram[128,144], the two stable phases near this composition are NaSn and Na_9Sn_4, with the latter being the majority phase. The Na_2Sn|Na_3PSe_4|Na_2Sn symmetric cell was galvanostatically cycled at 60 min per cycle. A relatively stable voltage during cycling at low current density (0.1 mA/cm^2) is observed in Figure 2.13(a), indicating enhanced interface stability. However, at a higher current density (0.2 mA/cm^2), the interface becomes unstable, and Na_2Se was observed after cycling for 40 h (Figure 2.13(b)).

Because Na metal is reported to be incompatible with Na_3PS_4 forming Na_2S and Na_3P decomposition products[145], consistent with our DFT calculation results shown in Figure 2a, only the compatibility between the Na_2Sn anode and Na_3PS_4 was then investigated by cycling a Na_2Sn|Na_3PS_4|Na_2Sn symmetric cell. A stable anode–electrolyte interface was obtained, signified by the approximately constant voltage during cycling at both low and high current densities (Figure 2.14). We thus concluded that the "Na_2Sn" alloy is a promising anode candidate for use in solid-state batteries employing Na_3PS_4 solid electrolytes.

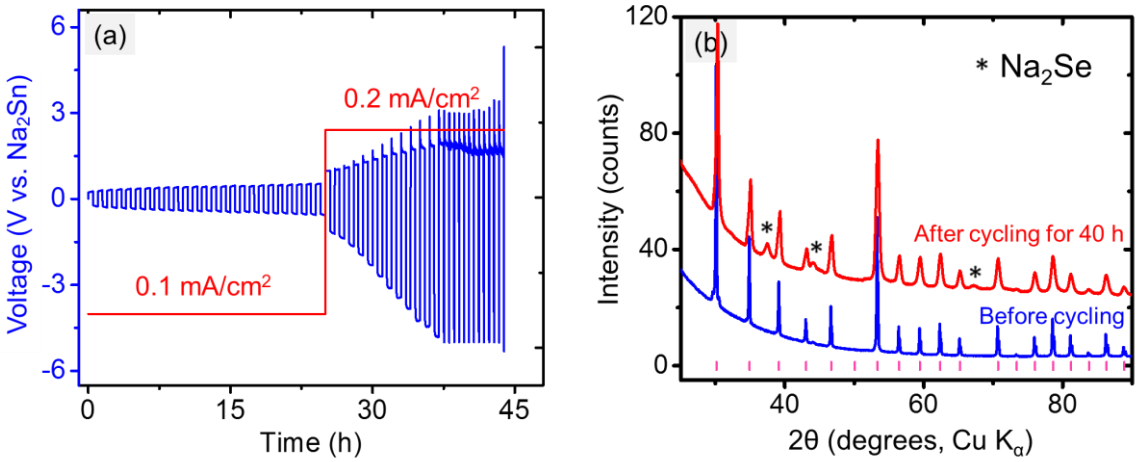

Figure 2.13: Characterization of the improved anode instability for NaSn alloy. (a) Electrochemical cycling of $Na_2Sn|Na_3PSe_4|Na_2Sn$ symmetric cell. (b) XRD patterns of Na_3PSe_4 before and after cycling for 40 h (60 min per cycle); the tick marks indicate Na_3PSe_4 peaks.

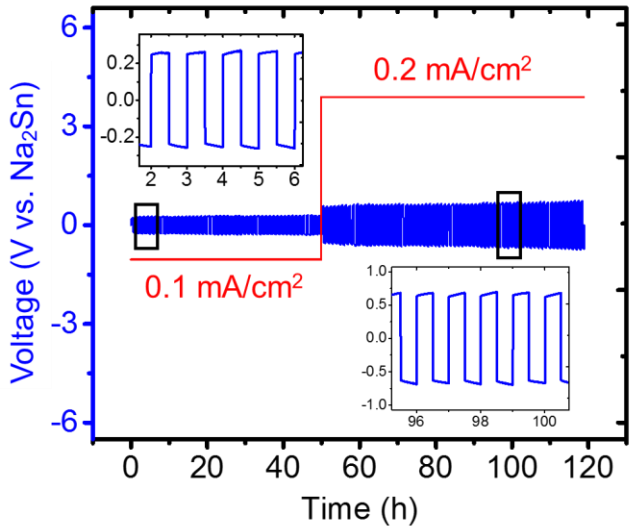

Figure 2.14: Electrochemical cycling of $Na_2Sn|Na_3PS_4|Na_2Sn$ symmetric cell (60 min per charge and discharge). The insets present zoomed-in voltage profiles during cycling from 2–6 h and 96–100 h.

2.6 Discussion

Interface stability has become a critical yet difficult problem for all-solid-state battery development. The methodology presented here provides a roadmap for studying the compatibility between solid electrolytes and electrodes, based on fairly straightforward computational analysis, symmetric cell testing, and the use of fast and simple techniques such as XRD and SDT, which are widely accessible to the research community.

We distinguish the pure electrochemical stability of the solid-state electrolyte at various Na chemical potentials (and in contact with Na reservoir) from the chemically-enhanced instability when solid-state electrolyte and cathode chemically interact. The pure electrochemical stability is relevant wherever the solid electrolyte is in contact with the electron reservoir. Hence this occurs at the cathode/electrolyte interface, at a direct contact with the current collector, or through the carbon network present in the electrode. Since Na^+ is highly mobile in the solid-state electrolyte, the conductor experiences the full chemical potential of Na applied at these electron contact interfaces. Computationally, we calculate the stability of the conductor in this condition by evaluating the thermodynamic grand potential of the compound under various applied Na chemical potentials, as described in prior work[114]. This analysis requires the availability of thermochemical information on a number of competing phases in the phase diagram of the conductor. Such information can for example be found in online resources such as the Materials Project[146]. This thermodynamic analysis for the electrochemical stability of the conductor provides a "safe" voltage window, in which there is no driving force at all for decomposition of the conductor. Because the thermodynamic decomposition of the conductor may sometimes require complete bond breaking in the material to form multiple other phases, it may be kinetically inhibited at the operating temperature of the battery. Hence, we also provide a kinetic anodic stability limit by evaluating at which potential, Na^+ can simply be extracted topotactically from the conductor together with the oxidation of the anion (S^{2-} or Se^{2-} in our case). Because the material is by definition a fast Na-ion conductor, and anion oxidation is easy, one expects there to be no kinetic barrier for this process. Hence, this topotactic Na extraction voltage can be considered an absolute upper bound for the voltage at which the conductor can operate. To test these computed stability limits we evaluated the conductor as an electrode in an electrochemical cell using liquid electrolyte so that contact problems, often present in full solid-state devices, will not mask instabilities. The computational and experimental results summarized in Table 2.5 clearly indicate that the measured upper voltage limit lies between the thermodynamic upper voltage and the topotactic Na extraction limit, in agreement with our understanding. Table 2.5 also clearly shows that CV is a poor tool to measure electrochemical stability of solid-state conductors. The poor reliability of CV measurements has led for example to claims that some sulfide conductors have 5V or even 10V stability[58,133,147,148], which is counterintuitive, given that a sulfide ion can general be oxidized between 2-3V.

Table 2.5: Comparisons of the various stability windows obtained theoretically and experimentally for Na_3PX_4

	Thermodynamic window (V)	Kinetic upper limit (V)	Experimental (liquid cell charging) upper limit (V)	Experimental (CV measurement) upper limit (V)
Na_3PS_4	1.55 - 2.25	3.05	2.50	> 5 V[58]
Na_3PSe_4	1.80 - 2.15	2.75	2.33	2.6 V *

*Data shown in Figure 2.15

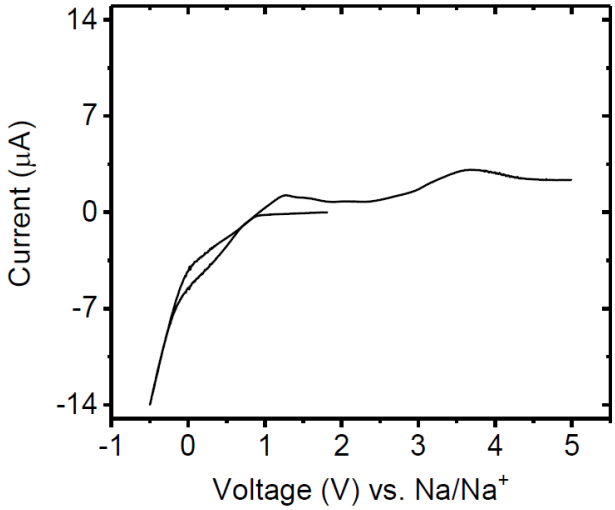

Figure 2.15: Cyclic voltammogram of the Na_3PSe_4 solid-state electrolyte. A platinum foil, as the working electrode, and a sodium foil, as the counter/reference electrode, were used. The potential sweep was performed with a scanning rate of 5 mV s−1 at 25 °C.

In contact with the cathode, the conductor (i.e., solid-state electrolyte) can also undergo chemical reactivity. To determine this reactivity, we used a combination of XRD, SDT and XPS to evaluate the reaction products in mixed cathode/electrolyte powders. Through the study of more than 20 cathode/electrolyte reactions between layered Na transition metal oxides ($NaMO_2$, *M*=Cr, Mn, Fe, Co, Ni) and two solid electrolytes (Na_3PX_4, *X*=S, Se), we were able to determine trends and understand the mechanisms behind these reactions. We first determine the thermodynamic driving forces and end-products of the cathode/electrolyte reaction, and then discuss what may happen under more kinetically constrained conditions. There are some common trends that can be understood from Table 2.1:

(1) On the cathode/conductor interface P strongly prefers bonding to O, resulting in the exchange of O and S/Se between the cathode and conductor, and the formation of PO_4 groups. As a result, Na_3PO_4 is produced for all reactions listed in Table 2.1.

(2) Some transition metals, even in the discharged redox state can oxidize the chalcogenide anion leading to reaction products that are metallic, have per-sulfide or per-selenide ions, or even sulfate ions. This is the case for the $NaFeO_2$ and $NaNiO_2$ cathodes against both conductors and

for the $NaCoO_2$ cathode against the selenide conductor. The fact that the $NaCoO_2$ seems redox stable with the sulfide but not with the selenide is likely due to the fact that the Se^{2-} ion is easier to oxidize than S^{2-}.

Once the cathodes are charged (bottom part of Table 2.1) oxidation of the anion by reduction of the transition metal is favorable for all cathode/conductor couples, and only local passivation with an electron-insulating layer will protect the conductor. The reaction products that form at the interface are however dependent chemistry of each cathode. In some cases, elemental S is predicted to occur (e.g. $Na_{0.5}CrO_2$ with Na_3PS_4) while for other cathode/conductor couples reduced metal sulfides are usually predicted (MnS, FeS_2, etc.). The reaction products for the Co and Ni cathode deserve particular attention. Compounds such as Ni_9S_8 and Co_9Se_8 are in the pentlandite family and have a structure containing an excess of metal atoms and short metal-metal distance[149,150]. Similar metal-metal bonding also exists in other metal-rich chalcogenides such as Ni_3S_2[151,152]. These compounds are metallic and hence will not provide any passivation protection.

Though it is useful to understand the thermodynamic endpoints of the cathode/conductor reaction as shown in Table 2.1, comparison with the experimentally observed products clearly indicates that these phases do not always form, as would be expected under conditions where kinetics may be limited.

First, when the electrode and electrolyte are in contact, arbitrary amounts of these phases can react, forming an interface layer of decomposition products that can take on, in principle any average composition between the cathode and electrolyte composition depending on the ratio in which they react. This renders many possible reaction pathways plausible. In our previous modeling approach, a mixing parameter x ($0 < x < 1$) between the electrode and electrolyte was introduced in our calculations[114]. By scanning a range of x from 0 to 1, we calculated the reaction enthalpies for all possible reactions and determined the mostly likely reaction as the one with the largest thermodynamic driving force. This approach was largely successful in predicting the decomposition products between electrodes and electrolytes, and indeed, many of the predictions have recently been verified by experiments[66,121,153,154]. However, it is important to keep in mind that in principle <u>all</u> reactions with positive driving force can take place spontaneously, and which ones occur first depends on their kinetics. To make a broader comparison with future experiments possible we have listed in Tables S1 possible reaction products that can be formed for each cathode/electrolyte couple. Given these constraints, it is remarkable that many of the experimentally observed products are the ones predicted in the thermodynamic calculations[153,155] This finding may result from the very thin interface layer (nanometer scale) formed, requiring only very short diffusion lengths.

Several of the experimental products we observed can be explained by adding at least a qualitative layer of kinetic constraints on top of the predictions. For example, in the reaction between $NaCrO_2$ and Na_3PS_4, the theoretically predicted product (Na_3PO_4) was not observed at temperatures below 700°C. Instead, the intermediate Na_3PS_3O was formed at lower temperatures, which may be thought of as an intermediate towards the exchange of S and O in the conductor.

One reaction that however cannot be kinetically limited is the exchange of Na ions between the electrolyte and cathode. As a result, cathodes that are charged above the anodic voltage limit of the conductor will always extract Na from the solid-state electrolyte, at which point the electrolyte will degrade and decompose. This concept rationalizes our experimental observation when $Na_{0.5}CrO_2$ and Na_3PSe_4 come in contact. The results in Table 2.1, assuming diffusion is not limited,

predicted the formation of $Na_{1/3}(CrSe_2)$, $Na_{2/3}(CrSe_2)$, and Na_3PO_4 decomposition products. However, experimentally a more limited reaction is observed whereby Na is extracted from the electrolyte, causing electrolyte decomposition, and producing fully sodiated $NaCrO_2$.

In the two cases discussed above, instead of taking the reaction pathway with the largest thermodynamic driving force, which involves diffusion and rearrangement of elements, a reaction via anion and Na exchange processes is observed. This finding is not surprising as reactions involving well-known mobile species (e.g., Na^+) are fast and kinetically favored. Overall, in the analysis of electrode/electrolyte reactions, our results suggest that in addition to the ones with the largest driving forces, other reactions with similar thermodynamic driving forces but faster kinetics (e.g., topotactic Na extraction/insertion) should also be considered in electrode/electrolyte reactions.

With the driving forces that may degrade the cathode/electrolyte interface better understood, one can develop strategies to alleviate these. The anion-exchange reaction is mainly driven by the tendency to form the stable phosphate group. Therefore, this type of reaction may be prevented by fully or partially replacing P in the solid electrolytes with other suitable elements that do not exhibit strong bonding preference with O, such as Sb, Ge, Sn, or As. Interestingly, recent studies suggest that a $NaCrO_2$ cathode can be cycled reversibly using a Na_3SbS_4 solid-state electrolyte, indicating that replacing P with Sb in the sulfide electrolyte resulted in improved compatibility with the oxide cathode[103,119]. We expect that a similar effect will be observed for Na_4SnS_4[156], Li_4SnS_4[157], Li_4GeS_4[158], Li_3AsS_4[159], and similar materials. Another possible strategy to prevent the anion exchange is to use polyanion cathodes with stable anion groups such as PO_4. Since the O is already in a stable configuration, it is unlikely to participate in the anion exchange reaction. Changing from an oxide-based cathode to a sulfide-based cathode will also mitigate the interface issue, although sulfide-based cathodes will operate at a lower voltage than their oxide counterparts, thus reducing the overall energy density of the batteries. The redox degradation pathway requires transition metal reduction in the cathode. While this seems inevitable in a charged cathode, it may be preventable in the discharged cathode by selecting transition metals that are difficult to reduce (e.g., Cr^{3+} Mo^{3+}, V^{3+}, Nb^{3+} and Ti^{3+}). The thermodynamic stability requirement between the conductor and discharged cathode is often more stringent as processing of a solid-state battery may bring this system to elevated temperature. This is not the case for the charged cathode which is usually only exposed to the conductor during room temperature operation.

Finally, one always has the option to coat the electrode to protect it chemically from the electrolyte[115,116,160]. Because the coating is often a thin layer which has less stringent requirement for ionic conductivity than that of the bulk electrolyte, this brings many more materials choices than those of bulk electrolytes, making the selection of a chemically and electrochemically stable coating material possible[68]. However, we believe that passivating solid-state electrolytes is equally important and should be explored in future studies. Coating only the cathode still exposes the electrolyte to electronic pathways created by carbon in the cathode. According to our electrolyte stability testing results, it is clear that electronic pathways promote the decomposition of the electrolyte via the extraction of Na^+ and oxidation of the anion in the conductor. Therefore, the electrode coating method only solves the cathode/electrolyte interface problem and cannot prevent electrolyte decomposition at voltages beyond its stability window. This issue might not be critical for the cell initially, especially when the cell is cycled at a very high rate, because breakdown of the electrolyte at places other than the cathode interface will initially not degrade cell operation. However, this issue is likely to be detrimental for the long-

term cyclability of all-solid-state batteries. We believe that electrolyte coating provides a more effective approach to prevent both electrolyte decomposition and electrolyte/electrode reaction.

2.7 Conclusion

We presented a methodology that combines computational and experimental tools to investigate the compatibility between solid electrolytes and electrodes. Relatively simple and rapid XRD and SDT experiments were proven to be very effective in describing the interfacial reactions between electrolytes and electrodes. By applying our method to the Na solid-state system, we were able to determine the voltage windows of the electrolytes (both the thermodynamic-driven lower bound and kinetic-stabilized upper bound), understand the thermodynamics and kinetics behind the reactions between incompatible electrolyte/electrode pairs, and select the most stable components ($NaCrO_2$/Na_3PS_4/Na–Sn) within our chemical space for an all-solid-state battery. We believe that these data provide crucial information for new solid electrolyte design and electrolyte/electrode interfacial modification and serve as an essential guide for integrating these components. The methodology and insights obtained in this study can also be applied to other electrochemical systems of interest, such as Li-ion solid-state batteries.

2.8 Detailed methods

Experimental

Synthesis of Na*M*O_2

All the Na*M*O_2 cathode materials were prepared by solid-state synthesis. Stoichiometric amounts of the precursors (typically ~1.0 g) were mixed by ball milling (tungsten carbide ball mill jar, Spex 8000M mixer/mill) and pressed into 1/2-in pellets. The pellets were then placed in alumina boats and heated at a rate of 10°C/min in appropriate atmospheres until the reaction was completed. The corresponding precursors and heating conditions are listed in Table 2.6. The samples (except $NaMnO_2$) were cooled to 150°C at a rate of 30°C/min and immediately transferred to an Ar glovebox. $NaMnO_2$ was quenched to RT after synthesis and then immediately transferred to an Ar glovebox.

Table 2.6: Synthesis conditions of Na*M*O_2 cathode materials

	Precursors	Heating Condition	Reference
$NaCrO_2$	Cr_2O_3 (Sigma–Aldrich, >99.5%), Na_2CO_3 (Sigma–Aldrich, 99%)	900°C in Ar (with 2% H_2) for 10 h	[39]
$NaMnO_2$	Mn_2O_3 (Sigma–Aldrich, >99.5%), Na_2CO_3 (Sigma–Aldrich, 99%)	700°C in air for 9 h	[40]
$NaFeO_2$	Fe_2O_3 (Sigma–Aldrich, >99%), Na_2O_2 (Sigma–Aldrich, 97%)	600°C in air for 20 h	[41]
$NaCoO_2$	Co_3O_4 (Sigma–Aldrich, 99.5%), Na_2O_2 (Sigma–Aldrich, 97%)	550°C in O_2 for 16 h	[42]
$NaNiO_2$	NiO (Sigma–Aldrich, 99%), Na_2O_2 (Sigma–Aldrich, 97%)	650°C in O_2 for 10 h	[43]

Synthesis of Na_3PX_4

Na_2X (X = S, Se, Alfa Aesar, 99.8%), red phosphorus (Sigma–Aldrich, ⩾99.99% trace metal basis), and S/Se (Sigma–Aldrich, 99.99% trace metal basis) powder were mixed in a stoichiometric ratio in an Ar-filled glovebox. The mixture of the three compounds was then loaded into a BN tube (3-mm inner diameter and 4-mm outer diameter). The tube was wrapped with Al foil and sealed with a stainless steel Swagelok cap (3/8 in) at the open end. The synthesis was performed in a sealed alumina tube furnace, which was purged with Ar gas for 20 min, rapidly ramped to 300°C within 10 min, and held at the same temperature for 16 h for the reaction. Continuous Ar gas with a flow rate of ~ 30 mL/min flowed into the sealed furnace during the entire synthesis process. The final products were collected after the furnace was naturally cooled down to RT and were immediately transferred into the glovebox.

Synthesis of chemically desodiated $Na_{0.5}MO_2$

Synthesized pristine $NaMO_2$ powder, over-stoichiometric (ten-fold excess) iodine (GSS, 99.8%, beads), and ~15 mL of acetonitrile (Sigma–Aldrich, 99.8%, anhydrous) were placed in a glass sample vial containing an octagonal magnetic stirring bar. After being wrapped with Al foil to prevent light exposure, the sealed vial was placed on a stirrer and stirred at a speed of 1200 rpm in a Ar glovebox for 4 days. The solution was then centrifuged at 5000 rpm for 7 min. The solid residue was separated from the supernatant and washed with acetonitrile ~6 times until no iodine was observed in the solvent. After drying in the vacuum chamber of the Ar glovebox for ~12 h, the final product was transferred into the glovebox and ground into a powder for further characterization.

Experimental characterization

XRD analysis was performed using a Rigaku Miniflex diffractometer and Cu Kα radiation. The powder sample was first sealed into a Kapton tube (0.9 mm in diameter, Cole Parmer) in the glovebox and then characterized in the diffractometer, which was equipped with a capillary stage to limit air exposure.

SDT measurements were performed using a TA Instruments SDT Q600. Approximately 15 mg of the powder sample was first placed into an alumina sample pan in the glovebox. The filled pan was then placed on the pre-tared cantilever of the analyzer. SDT standard measurements were then performed under continuous Ar flow with a flow rate of 100 mL/min. The measurement procedure usually involves heating and cooling processes. After equilibrating at 25°C, the sample was heated to the set temperature at a heating rate of 5°C/min. The temperature was held for at least 1 h to complete the reaction before cooling was initiated at a rate of 2°C/min. The sample was rapidly transferred to the glovebox after measurement for further characterization.

The working electrode composites were prepared by mixing the synthesized Na_3PX_4 powder, carbon black, and poly(tetrafluoroethylene) (PTFE) in a weight ratio of 80:15:5 with a mortar and pestle in an Ar glovebox. This powder mixture was rolled into a thin film using a stainless steel plate and roller. Circular disks of 5/16-in diameter were then punched with a loading of approximately 3–5 mg. These electrodes were assembled into Swagelok cells with Na metal as the counter electrode and 1 M $NaPF_6$ in a 1:1 (volumetric ratio) ethylene carbonate/diethyl carbonate (EC/DEC) solvent mixture as the liquid electrolyte. Two glass fiber separators were used in the cells. The charging and discharging of the Swagelok cells were performed with an Arbin battery cycler.

Cyclic voltammetry measurements were conducted to investigate the electrochemical stability window of the solid electrolyte Na_3PSe_4. A platinum foil as the working electrode and a sodium

foil as the counter electrode were attached to each face of the pellet. The potential sweep was performed by using a potentiostat/galvanostat device with a scanning rate of 5 mV s^{-1} at room temperature.

XPS measurements were performed on a PHI 5400 ESCA/XPS system with a monochromatic Al Kα X-ray source. The powder samples were mixed with PTFE binder (5 wt%) and rolled into thin films in the Ar glovebox. The films were transferred into the XPS system and cleaned using Ar ion milling (3 kV, 25 mA) to remove surface-absorbed C and O. The core-level spectra were fitted using the commonly applied Gaussian peak shapes and Shirley background correction to extract the transition metal valence states based on the ratio of scaled peak areas.

Computational

The calculations for voltage and interfacial stability generally followed the methodology described in greater detail in reference [114].

Phase diagrams and bulk energies

Zero Kelvin phase diagrams were constructed using the pymatgen software package[161] and a database of DFT-computed bulk phase energies of materials with crystal structures obtained from the Inorganic Crystal Structure Database (ICSD)[162] or generated by applying data-mined chemical substitutions[163]. To obtain these bulk energies, we employed DFT within the projector augmented wave (PAW) formalism[164] using the generalized gradient approximation (GGA)[165] to the exchange-correlation energy as implemented in the Vienna ab initio simulation package (VASP)[166] to calculate the formation energy of each electrolyte from the nearest phases present in the NIST-JANAF[167] or Kubaschewski[168] thermochemical tables or from the elements. To treat the sulfides and selenides equally, we added the formation energy of Na_2Se to this dataset[169]. We uniquely define the nearest phases as those that define the Gibbs triangle (the low-energy facet) containing the desired composition in the phase diagram. As a result of this methodology, the formation energy input to the phase diagram calculation is exactly the experimentally determined enthalpy for compounds that are present in these thermochemical tables. For other compounds, we use the sum of the experimental formation enthalpies of the nearby phases and the DFT calculated reaction energy from these nearby phases to form the compound of interest. This reduces the formation energy error by minimizing electron transfer in the DFT calculated reactions.

For all the VASP calculations, a cutoff energy of 520 eV and a *k*-point grid of at least 500 per number of atoms were used. We applied the mixing scheme of Jain et al.[170] to combine GGA calculations with/without the rotationally invariant Hubbard (+U) correction[171,172] to properly treat insulators and metals.

Voltage stability calculations

To calculate the voltage stability of each electrolyte, we calculated the range of Na chemical potential (μ_{Na}) over which each electrolyte was observed to be on the convex hull and therefore stable in the relevant 0 K grand potential phase diagram. At the extremes of the stability window, we determined its decomposition products as the compositions defining its associated Gibbs triangle. Topotactic Na extraction voltage (upper kinetic stability limit) was calculated by removing a single Na atom from a 4 formula unit supercell, while constraining the lattice dimensions.

Interfacial stability calculations

To determine the interfacial stability, we determine the reaction between electrode and electrolyte compositions with the highest driving force as first proposed by Richards el.[114]. Because arbitrary amounts of either phase can be consumed by this reaction, this process results in a driving force given by the equation

$$\Delta E[c_a, c_b] = \min_{x\in[0,1]}\{E_{pd}[xc_a + (1-x)c_b] - xE[c_a] - (1-x)E[c_b]\},$$

where c_a and c_b are the compositions of the electrode and electrolyte, respectively; E[c_a] and E[c_b] are their bulk energies, respectively; $E_{pd}[c]$ is a function returning the energy of the lowest energy equilibrium of phases at the composition c; and x is a mixing parameter between 0 and 1.

These calculations were not performed at constant Na chemical potential, in slight contrast to the methodologies of reference[114], to more accurately reflect the experimental conditions used in this work.

2.9 Acknowledgments

This work was supported by the Samsung Advanced Institute of Technology. The XPS experiments were performed at the Molecular Foundry, LBNL, supported by the Office of Science, Office of Basic Energy Sciences of the US Department of Energy (Contract No. DE-AC02-05CH11231). This work also used the Extreme Science and Engineering Discovery Environment (XSEDE), which is supported by National Science Foundation grant number ACI-1053575.

Chapter 3 - Characterization of the Mechanical Degradation in All-Solid-State Battery Cathode

3.1 Foreword

The work presented in this chapter has contributions from Tan Shi, Yaqian Zhang, Qingsong Tu, Yuhao Wang, Mary Scott, and Gerbrand Ceder, and will be submitted for publication under the title "Characterization of the Mechanical Degradation in All-Solid-State Battery Cathode".

3.2 Abstract

Solid-state batteries (SSB) promise improved safety and higher energy density and are considered as the ideal energy storage device for electrical vehicle applications. However, their poor cycling stability often leads to rapid capacity fade during cycling. Here, we demonstrate the mechanical instability caused by the cathode volume change plays a significant role in the observed capacity fade. Focus ion beam scanning electron microscope (FIB-SEM) tomography was used to characterize the composite electrode morphology before and after cycling in 3D with nano-scale resolution. The tomography results clearly show the development of voids and cracks near the cathode particles and significant contact loss between the cathode particles and solid electrolyte after cycling. The observed severe mechanical degradation in the electrode composite highlights the difficulty and importance of engineering a mechanically stable ASSB.

3.3 Introduction

Solid-state batteries (SSB) are of interest for energy storage as they would improve safety over Li-ion batteries by replacing the flammable liquid electrolyte with a ceramic solid electrolyte. Potential energy density enhancements are also possible as the solid-state electrolyte may enable the utilization of Li metal.[4,32] However, current SSBs often show rapid capacity fade compared to conventional Li-ion batteries.[35,64,97,173-175] Improving the cyclability of the SSB requires a more comprehensive understanding of the degradation mechanism during cycling.

Both chemical and mechanical instabilities play a role in the capacity fade of SSBs. In this work, we focus on failure modes of the SSB composite cathode which consist of an intimate mixture of solid electrolyte and cathode to provide a transport path for the Li ions to/from the cathode particles. Good Li ion transport across the solid electrolyte–cathode interface is necessary to minimize the cell resistance and overpotential. Chemical reactivity between the solid electrolyte and cathode occurs at this interface and can lead to the formation of a reaction layer, which increases cathode impedance. For example, the sulfide-based electrolyte has been shown to react with oxide-based cathodes, resulting in overpotential growth and capacity fade.[61,62,66,173,176] The coating of the cathode particles has been shown to mitigate this issue to some extent and improve cycling stability.[68,70,71,112,115]

Compared to the chemical instability, the mechanical instability at the solid electrolyte–cathode interface is less studied, but may also cause significant capacity fade. Any loss of contact area between the cathode and solid electrolyte will lead to an increase in cell impedance.[177] The mechanical instability in the cathode composite mainly arises from the volume change of the cathode materials during cycling. Volume changes of up to 8% during cycling are possible for common layered cathode compounds.[78,79] Because the elasticity of a solid electrolyte is extremely small, the only way that the solid electrolyte can accommodate the volume change of the cathode particle is by displacement or irreversible deformation. It is therefore expected that

repeated expansion/contraction of the cathode particles during SSB cycling can lead to contact loss at the solid electrolyte–cathode interface. While there have been some reports on the mechanical degradation in SSB cathode composites,[175,178,179] the severity of the contact loss during cycling is still unclear and requires high-resolution, 3D characterization of the cycled composite cathode. In this study, we use focused ion beam scanning electron microscope (FIB-SEM) based tomography to characterize the microstructure change in the SSB cathode composite after long-term cycling and correlate the mechanical degradation to the resistance growth and capacity fade.

Two of the most common cathode and SE materials, $LiNi_{0.5}Mn_{0.3}Co_{0.2}O_2$ (NMC) and amorphous $75Li_2S$-$25P_2S_5$ (LPS), are used as the cathode and SE in the current study. The cathode material is coated with an amorphous Li-Zr-oxide (LZO) to reduce the reaction between NMC and LPS, and minimize the chemical instability's effect on the electrochemical performance.[70] SSB cells are made with In metal as the anode, a composite of NMC/LPS/carbon nanofiber (CNF) in a weight ratio of 60:35:5 as the cathode, and LPS as the solid electrolyte. The detailed cell fabrication process has been previously reported.[180] The cells are cycled between 1.4 to 3.7 V vs. In (2 to 4.3 V vs. Li/Li^+) using constant current constant voltage (CCCV) charging and constant current discharging at a rate of 0.05 mA cm^2.

3.4 Results

A typical result of SSB cycling is shown in Figure 3.1. In the first 25 cycles, the discharge capacity gradually decreases by about 1 mAh g^{-1} per cycle. However, between 30 to 40 cycles the capacity decreases rapidly to less than 20 mAh g^{-1} (Figure 3.1(a)). Similar cycling behavior has also been observed in other cells, although the sudden drop in capacity can start earlier or later. Figure 3.2 shows the cycling performance of an additional cell with a large capacity drop after ~ 30 cycles.

To investigate whether the capacity degradation is indeed related to a loss of mechanical contact, 300 MPa pressure was reapplied to the cell after cycling for 50 cycles to restore the mechanical contact. Figure 3.1(a) shows that after re-pressing the cell with 300 MPa pressure, the capacity recovered to ~ 80 mAh g^{-1}. This result unambiguously shows that the mechanical degradation is a major contributor to the capacity loss during ASSB cycling. The contact loss created by in the composite cathode leads to a large increase in interfacial resistance, which can be probed by the electrochemical impedance spectroscopy (EIS). Figure 3.1(b) and (c) show the EIS results of the cell after 1, 20, 50, and 51 (after re-pressing) cycles. Each spectrum shows three distinct semicircles at the high, mid, and low-frequency regions. Figure 3.11(d) shows the corresponding fitting results using the equivalent circuit shown in the figure inset. During the first 50 cycles, the resistances in all frequency regions increases. After re-pressing the cell (51^{st} cycle), all resistances show a significant decrease. This general trend suggests that mechanical degradation is not limited to the cathode–solid electrolyte interface, but may also occur at other interfaces such as the anode–solid electrolyte and solid electrolyte grain boundaries. While it is not possible to precisely assign a single frequency region to the cathode–solid electrolyte interface because of the overlapping time constants of different transport processes, previous studies have shown that the midfrequency region is most sensitive to the change at the cathode–solid electrolyte interface.[64] Interestingly, the resistance corresponds to the midfrequency region (R_{MF}) only increased from 954 Ω to 1241 Ω in the first 10 cycles, a 30% increase. After 50 cycles, it further increased to 3283 Ω, a 244% increase. This again demonstrates that the interfacial degradation is accelerated in the later cycles, which agrees with the observed faster capacity decay. After re-pressing, R_{MF} decreased to 2755 Ω, suggesting the poor mechanical contact between the cathode and solid electrolyte contributed to the increased resistance. However, this value is still much larger than the

original R_{MF} after the first cycle, suggesting that other factors, such as chemical degradation at the interfaces, also play a role in the resistance growth.

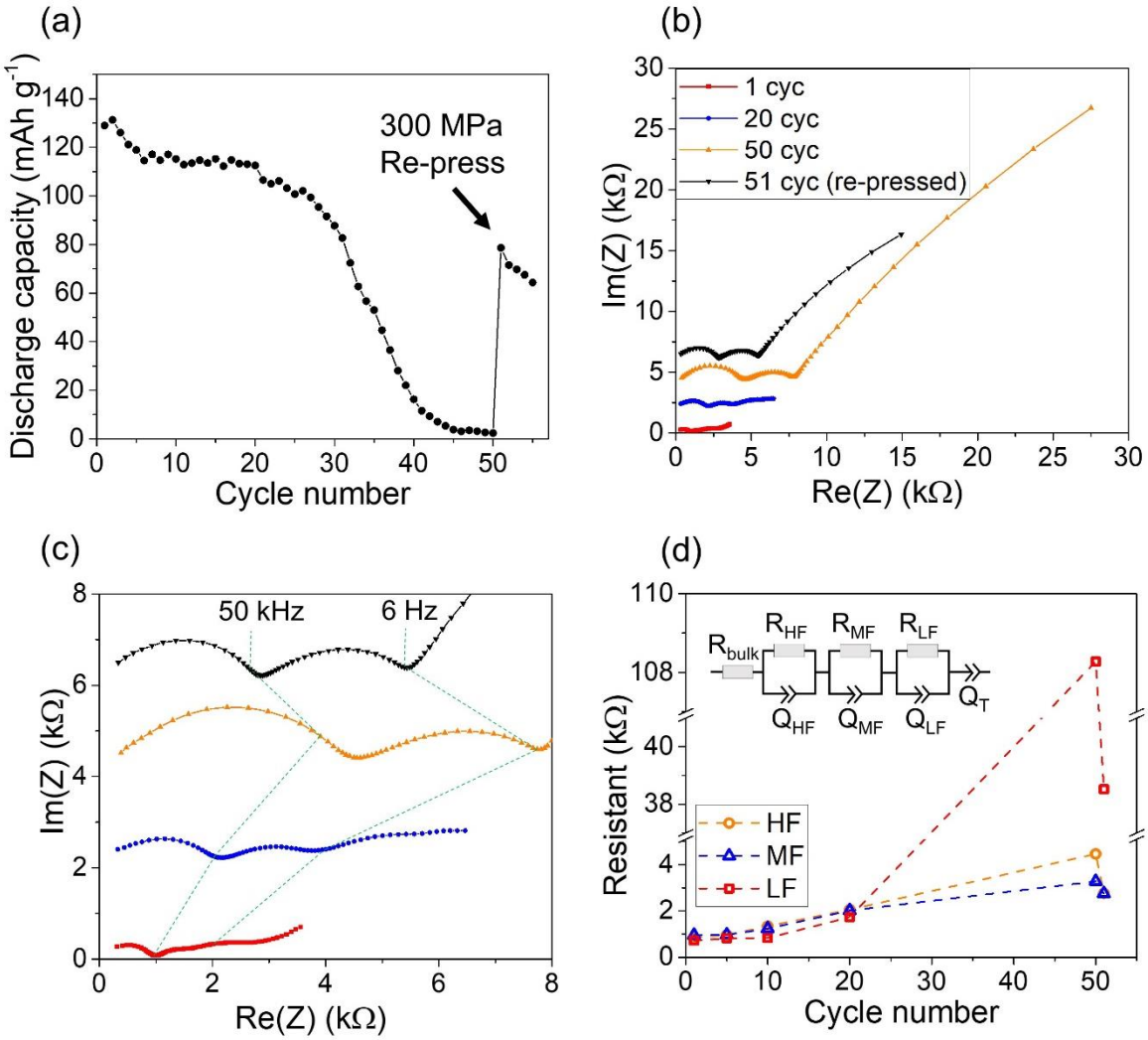

Figure 3.1: Electrochemical tests of a SSB before and after re-pressing. (a) The discharge capacity of the cell. After 50 cycles, 300 MPa pressure was applied. **(b)** and **(c)** EIS measurement after 1, 20, 50, and 51 cycles. **(d)** Equivalent circuit models fitted from the EIS measurements.

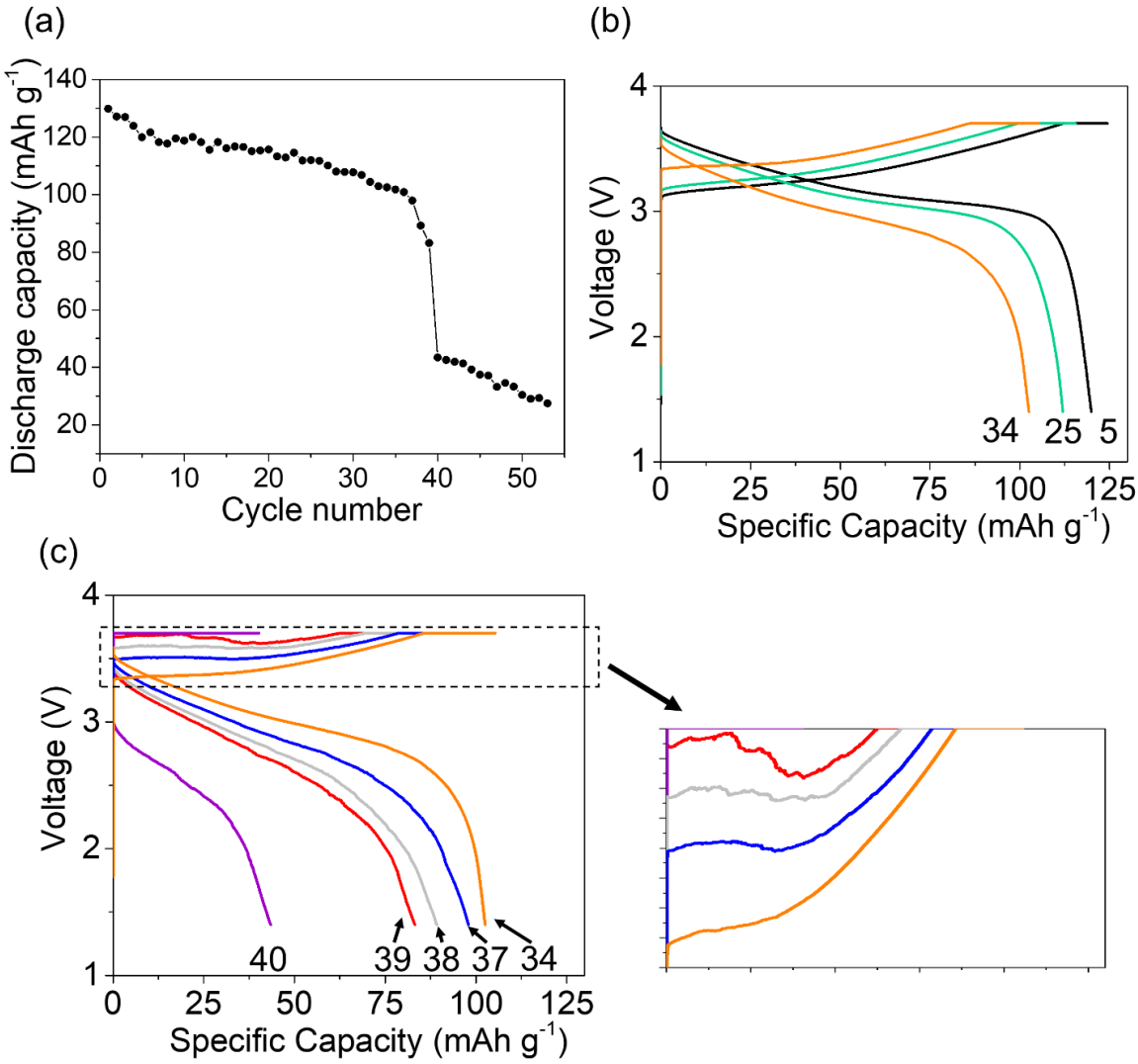

Figure 3.2: Electrochemical cycling results of an additional SSB full cell. **(a)** Cycling performance. **(b)** and **(c)** voltage profiles before and after the sudden drop in capacity. The cycling overpotential slowly increases in the first ~ 30 cycles, leading to the gradual capacity decay, and suddenly accelerated between cycle 35 and 40. It should be noted that the voltage curve also becomes unstable during these cycles, jumping up and down instead of smoothly increasing or decreasing (zoomed-in part of Figure S1(c)). This unstable voltage behavior can be explained by the intermittent Li transport to and from the contracting/expanding cathode particles.

To directly observe and verify the contact loss between the cathode and the solid electrolyte, FIB-SEM tomography was performed to characterize the morphology change in the composite cathode during cycling. Two SSB cells (before cycling and after 50 cycles) were extracted in the discharged state for the FIB-SEM tomography experiment. The workflow for the FIB-SEM tomography experiment is presented in Figure 3.3. The SSB full cell was tilted at a 52° angle with the cathode composite facing the ion beam perpendicular. The ion beam was first used to mill the trenches surrounding the interested area, exposing the cross-section to the top-mounted electron beam at a 52° angle. After an SEM image was taken with an electron beam, a thin slice (50 nm) was milled away from the cross-section with the ion beam, and another SEM image was taken.

After repeating this process for several hundred times, the image stack was processed, combined and reconstructed into 3D volume (see supporting information for the detailed image process procedures). Reconstructed structures of the composite cathodes before cycling and after 50 cycles are shown in Figure 3.4.

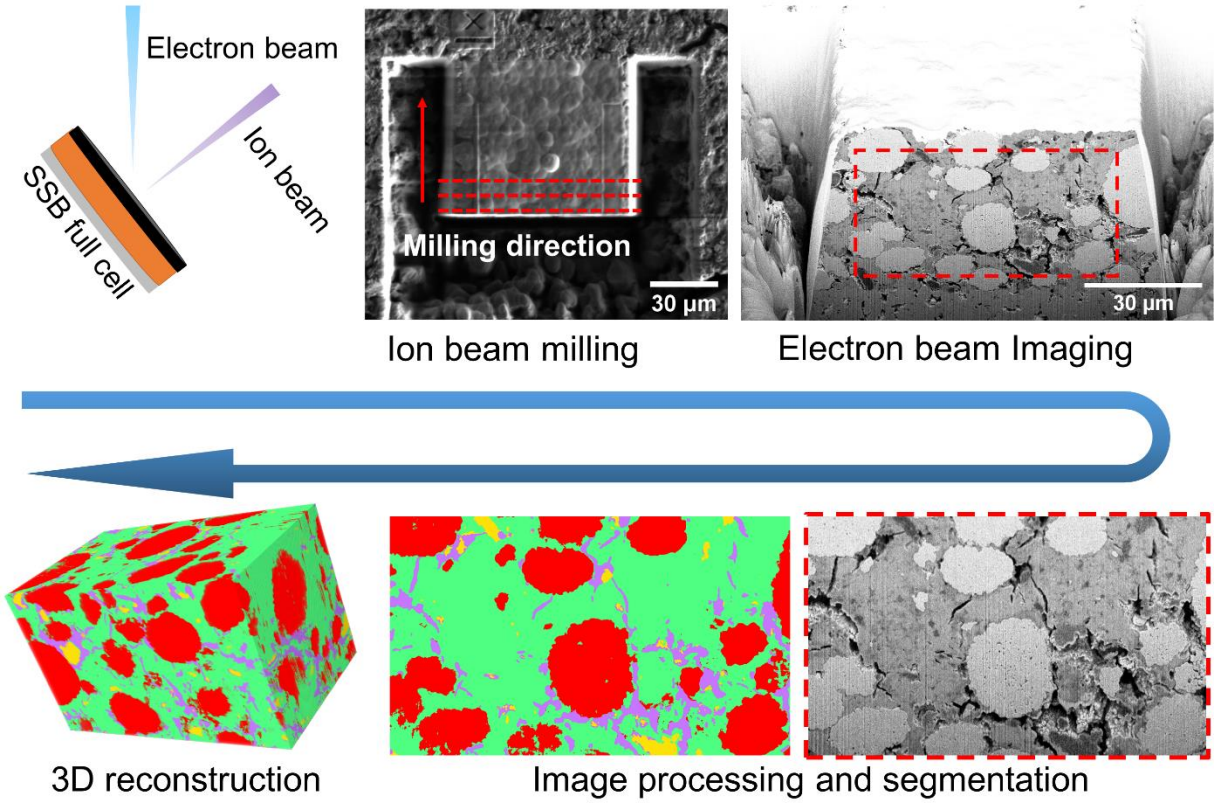

Figure 3.3: Workflow for FIB-SEM tomography. The final 3D volumes are slightly different for the three samples but all in the range of ~ 60×40×30 µm.

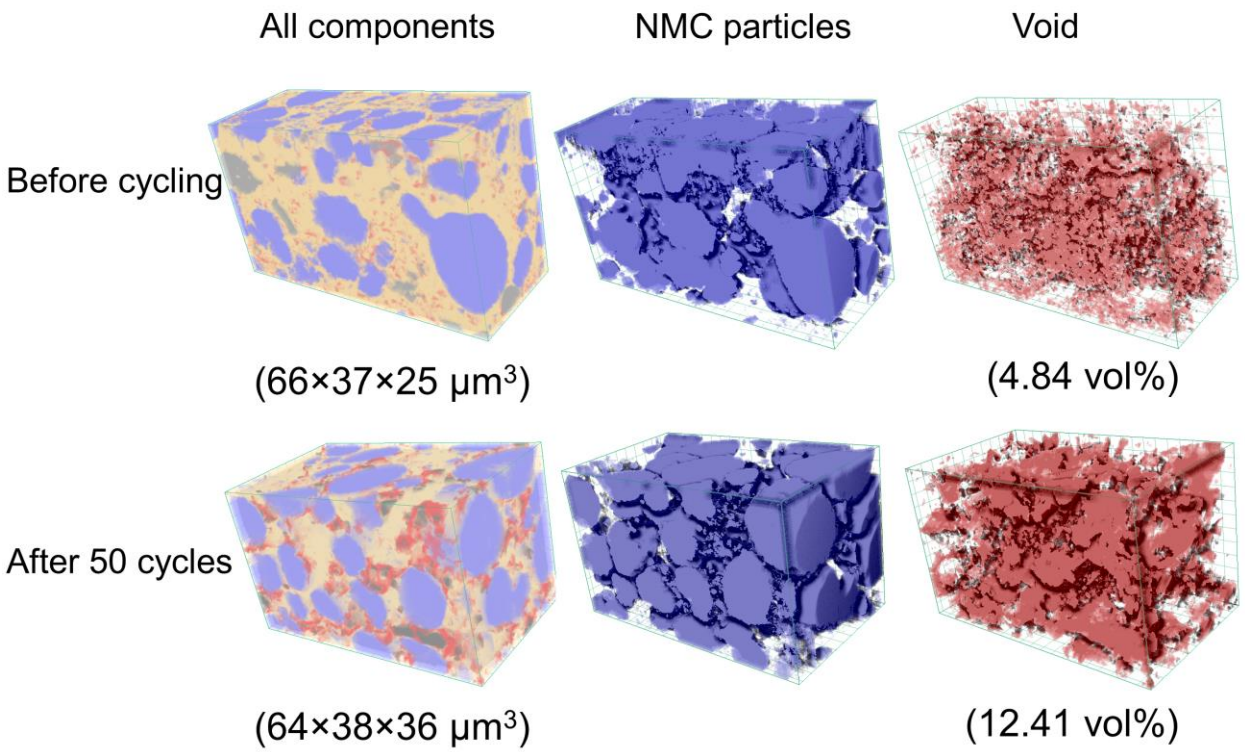

Figure 3.4: Reconstructed 3D structure of the cathode composite. Reconstructed 3D structure of the cathode composite before cycling (top), after 10 cycles (middle) and after 50 cycles (bottom). The left column shows all components (blue: NMC; yellow: LPS; red: void; black: carbon). The middle column shows the NMC particles only and the right column shows voids only. The overall volume and the void volume percent are labeled below the figure.

From Figure 3.4, a noticeable increase in void volume is observed in the after-50-cycle sample, reaching 12.41% of the total volume. To exam the void morphology more carefully, a representative cross-section SEM image is taken for cells before cycling and after 10 and 50 cycles and shown in Figure 3.5(a) through (c). While only small isolated pores exist in the before-cycled sample and after–10–cycles sample, large cracks can be seen next to cathode particles in the after-50-cycle sample (highlighted by the red arrows). The voids are mostly next to the cathode particles, suggesting the repeated volume change of cathode particles during cycling is likely the main driving force for the void formation. The voids near the surface of the cathode particles directly hinder the Li transport between the cathode and solid electrolyte, therefore can lead to a dramatic increase in the overpotential and significant capacity fade.

To better quantify the degree of contact loss at cathode-SE interface after 50 cycles, we divide the cathode surface into two categories base on the segmentation results shown in Figure 3.4: cathode surface in contact with void (contact loss) and cathode surface in contact with other components such as other cathode, SE, or carbon (with contact). Figure 3.5(c) demonstrates the two categories in the cross-section image shown in Figure 3.5(b) with the contact loss surfaces highlighted in red and other cathode surfaces in blue. This analysis was performed on all images of the after–50–cycle sample and the reconstructed 3D structure of the cathode surfaces with contact (blue) and without contact (red) is shown in Figure 3.5(d). The contact loss area is

distributed across the volume and can be found on most of the cathode particle surfaces, demonstrating the severity of the mechanical instability. The estimated contact loss area is 10.4% of the total cathode surface area.

Figure 3.5(d) also shows that the contact loss areas do not seem to be uniformly distributed around the spherical cathode particles. To better visualize the contact loss distribution around a cathode particle, the voids around a single NMC particle in the after–50–cycle sample are isolated from the larger volume and shown in Figure 3.5(e). The spherical NMC particle in the center is shown in grey, and the surrounding voids are shown in red. The voids are much more concentrated on the right side compared to the left side of the NMC particle, suggesting the contact loss areas caused by the cathode particle volume shrinking will mostly be on one side of the particle, rather than uniformly distribute around the particle. This is because that the voids on one side of the particle is sufficient to release the strain caused by the particle volume change.

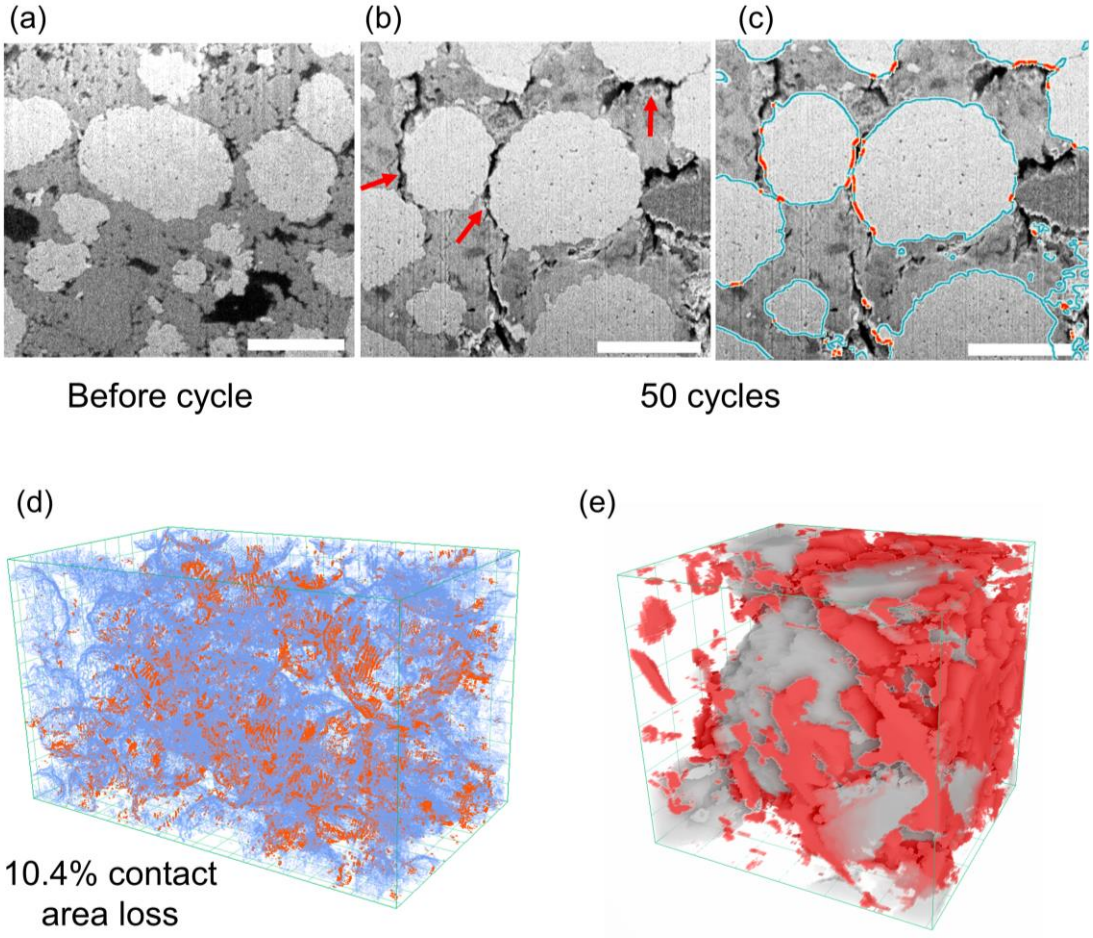

Figure 3.5: The contact loss between cathode and SE. Cross section SEM images of the composite cathode **(a)** before cycle, **(b)** after 50 cycles. **(c)** NMC surfaces (blue) with void-NMC interfaces highlighted in red and **(d)** its reconstruction in 3D. **(e)** A part of the 3D reconstruction of after–50–cycle sample showing an isolated NMC particle (grey) with surrounding voids (red). Other components (LPS and carbon) are not shown.

3.5 Discussion

The FIB-SEM tomography and electrochemical testing results together reveal the severe mechanical degradation in the ASSB composite electrode, particularly at later cycles. The cause for the accelerated mechanical degradation at the later cycles is still unclear. One likely reason is that mechanical degradation can be worsened by continuous chemical degradation at the interface. Severe chemical reactions the cathode–solid electrolyte interface has been widely reported. The growth of an interfacial layer composed of various reaction products can weaken the mechanical adhesion between cathode and solid-electrolyte, promoting the crack development under stress.

While server mechanical degradation was observed within the first 50 cycles of SSB cycling, we note that many factors will likely modify this mechanical degradation behavior, including the cathode chemistry/structure, cathode morphology, SE mechanical property, and external pressure. Optimizing these factors will likely result in improved mechanical stability in SSBs. For example, it has been shown that different cathode chemistries and structures can lead to different volume change during cycling.[79,181] Electrode materials with small volume change or "zero–strain" would be ideal for the improvement of mechanical stability. Additionally, the cathode particle morphology can also be better optimized. Engineering secondary cathode particles with some porosity between primary particles may result in a reduced volume change compared to the fully dense particles. The large cathode particle size used in the current study (~ 12 μm diameter) also creates a larger surface displacement, and therefore a larger strain for the SE. Utilizing a smaller particle size cathode material may reduce the severity of the mechanical degradation observed in the current study. Different SE material will also lead to different mechanical degradation behavior. For example, the rapid development of cracks in the first few cycles has been observed in SSBs with oxide-based SE, which is more rigid compared to sulfide SE used in the current study.[179] Therefore, developing a SE with higher elasticity is one route to lessen the mechanical instability. Finally, applying an external pressure (stack pressure) large enough to deform the SE can also prevent the void formation. However, such a high pressure may not be practical for large format cells.

3.6 Conclusion

Using FIB-SEM tomography, we characterized the SSB composite cathode morphology and revealed the severe mechanical degradation during cycling. A large amount of void volume (~ 12%) is found in the cathode composite after 50 cycles. These voids are mostly distributed near the cathode particle surfaces, leading to contact area loss over 10%. The observed rapid capacity drop in later cycles is attributed to this contact loss between cathode and SE. Our results also suggest, somewhat surprisingly, that mechanical degradation does not progress gradually starting from the first cycle. Instead, the majority of the void formation and contact loss likely occurs at later cycles and over a short time.

3.7 Detailed methods

Materials synthesis and characterization: $LiNi_{0.5}Mn_{0.3}Co_{0.2}O_2$ (NMC) and $75Li_2S–25P_2S_5$ (LPS) were used as the cathode (CAM) and SE material, respectively. NMC powder ($\overline{D}_{CAM}$ = ~12 μm) was purchased from MSE Supplies LLC. The 6 - 8 nm $Li_2O–ZrO_2$ (LZO) coating was applied to both NMC powders by Samsung Research Japan using the procedure described by Ito *et al.*[70] The LPS was synthesized by ball milling stoichiometric amounts of Li_2S (99.98% Sigma-Aldrich) and P_2S_5 (99% Sigma-Aldrich) in a 50-mL ZrO_2 jar for 200 min using a SPEX 8000M mixer mill.

LPS with small particle size used in the composite cathode was prepared by wet ball milling the LPS SE with heptane and dibutyl ether using a Retsch PM200 ball mill for 40 hours. All LPS synthesis steps were conducted in an Ar atmosphere.

Cell fabrication and testing: Solid-state cells were fabricated in an Ar-filled glovebox (H_2O < 0.1 ppm and O_2 < 0.1 ppm). The composite cathode was fabricated by first hand-mixing the 60 mg of the LZO-coated NMC particles and 35 mg of the small particle LPS for ~10 min. 5 wt% CNFs (from Samsung Research Japan) was then added and mixed in for another ~10 min. The cell was assembled using a custom-made pressure cell. A polyether ether ketone (PEEK) cylinder with an inner diameter of 8 mm is used as the insulating body, and two 8-mm-diameter stainless-steel rods are used as current collectors. 35 mg of LPS electrolyte was added and compressed under ~100-MPa pressure. The cathode composite (~ 5 mg) was then spread evenly on top and compacted under ~ 300-MPa pressure. Finally, an 8-mm-diameter piece of In metal was attached as the anode, and ~100-MPa pressure was again applied. The cell was sealed in an Ar-filled jar and cycled under ~5-MPa pressure provided by a spring.

Cell cycling was performed using a Bio-Logic VMP300 system. For all the cells, the cycling voltage window was 2–3.7 V vs. In metal and current density was 0.05 mA/cm^2. Constant current constant voltage (CCCV) charging was used, where the cell was held for 5 hours at the top-of-charge state.

FIB-SEM characterization: FIB-SEM was performed on the FEI Helios G4 dual beam FIB system equipped with Ga^+ ion beam. The consecutive slice milling and image requisition were performed using the FEI Slice and View software.

Image processing and reconstruction: The resulting SEM image stacks were first rescaled to compensate for the 52° angle between the electron beam and the sample cross-section. Then several representative slices were selected, and manual segmentation of different components (NMC, LPS, carbon, and void) was performed. The manually segmented images were used to train a classifier using the Trainable Weka Segmentation plugin in the ImageJ software, which was then used to segment the whole image stack. All 3D reconstruction and visualization were done using the Dragonfly software.

3.8 Acknowledgments

This work was supported by the Samsung Advanced Institute of Technology. The FIB-SEM experiments were performed at the Molecular Foundry, LBNL. Work at the Molecular Foundry was supported by the Office of Science, Office of Basic Energy Sciences, of the U.S. Department of Energy under Contract No. DE-AC02-05CH11231.

Chapter 4 - High Active Material Loading in All-Solid-State Battery Electrode via Particle Size Optimization

4.1 Foreword

The work presented in this chapter was published by T. Shi, Q. Tu, Y. Tian, L. J. Miara, O. Kononova, G. Ceder, in *Advanced Energy Materials*, vol. 10, article number 1902881 (2020), and is reproduced here with the permission of co-authors.

4.2 Abstract

Low active material loading in the composite electrode of all-solid-state batteries (SSBs) is one of the main reasons for the low energy density in current SSBs. In this work, we demonstrate with both modeling and experiments that in the regime of high cathode loading, the utilization of cathode material in the solid-state composite is highly dependent on the particle size ratio of the cathode to the solid-state conductor. Our modeling, confirmed by experimental data, shows that higher cathode loading and therefore an increased energy density can be achieved by increasing the ratio of cathode to conductor particle size. These results are consistent with ionic percolation being the limiting factor in cold pressed solid-state cathode materials and provide specific guidelines on how to improve the energy density of composite cathodes for solid state batteries. By reducing SE particle size and increasing the CAM particle size, we are able to experimentally achieve over 50 vol% CAM loading with high CAM utilization, demonstrating that a commercially-relevant, energy-dense cathode composite is achievable through simple mixing and pressing method.

4.3 Introduction

All-solid-state batteries (SSBs) have become an exciting energy storage technology to replace conventional lithium-ion batteries.[32,182] They improve safety by removing organic carbonate-based liquid electrolytes and can potentially increase energy density by utilizing a Li-metal anode.[4] However, while proof of concept of SSBs has been shown, multiple hurdles still have to be overcome before they can truly compete with today's commercialized Li-ion cells in terms of energy density.[32] In this paper, we focus on active material loading in the cathode as one of these challenges. Composite cathodes for SSBs are typically made up of the cathode active material (CAM), a solid electrolyte (SE), and carbon, and can be fabricated in multiple ways, the simplest one of them consisting of mixing the three components and then pressing or sintering them together with the bulk SE/separator layer.[35,70,183,184] However, because of the large solid-electrolyte fraction (30 wt%–50 wt%) typically required in cathode composites to provide sufficient ionic diffusion,[35,70,185,186] the volume fraction of cathode (cathode loading) of current SSBs is low, resulting in low energy density. Considering that the cathode loading of liquid cells is typically greater than 90 wt% (or 50 vol%),[187,188] achieving full capacity in an energy-dense electrode (with >50 vol% CAM loading) is vital for SSBs to be competitive with conventional lithium-ion batteries. An optimal composite cathode morphology should have minimal void space and good cathode/SE contact, and include the minimum amount of SE needed to ensure sufficient Li diffusion between the active material and bulk electrolyte. Several studies have separately demonstrated that the CAM and SE particle sizes affect the morphology of a cold-pressed cathode composite as well as the full cell performance.[81-83,183]

Using experiments and modeling, we demonstrate in this work that, somewhat surprisingly, very high volume fractions of cathode can be fully utilized in a composite cathode as long as the ratio of the SE to cathode particle size is controlled. We find that the most critical factor to obtain high energy density is to keep the SE particle size smaller than that of the active cathode material. By reducing the conductor particle size by a factor 2-3 the cathode utilization can improve from 20% to 100% even at high total cathode loading. The higher the volume loading of cathode the smaller the ratio of SE to cathode size needs to be.

Our modeling results are verified using Li_2O–ZrO_2 (LZO)-coated $LiNi_{0.5}Mn_{0.3}Co_{0.2}O_2$ (NMC) as the CAM and amorphous $75Li_2S$–$25P_2S_5$ (LPS) as the SE. Using small-particle-size LPS ($\overline{D}_{SE}$ ~ 1.5 μm) and large-particle-size NMC ($\overline{D}_{CAM}$ ~ 12 μm), we were able to dramatically increase cathode loading towards a commercially viable level without sacrificing specific capacity. Our results provide simple design guidelines to improve the energy density of solid-state batteries by achieving high active material loading in the cathode.

4.4 Computational and experimental methods

Microstructural Modeling

We systematically studied the relation between active cathode loading (f_{CAM}), cathode utilization (θ_{CAM}), and the particle size of the active cathode material and SE through a basic model for the composite cathode. Numerical representations of 3D electrode microstructures are generated by randomly inserting spherical CAM and SE particles into a cubic simulation domain (V_{Box}), as shown in Figure 4.1**a**. Electronic conductive agents such as carbon nanofibers (CNFs) are not included in the model as the current study focuses on ionic percolation in the cathode composite.

The weight fractions of CAM and SE are defined as $f_{CAM} = \frac{0.95\, M_{CAM}}{M_{CAM}+M_{SE}}$ and $f_{SE} = \frac{0.95\, M_{SE}}{M_{CAM}+M_{SE}}$, where M_{CAM} and M_{SE} are the weights of the CAM and SE, respectively. The pre-factor (0.95) is used to account for the 5 wt% CNF used in our experimental cells, but not explicitly included in our model. The standard log-normal distributions particle size distributions used in the simulation have average particle diameter $\overline{D}_c$ and standard deviation σ_c (c is either CAM or SE), and are shown in Figure 4.1**b**. They match the scanning electron microscopy (SEM) measurements of our experimental material as close as possible and are of similar form to what has been used in other studies.[183,189]

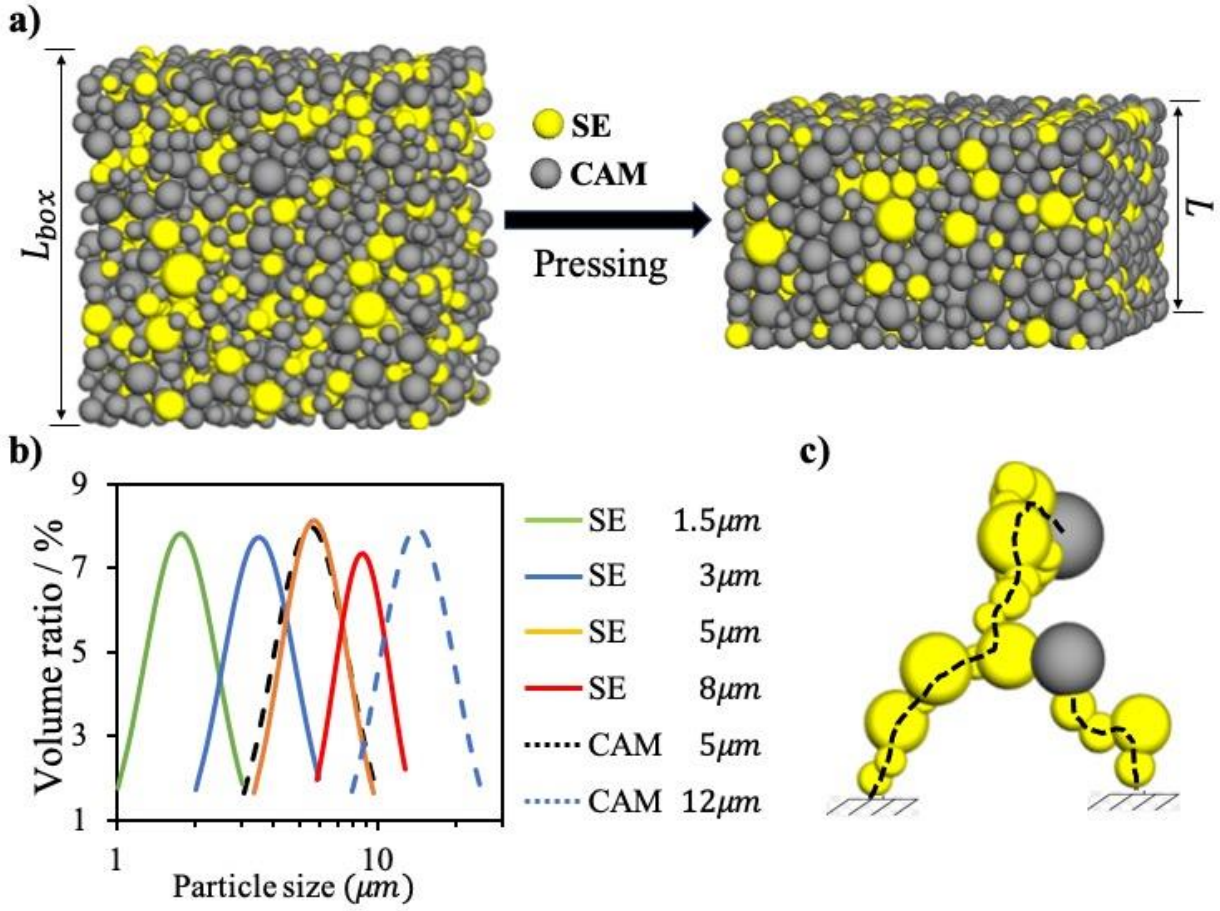

Figure 4.1. Computation model. **a)** Example microstructures showing the composite cathode from its initial cubic shape (top-left, with box size L_{box}) to its final compact shape (bottom-left, with height L) under a pressing pressure of 200MPa. The model was built using the following parameters: $f_{CAM} = 80$wt%, $\overline{D}_{SE} = 5\ \mu m$, $\overline{D}_{CAM} = 5\ \mu m$. **b)** Particle size distributions used in the simulation. The average particle diameters and standard deviations measured from the SEM images were used as inputs in the log-normal distributions. **c)** Ionic percolating paths for two typical CAM particles (black dash lines). The paths connect CAM particles to the composite cathode/bulk SE interface (bottom of the simulation box).

A discrete element method (DEM) implemented in the open source package LIGGGHTS was used to simulate the pressing process in the experiment.[190-192] Granular contact walls were placed at the bottom and all four vertical boundaries of the box. A flat surface was applied at the

top of the simulation box and moved downward at a prescribed velocity until the system reaches a specified pressure of 200 MPa. Pressure was then held constant until the system reaches static equilibrium (i.e., the kinetic energy of the system decayed to zero). The Hertzian granular contact potential was used to describe the normal and tangential interactions and damping forces[193] as well as the frictional yield.[194] The Hertzian contact force used in the discrete element method to simulate the pressing process is described by the following equation:

$$\boldsymbol{F}_{ij} = \sqrt{\delta}\sqrt{\frac{R_i R_j}{R_i + R_j}}\left[\underbrace{\left(k_n \delta \boldsymbol{n}_{ij} - \gamma_n (\boldsymbol{v}\cdot\boldsymbol{n}_{ij})\boldsymbol{n}_{ij}\right)}_{Normal\ force} + \underbrace{\left(k_t \delta \boldsymbol{t}_{ij} - \gamma_t (\boldsymbol{v}\cdot\boldsymbol{t}_{ij})\boldsymbol{t}_{ij}\right)}_{Tangential\ force}\right],$$

where $\boldsymbol{F}_{ij}$, $\boldsymbol{n}_{ij}$, and $\boldsymbol{t}_{ij}$ are the contact force, normal directional vector, and tangential directional vector between particles i and j, respectively; R_i and R_j are the radii of particles i and j, respectively; δ is the overlap distance between two particles defined as $\delta = d - (R_i + R_j)$, where d is the central distance between two particles; $\boldsymbol{v}$ is the relative velocity of two particles; and $\boldsymbol{v}\cdot\boldsymbol{n}_{ij}$ and $\boldsymbol{v}\cdot\boldsymbol{t}_{ij}$ are the components of the relative velocity along the normal and tangential directions, respectively.

In our experiment, LPS was selected as the SE material and NMC was selected as the CAM material. The properties of the SE and CAM used in this study were taken from the literature and are summarized in Table 4.1

Symbol	***Description***	***Value***	
		SE	**AM**
E_c *(GPa)*	Young's modulus	18.5[72]	177.5[195]
ν	Poisson's ratio	0.3[72]	0.3[195]
ρ (g/cm^3)	Density	1.87[196]	4.85[195]
γ_t *(GPa)*	Damping constant	50[194]	25[194]
σ_y *(GPa)*	Yield stress	2[72]	12.6[195]

Table 4.1. Simulation parameters used in the Hertzian contact model

Because Li-ion diffusion is much faster in the SE than in the CAM,[197] we only consider Li-ion percolation pathways through SE particles.[198] A CAM particle is considered to be "active" if at least one Li percolation pathway connects it to the bulk SE layer (as shown in Figure 4.1**b**). To analyze whether a CAM particle is active or inactive, we first built networks of CAM particles by connecting each node (CAM or SE particles) with its neighbors and then defined CAM particles as source nodes and SE particles located at the bottom boundary as target nodes.[199] From the network, we extract the shortest percolating pathway of each active CAM particle to a SE target particles. The active CAM fraction (θ_{CAM}) in a cathode composite is the ratio of the volume of the active CAM particles to the total CAM volume ($\theta_{CAM} = V_{CAM}^{active}/V_{CAM}$). The result for each condition was averaged using at least three different random initial configurations.

The convergence of the percolation results with the simulation box size is discussed here. As shown in Figure 4.2**a**, when the box size was too small, the particle size distributions of the generated model deviated from the designed distributions. This deviation increased as the maximal particle size increased.

As shown in Figure 4.2**b**, four composite models (Model 1: CAM-5μm/SE-1.5μm, Model 2: CAM-5μm/SE-3μm, Model 3: CAM-12μm/SE-5μm and Model 4: CAM-12μm/SE-8μm) with fixed mass ratio (CAM:SE=80:15) were filled into eleven cubic cathode boxes of length *L*. Detailed statistic descriptions of each particle size are shown in Table 4.2:

Material	Average size (μm)	Distribution function	Standard deviation σ (μm)	Minimal diameter (μm)	Maximal diameter (μm)
CAM	5	Log-normal	1.6	3.0	10.0
	12		3.5	5.0	25.0
SE	1.5		0.5	0.8	3.0
	3		1.0	2.0	6.0
	5		1.5	3.2	10.0
	8		2.0	5.8	13.0

Table 4.2. Detailed parameters for the statistic distribution of each particle sizes.

Because the box-size errors are mainly determined by the largest particles, Model 1 and Model 2 shared the same box length *L* (first line of the horizontal axis labeled as CAM-5) and Model 3 and Model 4 shared the same box length *L* (second line of the horizontal axis labeled as CAM-12). Large errors were observed for $L < 50\ \mu m$ for the AM-5μm models and for $L < 120\ \mu m$ for the AM-12μm models. The following empirical conclusion was thus drawn: for a composite model with maximal particle diameter d_{max}, the minimal length for the simulation box is $L_{min} \approx 10\overline{D}_{max}$. The box sizes of all the models used in the study were conservatively set to be 1.5-times larger than the critical minimal box size: $L_{box} = 1.5L_{min} \approx 15\overline{D}_{max}$.

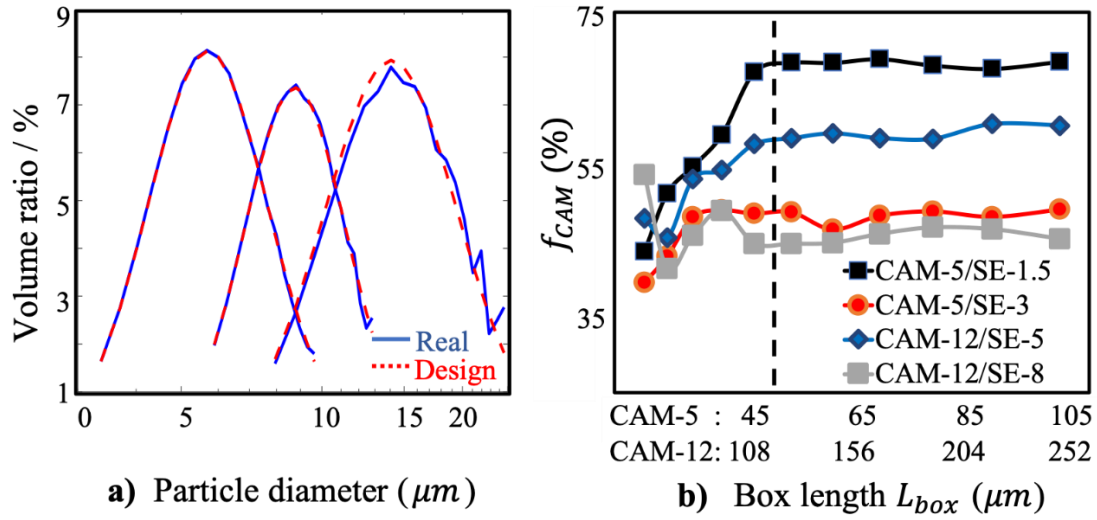

Figure 4.2. Box size convergence tests. **a)** Size distributions of three types of particles. The dashed red lines represent the theoretically designed distributions, and the solid blue lines represent the real distribution after filling these particles into a cubic box of 30-μm length. **b)** Active cathode ratios of four composite models with mass ratio of AM:SE=80:15 as a function of cubic length. Models CAM-$5\mu m$/SE-$1.5\mu m$ and CAM-$5\mu m$/SE-$3\mu m$ share the cubic length of the first horizontal axis, and models CAM-$12\mu m$/SE-$5\mu m$ and CAM-$12\mu m$/SE-$8\mu m$ share the cubic length of the second horizontal axis.

Experimental Details

Materials synthesis and characterization: In our experiments, NMC and LPS were used as the cathode (CAM) and SE material, respectively. Small-sized NMC powder ($\overline{D}_{CAM}$ = ~5 μm) was provided by Samsung Research Japan, and large-sized NMC powder ($\overline{D}_{CAM}$ = ~12 μm) was purchased from MSE Supplies LLC. The 6 - 8 nm LZO coating was applied to both NMC powders by Samsung Research Japan using the procedure described by Ito *et al.*[70] The LZO-coated NMC has been shown to minimize the interfacial reaction between NMC and LPS, allowing the current study to mainly focus on the particle size effect. The bulk LPS SE used as the separator was synthesized by ball milling stoichiometric amounts of Li_2S (99.98% Sigma-Aldrich) and P_2S_5 (99% Sigma-Aldrich) in a 50-mL ZrO_2 jar for 200 min using a SPEX 8000M mixer mill. The resulting LPS SE shows an ionic conductivity of 0.39 mS cm^{-1}, consistent with previous reports.[45] The small-particle-size LPS used in the cathode composite was prepared by wet ball milling the LPS SE with heptane and dibutyl ether using a Retsch PM200 ball mill.[183] LPS particles with different average diameters were prepared using ZrO_2 balls ranging in size from 1 to 10 mm under different ball-milling conditions. The detailed preparation conditions and the ionic conductivities of the small particle LPS are provided in Table 4.3. We note that the ionic conductivities of the LPS decreases with smaller particle sizes. This is likely because of the increased grain boundary (or particle boundary) resistant, which can be worsened by any residual solvent from wet ball milling process. LPS with four different average particle sizes (8, 5, 3, and 1.5 μm) was tested with LZO-coated NMC particles with average particle sizes of 5 and 12 μm. Representative SEM images of all the particles are presented in Figure 4.3.

The SEM images were obtained using a Zeiss Gemini Ultra-55 analytical field-emission scanning electron microscope, and were used to estimate the particle sizes. For each sample, the diameters of ~200 random particles were measured, and the average value was recorded.

Average size (μm)	Ball mill model	Ball size (mm)	Ball milling speed	Solution	Ball milling time (h)
8	SPEX 8000M	5	1060 cycles/min	Heptane	1
5	SPEX 8000M	3	1060 cycles/min	Heptane	1.5
3	Retsch PM200	3 and 1	300 rpm	Heptane + Dibutyl Ether	15
1.5	Retsch PM200	1	300 rpm	Heptane + Dibutyl Ether	40

Table 4.3. Detailed wet-ball-milling conditions used to obtain various sized LPS particles. In all cases, 50-mL ZrO_2 ball-mill jars and Y-stabilized ZrO_2 milling balls were used.

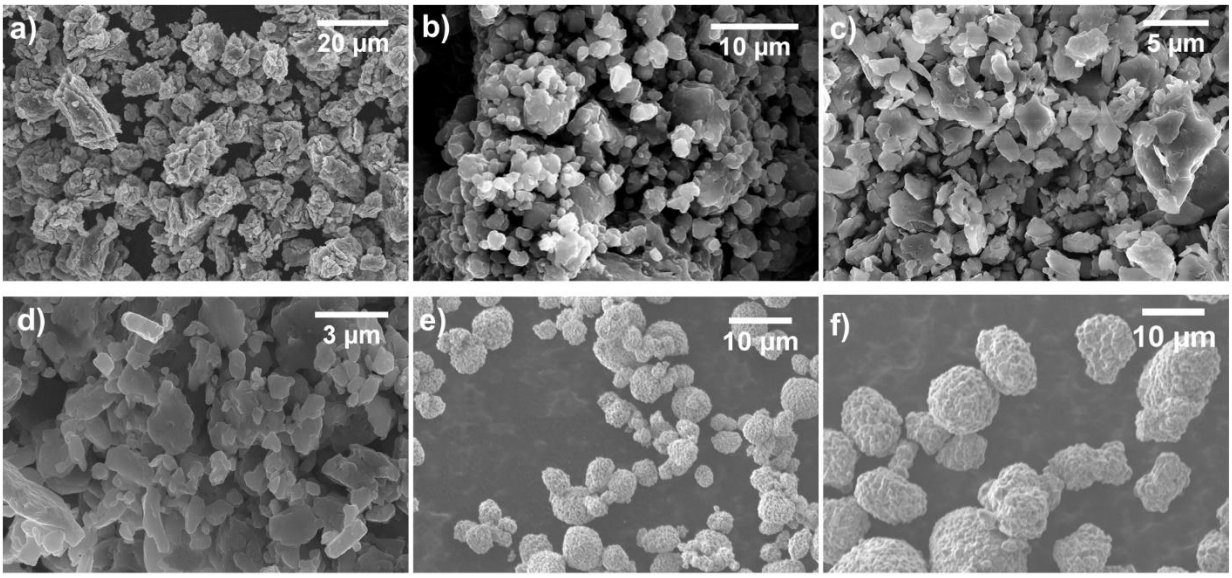

Figure 4.3. Particle size characterization. **a–d)** SEM images of LPS with average particle diameters of a) 8 μm, b) 5 μm, c) 3 μm, and d) 1.5 μm prepared using different wet-ball-milling conditions. **e–f)** SEM images of LZO-coated NMC cathode particles with average diameters of e) 5 μm and f) 12 μm.

Cell fabrication and testing: Solid-state cells were fabricated in an Ar-filled glovebox (H_2O < 0.1 ppm and O_2 < 0.1 ppm). The composite cathode was fabricated by first hand-mixing the LZO-coated NMC particles and LPS for ~10 min and then mixing them for another ~10 min after adding 5 wt% CNFs (from Samsung Research Japan). The cell was assembled using a custom-made pressure cell consisting of a polyether ether ketone (PEEK) cylinder with an inner diameter of 8 mm and two 8-mm-diameter stainless-steel rods as current collectors. The cell was made by closing one end of the cylinder with a current collector. Bulk LPS electrolyte (35 mg) was added

and compressed under ~100-MPa pressure. The cathode composite (~ 5 mg) was then spread evenly on top and compacted under ~ 200-MPa pressure. Finally, an 8-mm-diameter piece of In metal was attached as the anode, and ~200-MPa pressure was again applied. The cell was sealed in an Ar-filled airtight jar and cycled under ~5-MPa pressure provided by a spring.

Cell cycling was performed using a Bio-Logic VMP300 system. For all the cells, the cycling voltage window and current density were set to 2–3.7 V vs. In metal and 0.05 mA/cm^2, respectively.

4.5 Results

Influence of Particle Size Ratio and Cathode loading on CAM Utilization

The model results for the effect of cathode loading on the CAM utilization (θ_{CAM}) at fixed relative particle size ($\lambda = 1.67$) are shown in Figure 4.4**a**. For low f_{CAM} (< 70 wt%), the CAM particles are fully utilized ($\theta_{CAM} = 1$). However, upon increasing the cathode loading above 75 wt%, the cathode utilization decreases drastically. This result is consistent with the idea that Li percolation will weaken as the amount of SE in the composite is reduced. However, for a given λ, there is a corresponding maximum f_{CAM} that still enables full CAM utilization ($f_{CAM} =$ ~70 wt% in this case). We show below that the critical cathode loading at which percolation disappears depends strongly on the SE particle size.

The effect of λ on cathode utilization at fixed f_{CAM} (70 wt%) is shown in Figure 4.4**b**. Specifically, we fixed the CAM particle size to 5 μm and determined θ_{CAM} for a series of SE particle sizes (1.5, 3, 5, 8, 12, and 15 μm). Somewhat surprisingly, the cathode utilization can vary between 20% and 100% at fixed cathode loading, simply by changing the SE particle size. Percolation clearly decreases when $\lambda < 1$. An important observation from Figure 4.4**b** is that a minimum value of λ is required to achieve full CAM utilization at a given cathode loading ($\lambda = 1.67$ in this case). To confirm that this effect is indeed caused by the change in λ rather than the SE particle size alone, we also calculated similar data using 12 μm CAM particles and obtained the same results (Figure 4.5).

Figure 4.4**a** and **b** clearly show that cathode utilization is affected by both λ and f_{CAM}. To quantitatively understand this effect, we varied both λ and f_{CAM} and determined the corresponding value of θ_{CAM}. Our findings are summarized in Figure 4.4**c** and indicate that percolation in the cathode composite consistently improves as f_{CAM} decreases (or as the SE weight fraction increases, moving from top to bottom) and as λ increases (moving from left to right). Therefore, *to achieve high capacity in a SSB with high cathode loading a large value of λ should be used*. In addition, independent of f_{CAM}, percolation always significantly worsens for $\lambda < 1$, stressing that under all circumstances the SE particle size should be kept smaller than the cathode particle size, which is in direct contrast to the desire for high particle size SE in the separator. Additionally, Figure 4.4**c** shows that the benefits of λ reduction are very dependent on the cathode loading for which one is trying to optimize: for $f_{CAM} = 80$ wt%, increasing λ from 1 to 3 doubles θ_{CAM} from ~30% to ~60%, but at $f_{CAM} = 85$ wt% increasing λ from 1 to 8 only slightly increases θ_{CAM} from ~16% to ~20%.

These simulation results can be summarized in a set of practical design criteria to create high energy density solid state batteries as shown in Fig 3**d**. For each desired cathode loading and utilization there is a minimum cathode to SE particle size that needs to be used to create the composite. For example, to achieve 98% cathode utilization with 75wt% loading $\lambda_{min} = 2.1$. For typical NMC cathode sizes of 5 or 20μm, this corresponds to a SE particle size of 2.4 and 9.5 μm respectively.

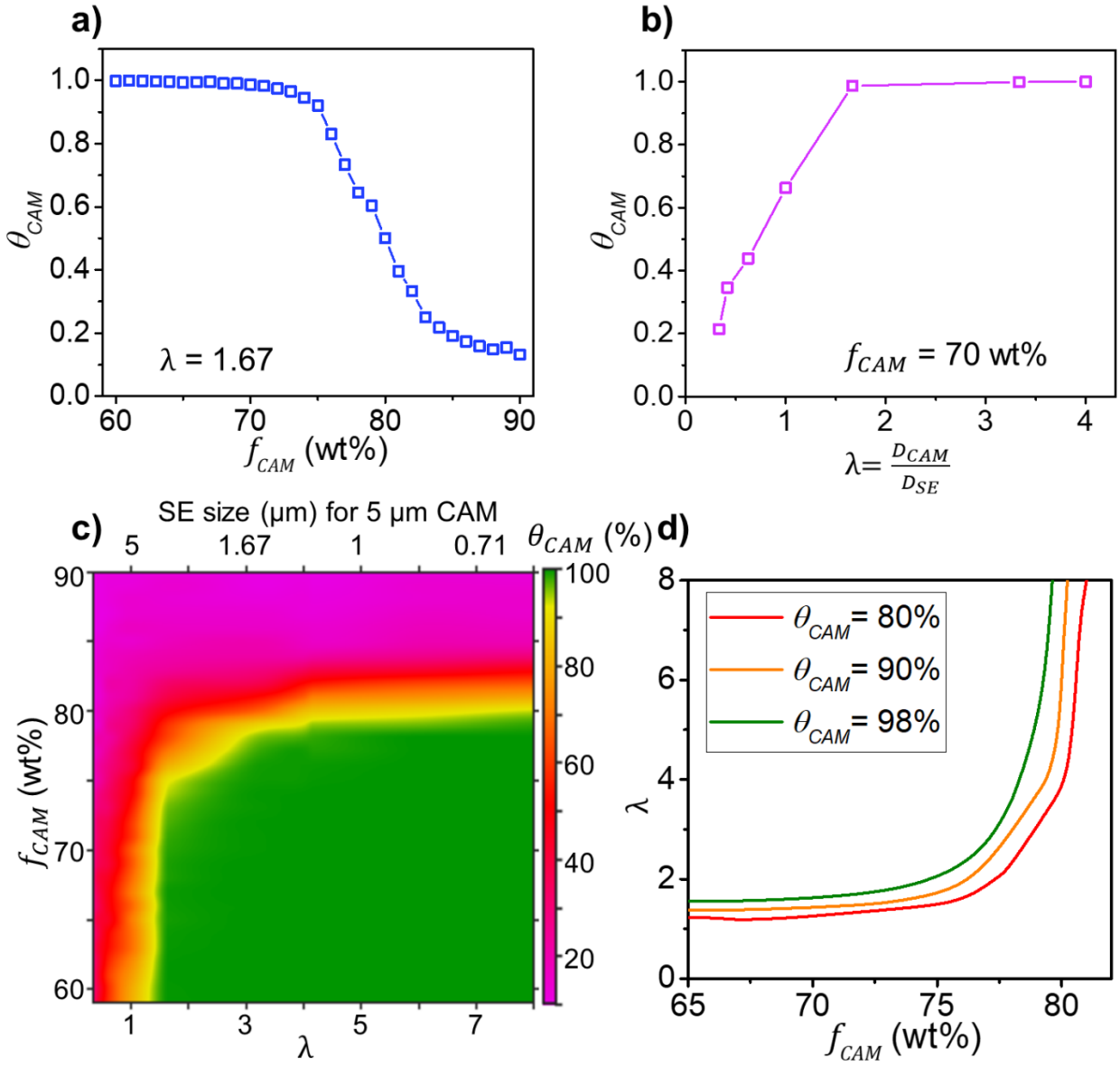

Figure 4.4. Modeling results. Modeling results showing the effect of **a)** f_{CAM} and **b)** λ on θ_{CAM}. **c)** θ_{CAM} as a function of both λ and f_{CAM}. d) Critical λ needed to achieve θ_{CAM} = 80%, 90%, and 98% as a function of f_{CAM}.

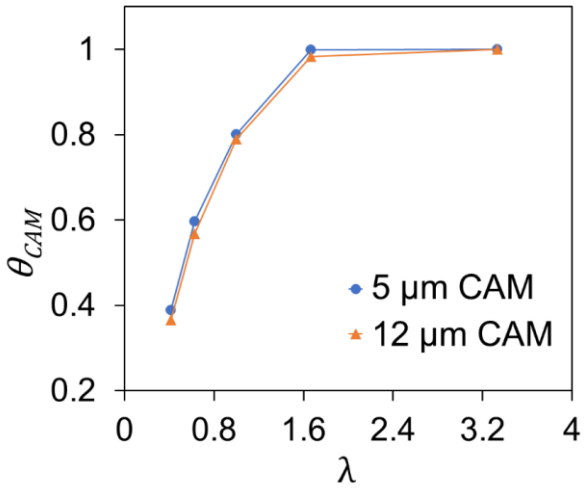

Figure 4.5. Active CAM ratio (θ_{CAM}) as a function of average particle size ratio of CAM to SE (λ). Two sets of data with different CAM sizes (5 and 12 μm) were calculated. The same results were obtained for the same λ, indicating that the utilization is controlled by λ rather than by the absolute particle sizes. The CAM loading was fixed at 60 wt%.

Visualization of Ionic Percolating Networks

Figure 4.6 presents visualizations of the composite cathodes and their percolating networks for various cathode weight fractions and LPS particle sizes, all with $\overline{D}_{CAM} = 5\ \mu m$.

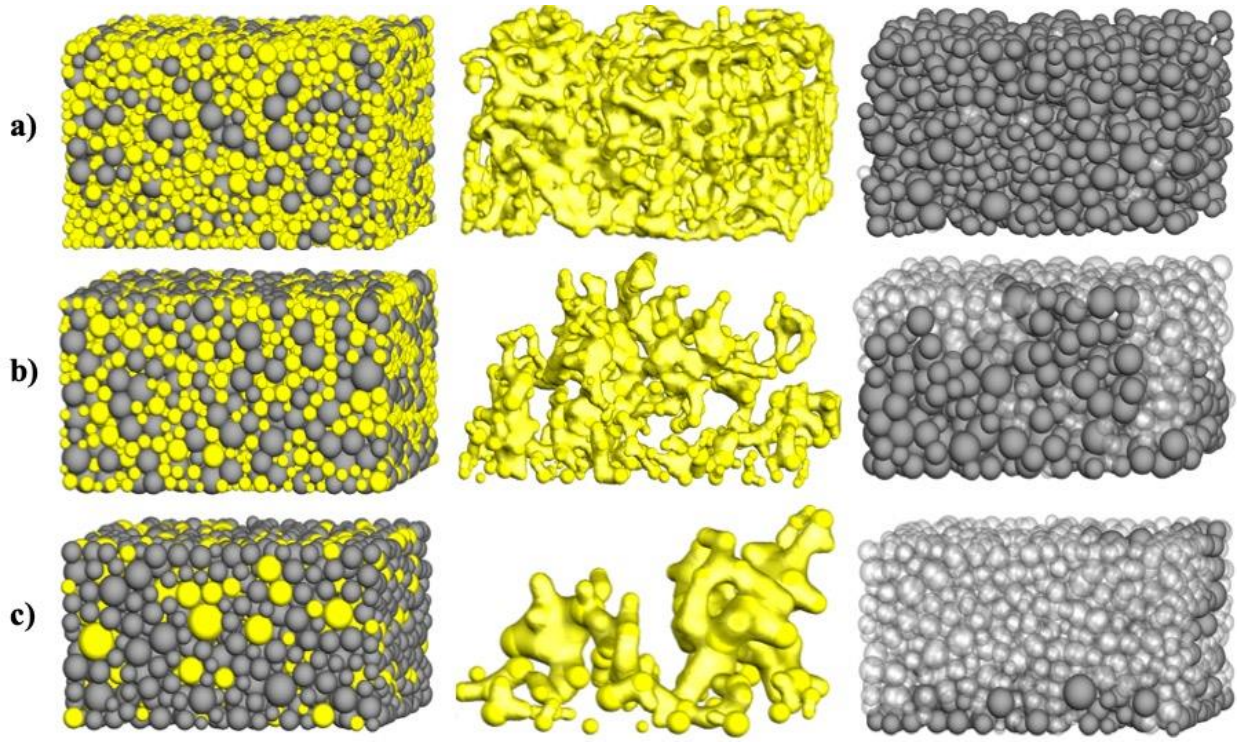

Figure 4.6. Visualization of models. **a)** $f_{CAM} = 70\ wt\%$, $\overline{D}_{SE} = 3\ \mu m$, **b)** $f_{CAM} = 80\ wt\%$, $\overline{D}_{SE} = 3\ \mu m$, and **c)** $f_{CAM} = 80\ wt\%$, $\overline{D}_{SE} = 5\ \mu m$, with CAM shown in gray and SE shown in yellow ($\overline{D}_{CAM} = 5\ \mu m$ for all three models). The composite microstructures, isolated SE percolating networks, and isolated CAM particles are shown in the left-hand, middle, and right-hand columns, respectively. The yellow surfaces in the middle column were generated using the QuickSurf method by Gaussian interpolating the SE positions weighted by their diameters.[200] The solid-gray and transparent-gray colors in the right-hand column represent the active and inactive CAM, respectively.

To demonstrate the SE particle size and cathode loading effect, we isolated the SE percolating network (middle panel) and highlighted the active/inactive CAM particles (right panel). Upon increasing f_{CAM} from 70 wt% (Figure 4.6**a**) to 80 wt% (Figure 4.6**b**) under constant λ ($\lambda = 1.67$), the SE volume decreases. Consequently, the SE percolating network becomes smaller and less spatially uniform, resulting in a decrease in θ_{CAM} from 98% to 52%.

Comparing Figure 4.6**b** and **c**, where f_{CAM} was fixed at 80 wt% while increasing the SE particle size (λ =1.67 and 1 for model **b** and **c**, respectively), it is apparent that the SE percolating network becomes smaller upon increasing the SE particle size. Therefore, most of the active CAM in model **c** is limited to the volume near the separator, leading to a low θ_{CAM} ($\theta_{CAM} = 52\%$ and 25% for model **b** and **c**, respectively).

Experimental Validation of the Effect of Particle Size Ratio and Cathode Loading on CAM Utilization

We performed a set of systematic experiments to test the dependence of the cathode utilization on particle size ratio and cathode loading as predicted by the model. Figure 4.7**a** presents the results for four cells using LPS of different sizes in the cathode composite. The cathode particle size and f_{CAM} were fixed at 5 μm and 60 wt% respectively. The cells with 8- and 5-μm LPS particles

delivered reduced discharge capacities (~75 and 125 mAh g^{-1}, respectively) compared with those for the 3- and 1.5-µm LPS particles (> 150 mAh g^{-1}) (Figure 4.7**a**), proving that the use of smaller SE particles (larger λ) indeed improves θ_{CAM}. The good agreement between the experimental and model-predicted specific capacities is shown in Figure 4.7**b**. The model-predicted specific capacities were calculated by multiplying the full capacity (largest experimental specific capacity observed, 155 mAh g^{-1}) by the predicted θ_{CAM} (shown in Figure 4.4**c**).

We also investigated the change in discharge capacity when λ was modified by only changing the CAM particle size, rather than the SE particle size as above. Figure 4.7**c** and **d** present the variation in discharge capacity when the NMC particle size is increased from 5 to 12 µm while fixing the LPS particle size at either 3 or 1.5 µm (f_{CAM} was fixed at 80 wt%). For both LPS sizes, the cells with 12-µm CAM particles (black curves) delivered larger discharge capacities than those with 5-µm CAM particles (red curves), further demonstrating that a larger λ benefits θ_{CAM}. The initial discharge capacities of the four cells are compared with the model-predicted specific capacities in Figure 4.7**e** and show good agreement.

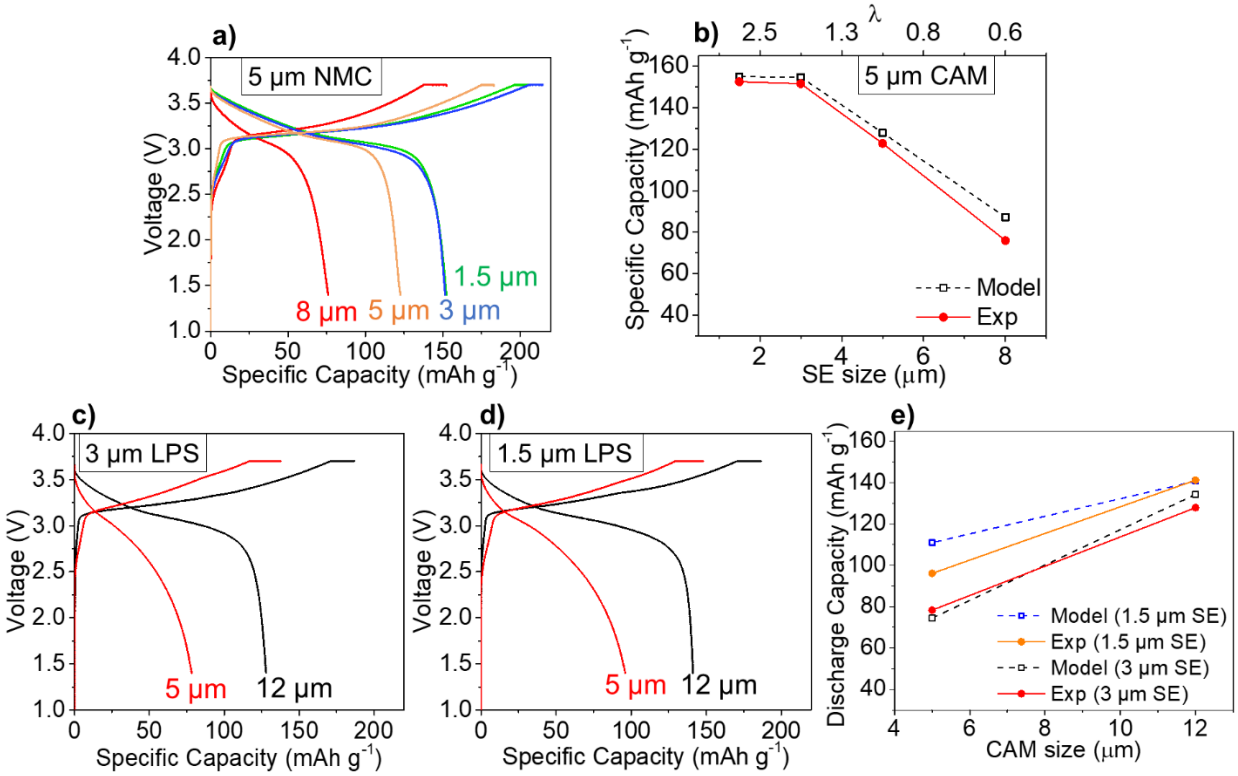

Figure 4.7. Full cell tests with different particle sizes. **a)** First-cycle voltage curves of SSBs using different-sized LPS particles in the cathode composite with fixed NMC size (5 µm) and f_{CAM} (60 wt%). **b)** Comparison of experimental capacities in **a** with model-predicted capacities. **c)** and **d)** First-cycle voltage curves of SSBs using different-sized NMC particles (5 and 12 µm) in the cathode composite with fixed LPS size (3 µm for **c** and 1.5 µm for **d**) and f_{CAM} (80 wt%). **e)** Comparison of experimental capacities in **c** and **d** with model-predicted capacities.

Finally, the effect of f_{CAM} was validated experimentally by varying f_{CAM} while fixing the LPS and NMC particle sizes. Cells with f_{CAM} = 60 wt%, 70 wt%, and 80 wt% were tested using 5-µm NMC and 3-µm LPS ($\lambda = 1.67$, Figure 4.8**a**) or 1.5-µm LPS ($\lambda = 3.33$, Figure 4.8**c**) particles. For f_{CAM} = 60 wt% (blue curves in Figure 4.8**a** and **c**), both LPS sizes fall in the high cathode utilization

area (the green region in Figure 4.4**c**). Consistent with this prediction, the experimental voltage curves for both cells are almost identical, with both specific discharge capacities greater than 150 mAh/g. In contrast, for f_{CAM} = 80 wt% (black curves in Figure 4.8**a** and **c**), both LPS sizes fall into the low-θ_{CAM} regions (purple and red regions in Figure 4.4**c**), consistent with the dramatically decreased initial discharge capacity. In addition, comparison of the discharge capacities for f_{CAM} = 70 wt% (orange curves in Figure 4.8**a** and **c**) confirms that increasing λ ensures higher θ_{CAM}. Because λ is larger for the cells with 1.5-μm LPS, f_{CAM} can be increased from 60 wt% to 70 wt% without any capacity decrease. The experimental data show good agreement with the model-predicted specific capacities (Figure 4.8**b** and **d**).

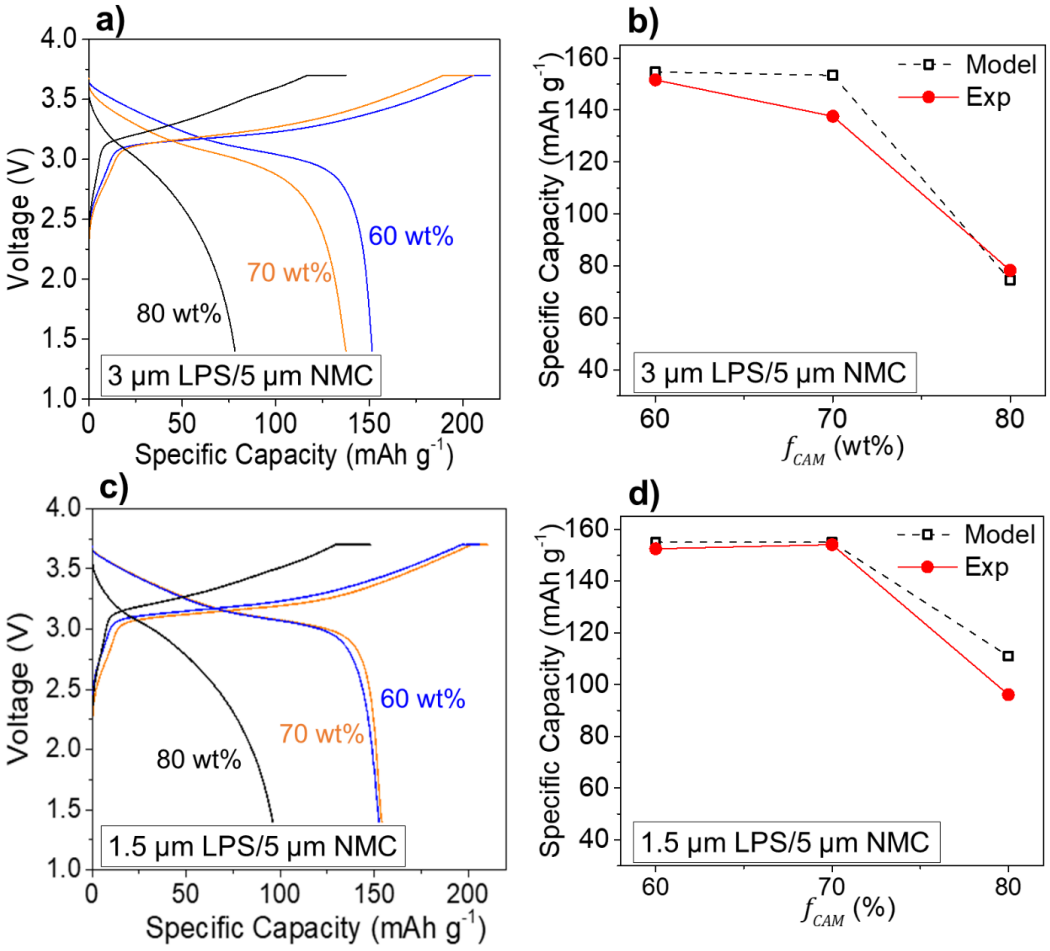

Figure 4.8. First-cycle voltage profiles of SSBs. **a)** 3-μm and **c)** 1.5-μm LPS in the cathode composite. The blue curves represent the cells with 60 wt% NMC, 35 wt% LPS, and 5 wt% CNF ($f_{CAM} = 60\ wt\%$), the orange curves represent the cells with 70 wt% NMC, 25 wt% LPS, and 5 wt% CNF ($f_{CAM} = 70\ wt\%$), and the black curves represent the cells with 80 wt% NMC, 15 wt% LPS, and 5 wt% CNF ($f_{CAM} = 80\ wt\%$). **b)** and **d)** Comparison of experimental first-cycle discharge capacities with model-predicted capacities. In all the cells, 5-μm NMC particles were used.

4.6 Discussion

Solid-state batteries are an important future energy storage technology which may surpass current Li-ion in both energy density and safety. But high energy density can only be achieved if cathode composites can be made with cathode volume fractions close to those in liquid ion cells. Our results show that degradation of capacity at high cathode loading is a percolation problem with only the volume of cathode near the separator being activated when the loading is too high. Somewhat surprisingly, both our modeling and experimental results indicate that percolation depends as much on the cathode volume fraction as on the ratio of the cathode to SE particle size (λ), and that even at high loading the cathode utilization can be dramatically improved by tuning this ratio. Our findings indicate that a larger λ is beneficial for improving cathode utilization and enables higher cathode loading. More specifically, at fixed cathode and SE volume, the battery capacity can be significantly improved when using SE and CAM particles so that $d_{SE} < d_{CAM}/\lambda$ is satisfied. The higher the weight fraction of cathode, the larger the value of λ is.

Experimentally, we demonstrated that both increasing the CAM particle size and reducing the SE particle size are effective ways to achieve a larger λ and therefore higher f_{CAM}. It may seem counterintuitive that a larger cathode particle size actually improves performance as larger particle sizes are associated with longer diffusion paths. But our result is consistent with Li-percolation to the CAM particles being the limiting factor. Larger cathode particles have higher surface area and therefore a higher probability to contact a percolating SE network. This finding shows that experience from liquid Li-ion cells cannot always be translated directly to solid-state batteries.

As shown in Figure 4.7**d**, $f_{CAM} = 80$ wt% can be achieved in the cathode composite with near full active material utilization when λ is increased to ~8. To put this finding into perspective, we calculate the active material volume ratio in the cathode composite as function of cathode loading using previously reported densities and composite cathode porosities (Figure 4.9**a**).[74] For $f_{CAM} = 80$ wt%, the volume loading is ~50 vol%, comparable to that of a common liquid cell cathode (usually >45 vol%).[187,188]

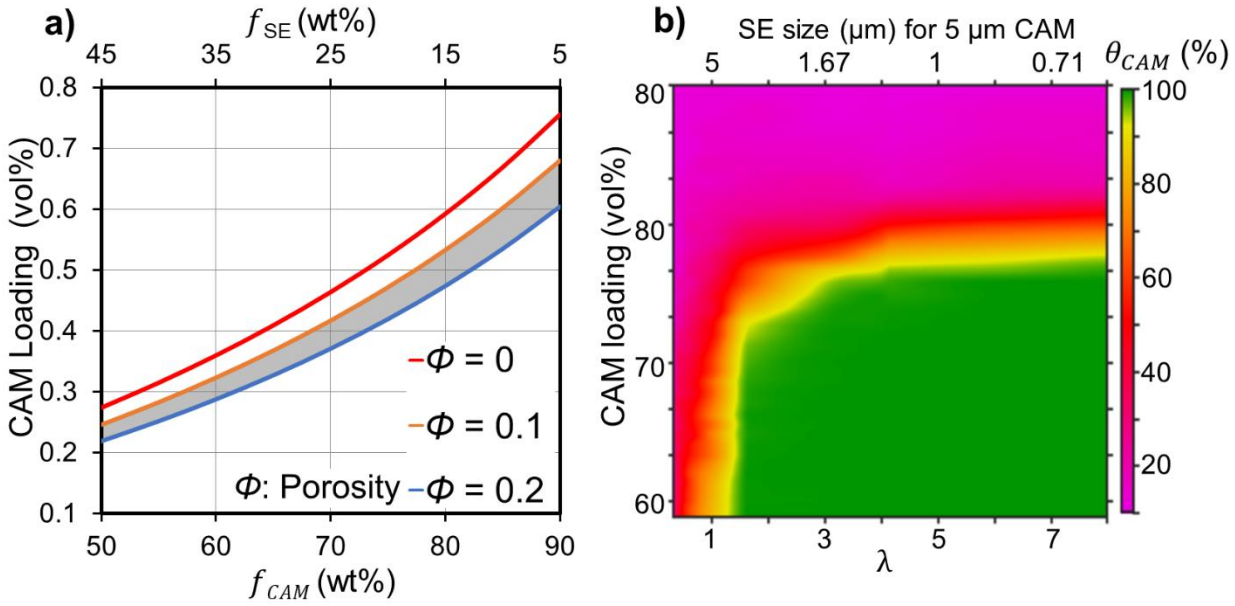

Figure 4.9. Generalization of the results. **a)** CAM volume loading in cathode composite as a function of f_{CAM}. The shaded area represents the experimentally reported porosities for SSB cathode composites (between 0.1 and 0.2).[74] **b)** θ_{CAM} as a function of both λ and CAM volume loading.

According to our modeling results, higher than 80 wt% CAM loading is possible if λ is further increased. Such large λ will likely require the SE particle size to be reduced to the sub-micron scale. Nano-sized SE particles have been successfully synthesized using solution-based methods in several recent studies, which could potentially lead to even higher CAM loading in the cathode composite.[82,83] Our findings thus motivate further research on the synthesis and application of nano-sized SEs with high ionic conductivity.

It should be noted that although a very large λ can enable high cathode loading and therefore high energy density of a solid-state battery, very large cathode particles or very small SE particles may limit the power density of the cell. A very large CAM particle requires more time to lithiate and delithiate.[197] Reduction of the SE particle size brings other potential issues as a smaller percolation channel width and an increased number of particle/grain boundaries may increase impedance within the SE network.[201] Hence, whether λ is reduced by increasing the cathode particle size or by reducing the SE size should depend on the relative importance of these kinetic contributions. Solid-state batteries using cathode materials such as $LiCoO_2$ with good intrinsic Li mobility may be optimized by increasing the cathode particle size, whereas cathode materials with poorer Li-ion transport such as some NMCs may require SE particle size reduction to achieve high loading. Therefore, this trade-off between power and energy density should be considered when determining the optimal λ.

Further refinement of the effect of λ on the ionic diffusivity in the cathode composite would require additional details, such as the Li transport properties across particle boundaries and the contact area between particles. An accurate description of the contact area between particles requires modeling of the plastic deformation of LPS particles, which has been observed experimentally.[74] The degree of the deformation will largely determine the contact area between particles and therefore the resistance at particle boundaries.

In addition to the Li percolation path provided by the SE, the electron path provided by the conductive carbon additive is also crucial for determining CAM utilization. In current study, excess (5 wt%) CNF is used to ensure sufficient electron percolation. The electronic percolation can become critical when less or no conductive additive is added. A recent study has shown that without conductive carbon additive, the electron percolation must be provided through CAM only, and becomes the limiting factor in cathode utilization.[81] This led to a conclusion that a smaller CAM particle size provides better cathode utilization, which seemingly contradicts with our results. However, since the electron percolation provided by the CAM particles is the limiting factor in this case, decreasing the CAM particle size improves the electronic percolation and the cathode utilization according to our model. This further highlights the importance of electronic transport in cathode composite and also demonstrates that our model applies to both electronic and ionic percolations. Adding carbon particles in the model would allow both the Li-ion and electron transport in the cathode composite to be modeled as well as optimization of both the carbon and SE ratio in the cathode composite. However, the particle sizes of commonly used carbon conductors (e.g., carbon blacks such as Super P and Super C65) are extremely small (tens of nanometers) and would increase the number of particles in our model to the order of 10^{10}, exceeding any computational ability. However, recent findings that the SE degrades at the interface with carbon[202,203] is leading to the preferred use of other morphologies for the additive, such as carbon nanofibers whose high aspect ratio leads to better percolation at lower volume fraction.

Finally, we note that percolation is controlled by the material volume distribution within the composite. Hence, our results can be generalized to other active materials and conductors by converting the data from wt% to vol%. An example of this is shown in Figure 4.9**b**. We believe very similar particle size effects will be observed when utilizing other types of SEs, such as $Li_7La_3Zr_2O_{12}$ garnet oxide, since the additional sintering step used in oxide SE processing does not dramatically change the SE percolation network morphology. Additionally, our results should be applicable to SSB anode composites when using traditional anode active materials such as mesocarbon microbeads or $Li_4Ti_5O_{12}$.

4.7 Conclusion

We have demonstrated the effect of the cathode to SE particle size ratio (λ) on the cathode utilization and loading tolerance in cold-pressed SSBs. Both our modeling and experimental results indicate that cathode utilization in solid state composites is percolation controlled, and that a larger ratio of cathode to conductor particle size enables higher cathode loading. In the regime of high cathode volume loading, which is most relevant for creating higher energy density solid-state batteries, the cathode utilization is most critically dependent on this particle size ratio. This leads to the counterintuitive result that in some cases a higher cathode particle size can dramatically improve the capacity of the solid-state battery. We demonstrated the possibility of preparing a solid-state cathode composite with liquid-cell-level cathode volume loading (~50 vol%) by using large cathode particles (~12 μm) and small SE particles (~1.5 μm). Our study provides a quantitative guide for particle size optimization in SSB electrodes, and shows how such optimization can enable commercially relevant cathode loading in SSBs.

4.8 Acknowledgments

This work was supported by the Samsung Advanced Institute of Technology. The SEM analysis was performed at the Molecular Foundry, Lawrence Berkeley National Laboratory, supported by the Office of Science, Office of Basic Energy Sciences, of the U.S. Department of Energy under Contract No. DE-AC02-05CH11231. This research used the Lawrencium computational cluster resource provided by the IT Division at Lawrence Berkeley National Laboratory (supported by the Director, Office of Science, Office of Basic Energy Sciences, of the U.S. Department of Energy under Contract No. DE-AC02-05CH11231) and the Savio computational cluster resource provided by the Berkeley Research Computing program at the University of California, Berkeley (supported by the UC Berkeley Chancellor, Vice Chancellor for Research, and Chief Information Officer). The authors also gratefully acknowledge Dr. Taku Watanabe, Dr. Yuichi Aihara, Dr. Tomoyuki Tsujimura and the Samsung R&D Institute of Japan for providing the LZO-coated cathode materials.

Chapter 5 - Summary and conclusion

The concept of an all-solid-state battery (SSB) shows great potential as the next-generation energy storage technology. With the emergence of various high conductivity solid electrolytes (SEs), integrating them into full cells has become the next major challenge for SSBs. In particular, significant improvements of full cell energy density and cycle life are needed for SSBs to compete with current Li-ion batteries. The purpose of this work is to investigate the various degradation mechanisms in the SSBs and improve the full cell energy density through the optimization of the composite electrode microstructure.

In the first part of the dissertation, the chemical stability between sulfide SEs and oxide cathode materials were studied. A methodology was presented that combines computational and experimental tools to investigate the chemical reactivity between SEs and electrodes. XRD, TGA, and DSC were proven to be very effective experimental techniques to explore the interfacial reactions between electrolytes and electrodes. By applying this method to the Na solid-state system, the voltage windows of the sulfide electrolytes were determined to be very small (1.8–2.5 V). The thermodynamics and kinetics behind the reactions between incompatible electrolyte/electrode pairs were also explored, and the most stable components ($NaCrO_2$/Na_3PS_4/Na–Sn) within the studied chemical space was recommended. This study demonstrates the highly reactive nature of sulfide SEs and highlights the importance of cathode coating for improving the chemical stability in SSBs.

Next, the mechanical degradation in SSBs was investigated. Using FIB-SEM tomography, SSB composite cathode morphology before and after long-term cycling was imaged, revealing the severe mechanical degradation during cycling. A large amount of void volume (~ 12%) and contact loss area (> 10%) are found in the cathode composite after 50 cycles. The observed rapid capacity drop in later cycles is likely related to this contact loss between cathode and SE. These results also suggest that mechanical degradation does not progress gradually starting from the first cycle. Instead, the majority of the void formation and contact loss likely occurs at later cycles and over a short period of time.

Finally, a method to improve the full cell energy density by increasing the cathode loading is proposed. Combined experimental and computational results show the effect of the cathode to SE particle size ratio on the cathode utilization and loading tolerance in cold-pressed SSBs. A larger ratio of the cathode to conductor particle size is shown to enable a higher cathode loading. While a smaller SE particle size can increase the cathode loading, a larger cathode particle size can also achieve a similar result. A solid-state cathode composite with liquid-cell-level cathode volume loading (~50 vol%) was achieved by using large cathode particles (~12 μm) and small SE particles (~1.5 μm). This particle size optimization proves that commercially relevant cathode loading in SSBs can be achieved by the simple cold-pressing method.

The results presented in this dissertation show the many challenges for SSB full cell design. Factors such as chemical compatibility, mechanical stability, and composite microstructures can all influence the energy density and cycle life of a SSB. This work provides a better understanding of the various effects of these factors and will help the future engineering of a better SSB.

Bibliography

(1) Global EV Outlook 2019. Available at: https://webstore.iea.org/global-ev-outlook-2019. (Accessed: Oct 11, 2019)

(2) Cano, Z. P., Banham, D., Ye, S., Hintennach, A., Lu, J., Fowler, M.; Chen, Z. Batteries and fuel cells for emerging electric vehicle markets. *Nature Energy* **2018,** *3*, 279.

(3) Kwade, A., Haselrieder, W., Leithoff, R., Modlinger, A., Dietrich, F.; Droeder, K. Current status and challenges for automotive battery production technologies. *Nature Energy* **2018,** *3*, 290.

(4) Liu, J., Bao, Z., Cui, Y., Dufek, E. J., Goodenough, J. B., Khalifah, P., Li, Q., Liaw, B. Y., Liu, P., Manthiram, A., Meng, Y. S., Subramanian, V. R., Toney, M. F., Viswanathan, V. V., Whittingham, M. S., Xiao, J., Xu, W., Yang, J., Yang, X. Q.; Zhang, J. G. Pathways for practical high-energy long-cycling lithium metal batteries. *Nature Energy* **2019,** *4*, 180.

(5) LIU, L., CHEN, L., HUANG, X., YANG, X., YOON, W., LEE, H.; MCBREEN, J. ELECTROCHEMICAL AND IN SITU SYNCHROTRON XRD STUDIES ON AL2O3-COATED LICOO2 CATHODE MATERIAL. *APPL. GEOCHEM* **2004,** *20*, A1344.

(6) Jan N. Reimers; J. R. Dahn Electrochemical and In Situ X-Ray Diffraction Studies of Lithium Intercalation in LixCo02. *J. Electrochem. Soc.* **1992,** *139*, 2091.

(7) Arunkumar, T. A., Wu, Y.; Manthiram, A. Factors Influencing the Irreversible Oxygen Loss and Reversible Capacity in Layered Li[Li1/3Mn2/ 3]O2−Li[M]O2 (M = Mn0.5- y Ni0.5- y Co2 y and Ni1- y Co y) Solid Solutions. *Chemistry of Materials* **2007,** *19*, 3067.

(8) Armstrong, A. R., Holzapfel, M., Novák, P., Johnson, C. S., Kang, S., Thackeray, M. M.; Bruce, P. G. Demonstrating Oxygen Loss and Associated Structural Reorganization in the Lithium Battery Cathode Li[Ni0.2Li0.2Mn0.6]O2. *Journal of the American Chemical Society* **2006,** *128*, 8694.

(9) Xu, B., Qian, D., Wang, Z.; Meng, Y. S. Recent progress in cathode materials research for advanced lithium ion batteries. *Materials Science and Engineering: R: Reports* **2012,** *73*, 51.

(10) Olivetti, E. A., Ceder, G., Gaustad, G. G.; Fu, X. Lithium-Ion Battery Supply Chain Considerations: Analysis of Potential Bottlenecks in Critical Metals. *Joule* **2017,** *1*, 229.

(11) Etacheri, V., Marom, R., Elazari, R., Salitra, G.; Aurbach, D. Challenges in the development of advanced Li-ion batteries: a review. *Energy & Environmental Science* **2011,** *4*, 3243.

(12) Islam, M. S.; Fisher, C. A. J. Lithium and sodium battery cathode materials: computational insights into voltage, diffusion and nanostructural properties. *Chemical Society reviews* **2013,** *43*, 185.

(13) Croguennec, L.; Palacin, M. R. Recent Achievements on Inorganic Electrode Materials for Lithium-Ion Batteries. *Journal of the American Chemical Society* **2015,** *137,* 3140.

(14) Yoshio, M., Wang, H., Fukuda, K., Umeno, T., Abe, T.; Ogumi, Z. Improvement of natural graphite as a lithium-ion battery anode material, from raw flake to carbon-coated sphere. *Journal of Materials Chemistry* **2004,** *14,* 1754.

(15) Yoshio, M., Brodd, R. J.; Kozawa, A. *Lithium-Ion Batteries*; SPRINGER: New York, 2009.

(16) Zuo, X., Zhu, J., Müller-Buschbaum, P.; Cheng, Y. Silicon based lithium-ion battery anodes: A chronicle perspective review. *Nano Energy* **2017,** *31,* 113.

(17) Ayala, J., Yushin, G., Hertzberg, B., Magasinski, A., Dixon, P.; Kvit, A. High-performance lithium-ion anodes using a hierarchical bottom-up approach. *Nature Materials* **2010,** *9,* 353.

(18) Zhang, R., Du, Y., Li, D., Shen, D., Yang, J., Guo, Z., Liu, H. K., Elzatahry, A. A.; Zhao, D. Highly reversible and large lithium storage in mesoporous si/c nanocomposite anodes with silicon nanoparticles embedded in a carbon framework. *Adv. Mater. Weinheim* **2014,** *26,* 6749.

(19) XGS presents new silicon-graphene anode materials for lithium-ion batteries. Available at: https://phys.org/news/2013-04-xgs-silicon-graphene-anode-materials-lithium-ion.html. (Accessed: Oct 17, 2019)

(20) Nexeon Technology. Available at: https://www.nexeon.co.uk/technology/. (Accessed: Oct 17, 2019)

(21) Amperius Technology. Available at: https://www.amprius.com/technology/. (Accessed: Oct 17, 2019)

(22) Aurbach, D., Talyosef, Y., Markovsky, B., Markevich, E., Zinigrad, E., Asraf, L., Gnanaraj, J. S.; Kim, H. Design of electrolyte solutions for Li and Li-ion batteries: a review. *Electrochimica Acta* **2004,** *50,* 247.

(23) Wang, Q., Ping, P., Zhao, X., Chu, G., Sun, J.; Chen, C. Thermal runaway caused fire and explosion of lithium ion battery. *Journal of Power Sources* **2012,** *208,* 210.

(24) Aurbach, D., Gamolsky, K., Markovsky, B., Salitra, G., Gofer, Y., Heider, U., Oesten, R.; Schmidt, M. Study of surface phenomena related to electrochemical lithium intercalation into LixMOy host materials (M = Ni, Mn). *Journal of the Electrochemical Society* **2000,** *147,* 1322.

(25) Moshkovich, M., Gofer, Y.; Aurbach, D. Investigation of the Electrochemical Windows of Aprotic Alkali Metal (Li, Na, K) Salt Solutions. *J. Electrochem. Soc.* **2001,** *148,* E155.

(26) Fan, L., Wei, S., Li, S., Li, Q.; Lu, Y. Recent Progress of the Solid-State Electrolytes for High-Energy Metal-Based Batteries. *Advanced Energy Materials* **2018,** *8,* 1.

(27) "Solid Power, BMW partner to develop next-generation EV batteries." *Reuters* .**2017,** Available at: https://www.reuters.com/article/us-bmw-solid-power-idUSKBN1EC16V.(Accessed: Oct 19, 2019, 2019)

(28) "Hyundai Motor solely developing EV batteries." *The Korea Herald* .**2017,** Available at: http://www.koreaherald.com/view.php?ud=20170405000762.(Accessed: Oct 19, 2019, 2019)

(29) "Toyota set to sell long-range, fast-charging electric cars in 2022: paper." *Reuters* .**2017,** Available at: https://www.reuters.com/article/us-toyota-electric-cars-idUSKBN1AA035.(Accessed: Oct 19, 2019, 2019)

(30) Long, L., Wang, S., Xiao, M.; Meng, Y. Polymer electrolytes for lithium polymer batteries. *Journal of Materials Chemistry A* **2016,** *4*, 10038.

(31) Manuel Stephan, A.; Nahm, K. S. Review on composite polymer electrolytes for lithium batteries. *Polymer* **2006,** *47*, 5952.

(32) Janek, J.; Zeier, W. G. A solid future for battery development. *Nature Energy* **2016,** *1*, 16141.

(33) "Samsung must act fast to keep an exploding phone from blowing up its brand." *The Guardian* .**2016,** Available at: https://www.theguardian.com/technology/2016/oct/10/samsung-galaxy-note-7-exploding-phone-brand.(Accessed: Oct 19, 2019, 2019)

(34) "Tesla says single battery module caused car fire in Shanghai, has changed vehicle settings." *Reuters* .**2019,** Available at: https://www.reuters.com/article/us-tesla-china-safety-idUSKCN1TT154.(Accessed: Oct 19, 2019, 2019)

(35) Kato, Y., Hori, S., Saito, T., Suzuki, K., Hirayama, M., Mitsui, A., Yonemura, M., Iba, H.; Kanno, R. High-power all-solid-state batteries using sulfide superionic conductors. *Nature Energy* **2016,** *1*, 16030.

(36) Gambe, Y., Sun, Y.; Honma, I. Development of Bipolar All-solid-state Lithium Battery Based on Quasi-solid-state Electrolyte Containing Tetraglyme-LiTFSA Equimolar Complex. *Scientific reports* **2015,** *5*, 8869.

(37) Kamaya, N., Homma, K., Yamakawa, Y., Hirayama, M., Kanno, R., Yonemura, M., Kamiyama, T., Kato, Y., Hama, S., Kawamoto, K.; Mitsui, A. A lithium superionic conductor. *Nature Materials* **2011,** *10*, 682.

(38) Famprikis, T., Canepa, P., Dawson, J. A., Islam, M. S.; Masquelier, C. Fundamentals of inorganic solid-state electrolytes for batteries. *Nature materials* **2019,** 1.

(39) Wang, Y., Richards, W. D., Ong, S. P., Miara, L. J., Kim, J. C., Mo, Y.; Ceder, G. Design principles for solid-state lithium superionic conductors. *Nature Materials* **2015,** *14*, 1026.

(40) Deiseroth, H. J., Kong, S. T., Eckert, H., Vannahme, J., Reiner, C., Zaiß, T.; Schlosser, M. Li6PS5X: A class of crystalline Li-rich solids with an unusually high Li+ mobility. *Angewandte Chemie - International Edition* **2008,** *47,* 755.

(41) Sun, Y., Wang, Y., Liang, X., Xia, Y., Peng, L., Jia, H., Li, H., Bai, L., Feng, J., Jiang, H.; Xie, J. Rotational Cluster Anion Enabling Superionic Conductivity in Sodium-Rich Antiperovskite Na 3 OBH 4. *J. Am. Chem. Soc.* **2019,** *141,* 5644.

(42) Xu, M., Park, M. S., Lee, J. M., Kim, T. Y., Park, Y. S.; Ma, E. Mechanisms of Li + transport in garnet-type cubic Li 3 + x La 3 M 2 O 12 (M = Te, Nb, Zr). *Physical Review B* **2012,** *85,* 052301.

(43) Wang, Q., Wu, J., Lu, Z., Ciucci, F., Pang, W. K.; Guo, X. A New Lithium-Ion Conductor LiTaSiO5: Theoretical Prediction, Materials Synthesis, and Ionic Conductivity. *Advanced Functional Materials* **2019,** *29,* 1904232.

(44) Suzuki, N., Inaba, T.; Shiga, T. Electrochemical properties of LiPON films made from a mixed powder target of Li 3PO 4 and Li 2O. *Thin Solid Films* **2012,** *520,* 1821.

(45) Hayashi, A., Hama, S., Morimoto, H., Tatsumisago, M.; Minami, T. Preparation of Li2S-P2S5 Amorphous Solid Electrolytes by Mechanical Milling. *Journal of the American Ceramic Society* **2001,** *84,* 477.

(46) Boulineau, S., Courty, M., Tarascon, J.; Viallet, V. Mechanochemical synthesis of Li-argyrodite Li 6 PS 5 X (X= Cl, Br, I) as sulfur-based solid electrolytes for all solid state batteries application. *Solid State Ionics* **2012,** *221,* 1.

(47) Murugan, R., Thangadurai, V.; Weppner, W. Fast lithium ion conduction in garnet-type Li7La 3Zr2O12. *Angewandte Chemie - International Edition* **2007,** *46,* 7778.

(48) Arbi, K., Rojo, J. M.; Sanz, J. Lithium mobility in titanium based Nasicon Li1+xTi2−xAlx(PO4)3 and LiTi2−x Zrx(PO4)3 materials followed by NMR and impedance spectroscopy. *Journal of the European Ceramic Society* **2007,** *27,* 4215.

(49) Le, H. T. T., Kalubarme, R. S., Ngo, D. T., Jang, S., Jung, K., Shin, K.; Park, C. J. Citrate gel synthesis of aluminum-doped lithium lanthanum titanate solid electrolyte for application in organic-type lithium–oxygen batteries. *Journal of Power Sources* **2015,** *274,* 1188.

(50) Zhao, Y.; Daemen, L. L. Superionic conductivity in lithium-rich anti-perovskites. *Journal of the American Chemical Society* **2012,** *134,* 15042.

(51) Yubuchi, S., Teragawa, S., Aso, K., Tadanaga, K., Hayashi, A.; Tatsumisago, M. Preparation of high lithium-ion conducting Li6PS5Cl solid electrolyte from ethanol solution for all-solid-state lithium batteries. *J. Power Sources* **2015,** *293,* 941.

(52) Thangadurai, V., Kaack, H.; Weppner, W. J. F. Novel Fast Lithium Ion Conduction in Garnet-Type Li 5 La 3 M 2 O 12 (M Nb, Ta). *J Am Ceram Soc* **2003,** *86,* 437.

(53) Inaguma, Y., Liquan, C., Itoh, M., Nakamura, T., Uchida, T., Ikuta, H.; Wakihara, M. High ionic conductivity in lithium lanthanum titanate. *Solid State Commun.* **1993,** *86,* 689.

(54) Stramare, S., Thangadurai, V.; Weppner, W. Lithium Lanthanum Titanates: A Review. *Chemistry of Materials* **2003,** *15,* 3974.

(55) Sharafi, A., Meyer, H. M., Nanda, J., Wolfenstine, J.; Sakamoto, J. Characterizing the Li-Li7La3Zr2O12 interface stability and kinetics as a function of temperature and current density. *Journal of Power Sources* **2016,** *302,* 135.

(56) Cheng, E. J., Sharafi, A.; Sakamoto, J. Intergranular Li metal propagation through polycrystalline Li6.25Al0.25La3Zr2O12 ceramic electrolyte. *Electrochim. Acta* **2017,** *223,* 85.

(57) Wang, M. J., Choudhury, R.; Sakamoto, J. Characterizing the Li-Solid-Electrolyte Interface Dynamics as a Function of Stack Pressure and Current Density. *Joule* **2019,** *3,* 2165.

(58) Hayashi, A., Noi, K., Sakuda, A.; Tatsumisago, M. Superionic glass-ceramic electrolytes for room-temperature rechargeable sodium batteries. *Nature Communications* **2012,** *3,* 856.

(59) Ohta, S., Kobayashi, T.; Asaoka, T. High lithium ionic conductivity in the garnet-type oxide Li7-X La3(Zr2-X, NbX)O12 (X = 0-2). *Journal of Power Sources* **2011,** *196,* 3342.

(60) Han, F., Zhu, Y., He, X., Mo, Y.; Wang, C. Electrochemical Stability of Li 10 GeP 2 S 12 and Li 7 La 3 Zr 2 O 12 Solid Electrolytes. *Advanced Energy Materials* **2016,** *6,* 1501590.

(61) Tian, Y., Shi, T., Richards, W. D., Li, J., Kim, J. C., Bo, S. H.; Ceder, G. Compatibility issues between electrodes and electrolytes in solid-state batteries. *Energy and Environmental Science* **2017,** *10,* 1150.

(62) Richards, W. D., Miara, L. J., Wang, Y., Kim, J. C.; Ceder, G. Interface Stability in Solid-State Batteries. *Chemistry of Materials* **2016,** *28,* 266.

(63) Han, F., Gao, T., Zhu, Y., Gaskell, K. J.; Wang, C. A Battery Made from a Single Material. *Adv Mater* **2015,** *27,* 3473.

(64) Zhang, W., Weber, D. A., Weigand, H., Arlt, T., Manke, I., Schröder, D., Koerver, R., Leichtweiss, T., Hartmann, P., Zeier, W. G.; Janek, J. Interfacial Processes and Influence of Composite Cathode Microstructure Controlling the Performance of All-Solid-State Lithium Batteries. *ACS Applied Materials & Interfaces* **2017,** *9,* 17835.

(65) Lacivita, V., Wang, Y., Bo, S.; Ceder, G. Ab initio investigation of the stability of electrolyte/electrode interfaces in all-solid-state Na batteries. *Journal of Materials Chemistry A* **2019,** *7,* 8144.

(66) Sakuda, A., Hayashi, A.; Tatsumisago, M. Interfacial Observation between LiCoO 2 Electrode and Li 2 S−P 2 S 5 Solid Electrolytes of All-Solid-State Lithium Secondary Batteries Using Transmission Electron Microscopy †. *Chemistry of Materials* **2010,** *22,* 949.

(67) Takada, K., Ohta, N., Zhang, L., Xu, X., Hang, B. T., Ohnishi, T., Osada, M.; Sasaki, T. Interfacial phenomena in solid-state lithium battery with sulfide solid electrolyte. *Solid State Ionics* **2012,** *225,* 594.

(68) Ohta, N., Takada, K., Zhang, L., Ma, R., Osada, M.; Sasaki, T. Enhancement of the high-rate capability of solid-state lithium batteries by nanoscale interfacial modification. *Advanced Materials* **2006,** *18,* 2226.

(69) Jung, S. H., Oh, K., Nam, Y. J., Oh, D. Y., Brüner, P., Kang, K.; Jung, Y. S. Li3BO3–Li2CO3: Rationally Designed Buffering Phase for Sulfide All-Solid-State Li-Ion Batteries. *Chemistry of Materials* **2018,** *30,* 8190.

(70) Ito, S., Fujiki, S., Yamada, T., Aihara, Y., Park, Y., Kim, T. Y., Baek, S., Lee, J., Doo, S.; Machida, N. A rocking chair type all-solid-state lithium ion battery adopting Li2O–ZrO2 coated LiNi0.8Co0.15Al0.05O2 and a sulfide based electrolyte. *J. Power Sources* **2014,** *248,* 943.

(71) Xiao, Y., Miara, L. J., Wang, Y.; Ceder, G. Computational Screening of Cathode Coatings for Solid-State Batteries. *Joule* **2019,** *3,* 1252.

(72) McGrogan, F. P., Swamy, T., Bishop, S. R., Eggleton, E., Porz, L., Chen, X., Chiang, Y.; Van Vliet, K. J. Compliant Yet Brittle Mechanical Behavior of Li $_2$ S-P $_2$ S $_5$ Lithium-Ion-Conducting Solid Electrolyte. *Advanced Energy Materials* **2017,** *7,* 1602011.

(73) SAKUDA, A., HAYASHI, A., TAKIGAWA, Y., HIGASHI, K.; TATSUMISAGO, M. Evaluation of elastic modulus of Li2S–P2S5 glassy solid electrolyte by ultrasonic sound velocity measurement and compression test. *Journal of the Ceramic Society of Japan* **2013,** *121,* 946.

(74) Choi, S., Jeon, M., Ahn, J., Jung, W. D., Choi, S. M., Kim, J. S., Lim, J., Jang, Y. J., Jung, H. G., Lee, J. H., Sang, B. I.; Kim, H. Quantitative Analysis of Microstructures and Reaction Interfaces on Composite Cathodes in All-Solid-State Batteries Using a Three-Dimensional Reconstruction Technique. *ACS Applied Materials and Interfaces* **2018,** *10,* 23740.

(75) Ni, J. E., Case, E. D., Sakamoto, J. S., Rangasamy, E.; Wolfenstine, J. B. Room temperature elastic moduli and Vickers hardness of hot-pressed LLZO cubic garnet. *Journal of Materials Science* **2012,** *47,* 7978.

(76) Wakasugi, J., Munakata, H.; Kanamura, K. Thermal Stability of Various Cathode Materials against Li 6.25 Al 0.25 La 3 Zr 2 O 12 Electrolyte. *Electrochemistry* **2017,** *85,* 77.

(77) Miara, L., Windmüller, A., Tsai, C. L., Richards, W. D., Ma, Q., Uhlenbruck, S., Guillon, O.; Ceder, G. About the Compatibility between High Voltage Spinel Cathode Materials and Solid

Oxide Electrolytes as a Function of Temperature. *ACS Applied Materials and Interfaces* **2016,** *8,* 26842.

(78) Weber, R., Fell, C. R., Dahn, J. R.; Hy, S. Operando X-ray Diffraction Study of Polycrystalline and Single-Crystal LixNi0.5Mn0.3Co0.2O2. *Journal of the Electrochemical Society* **2017,** *164,* A2992.

(79) Kondrakov, A. O., Schmidt, A., Xu, J., Geßwein, H., Mönig, R., Hartmann, P., Sommer, H., Brezesinski, T.; Janek, J. Anisotropic Lattice Strain and Mechanical Degradation of High- and Low-Nickel NCM Cathode Materials for Li-Ion Batteries. *The Journal of Physical Chemistry C* **2017,** *121,* 3286.

(80) Inada, T., Kobayashi, T., Sonoyama, N., Yamada, A., Kondo, S., Nagao, M.; Kanno, R. All solid-state sheet battery using lithium inorganic solid electrolyte, thio-LISICON. *J. Power Sources* **2009,** *194,* 1085.

(81) Strauss, F., Bartsch, T., De Biasi, L., Kim, A. Y., Janek, J., Hartmann, P.; Brezesinski, T. Impact of Cathode Material Particle Size on the Capacity of Bulk-Type All-Solid-State Batteries. *ACS Energy Letters* **2018,** *3,* 992.

(82) Calpa, M., Rosero-Navarro, N., Miura, A.; Tadanaga, K. Electrochemical performance of bulk-type all-solid-state batteries using small-sized Li7P3S11 solid electrolyte prepared by liquid phase as the ionic conductor in the composite cathode. *Electrochim. Acta* **2019,** *296,* 473.

(83) Wan, H., Mwizerwa, J. P., Qi, X., Xu, X., Li, H., Zhang, Q., Cai, L., Hu, Y. S.; Yao, X. Nanoscaled Na3PS4 Solid Electrolyte for All-Solid-State FeS2/Na Batteries with Ultrahigh Initial Coulombic Efficiency of 95% and Excellent Cyclic Performances. *ACS Applied Materials and Interfaces* **2018,** *10,* 12300.

(84) Bielefeld, A., Weber, D. A.; Janek, J. Microstructural Modeling of Composite Cathodes for All-Solid-State Batteries. *Journal of Physical Chemistry C* **2019,** *123,* 1626.

(85) Lobe, S., Dellen, C., Finsterbusch, M., Gehrke, H. G., Sebold, D., Tsai, C. L., Uhlenbruck, S.; Guillon, O. Radio frequency magnetron sputtering of Li7La3Zr2O12 thin films for solid-state batteries. *J. Power Sources* **2016,** *307,* 684.

(86) Kalita, D. J., Lee, S. H., Lee, K. S., Ko, D. H.; Yoon, Y. S. Ionic conductivity properties of amorphous Li-La-Zr-O solid electrolyte for thin film batteries. *Solid State Ionics* **2012,** *229,* 14.

(87) Nong, J., Xu, H., Yu, Z., Zhu, G.; Yu, A. Properties and preparation of Li-La-Ti-Zr-O thin film electrolyte. *Mater Lett* **2015,** *154,* 167.

(88) Saccoccio, M., Yu, J., Lu, Z., Kwok, S. C. T., Wang, J., Yeung, K. K., Yuen, M. M. F.; Ciucci, F. Low temperature pulsed laser deposition of garnet Li6.4La3Zr1.4Ta0.6O12films as all solid-state lithium battery electrolytes. *J. Power Sources* **2017,** *365,* 43.

(89) Park, J. S., Cheng, L., Zorba, V., Mehta, A., Cabana, J., Chen, G., Doeff, M. M., Richardson, T. J., Park, J. H., Son, J. W.; Hong, W. S. Effects of crystallinity and impurities on the electrical conductivity of Li-La-Zr-O thin films. *Thin Solid Films* **2015,** *576,* 55.

(90) Ogawa, M., Kanda, R., Yoshida, K., Uemura, T.; Harada, K. High-capacity thin film lithium batteries with sulfide solid electrolytes. *J. Power Sources* **2012,** *205,* 487.

(91) Nisula, M., Shindo, Y., Koga, H.; Karppinen, M. Atomic Layer Deposition of Lithium Phosphorus Oxynitride. *Chemistry of Materials* **2015,** *27,* 6987.

(92) Kazyak, E., Chen, K. H., Wood, K. N., Davis, A. L., Thompson, T., Bielinski, A. R., Sanchez, A. J., Wang, X., Wang, C., Sakamoto, J.; Dasgupta, N. P. Atomic Layer Deposition of the Solid Electrolyte Garnet Li7La3Zr2O12. *Chemistry of Materials* **2017,** *29,* 3785.

(93) Perng, Y., Cho, J., Sun, S. Y., Membreno, D., Cirigliano, N., Dunn, B.; Chang, J. P. Synthesis of ion conducting Li x Al y Si z O thin films by atomic layer deposition. *J.Mater.Chem.A* **2014,** *2,* 9566.

(94) Yi, E., Wang, W., Kieffer, J.; Laine, R. M. Flame made nanoparticles permit processing of dense, flexible, Li + conducting ceramic electrolyte thin films of cubic-Li 7 La 3 Zr 2 O 12 (c-LLZO). *Journal of Materials Chemistry A* **2016,** *4,* 12947.

(95) Nam, Y. J., Cho, S. J., Oh, D. Y., Lim, J. M., Kim, S. Y., Song, J. H., Lee, Y. G., Lee, S. Y.; Jung, Y. S. Bendable and thin sulfide solid electrolyte film: A new electrolyte opportunity for free-standing and stackable high-energy all-solid-state lithium-ion batteries. *Nano Letters* **2015,** *15,* 3317.

(96) Hayashi, A., Ohtomo, T., Mizuno, F., Tadanaga, K.; Tatsumisago, M. All-solid-state Li/S batteries with highly conductive glass–ceramic electrolytes. *Electrochemistry Communications* **2003,** *5,* 701.

(97) Ohtomo, T., Hayashi, A., Tatsumisago, M., Tsuchida, Y., Hama, S.; Kawamoto, K. All-solid-state lithium secondary batteries using the 75Li2S·25P2S5 glass and the 70Li2S·30P2S5 glass–ceramic as solid electrolytes. *J. Power Sources* **2013,** *233,* 231.

(98) Xie, J., Imanishi, N., Zhang, T., Hirano, A., Takeda, Y.; Yamamoto, O. Li-ion transport in all-solid-state lithium batteries with LiCoO2 using NASICON-type glass ceramic electrolytes. *J. Power Sources* **2009,** *189,* 365.

(99) Nagao, M., Hayashi, A.; Tatsumisago, M. Sulfur–carbon composite electrode for all-solid-state Li/S battery with Li2S–P2S5 solid electrolyte. *Electrochim. Acta* **2011,** *56,* 6055.

(100) Burns, J. C., Kassam, A., Sinha, N. N., Downie, L. E., Solnickova, L., Way, B. M.; Dahn, J. R. Predicting and extending the lifetime of Li-ion batteries. *J. Electrochem. Soc.* **2013,** *160,* A1451.

(101) Li, J., Ma, C., Chi, M., Liang, C.; Dudney, N. J. Solid electrolyte: The key for high-voltage lithium batteries. *Advanced Energy Materials* **2015,** *5,* 1401408.

(102) Bo, S., Wang, Y.; Ceder, G. Structural and Na-ion conduction characteristics of Na3PSxSe4-x. *J. Mater. Chem. A* **2016,** *4,* 9044.

(103) Wang, H., Chen, Y., Hood, Z. D., Sahu, G., Pandian, A. S., Keum, J. K., An, K.; Liang, C. An Air-Stable Na3SbS4 Superionic Conductor Prepared by a Rapid and Economic Synthetic Procedure. *Angewandte Chemie International Edition* **2016,** *55,* 8551.

(104) Richards, W. D., Tsujimura, T., Miara, L. J., Wang, Y., Kim, J. C., Ong, S. P., Uechi, I., Suzuki, N.; Ceder, G. Design and synthesis of the superionic conductor Na 10 SnP 2 S 12. *Nature Communications* **2016,** *7,* 11009.

(105) Richards, W. D., Wang, Y., Miara, L. J., Kim, J. C.; Ceder, G. Design of Li 1+2x Zn 1−x PS 4 , a new lithium ion conductor. *Energy & Environmental Science* **2016,** *9,* 3272.

(106) Ong, S. P., Mo, Y., Richards, W. D., Miara, L., Lee, H. S.; Ceder, G. Phase stability, electrochemical stability and ionic conductivity of the Li 10±1 MP 2 X 12 (M= Ge, Si, Sn, Al or P, and X= O, S or Se) family of superionic conductors. *Energy & Environmental Science* **2013,** *6,* 148.

(107) Wolfenstine, J., Allen, J. L., Sumner, J.; Sakamoto, J. Electrical and mechanical properties of hot-pressed versus sintered LiTi 2 (PO 4) 3. *Solid State Ionics* **2009,** *180,* 961.

(108) Allen, J. L., Wolfenstine, J., Rangasamy, E.; Sakamoto, J. Effect of substitution (Ta, Al, Ga) on the conductivity of Li 7 La 3 Zr 2 O 12. *J. Power Sources* **2012,** *206,* 315.

(109) Miara, L. J., Richards, W. D., Wang, Y. E.; Ceder, G. First-principles studies on cation dopants and electrolyte| cathode interphases for lithium garnets. *Chemistry of Materials* **2015,** *27,* 4040.

(110) Brousse, T., Fragnaud, P., Marchand, R., Schleich, D. M., Bohnke, O.; West, K. All oxide solid-state lithium-ion cells. *J. Power Sources* **1997,** *68,* 412.

(111) Bron, P., Johansson, S., Zick, K., Der Günne, Jörn Schmedt Auf, Dehnen, S.; Roling, B. Li10SnP2S12: An affordable lithium superionic conductor. *Journal of the American Chemical Society* **2013,** *135,* 15694.

(112) Tatsumisago, M., Nagao, M.; Hayashi, A. Recent development of sulfide solid electrolytes and interfacial modification for all-solid-state rechargeable lithium batteries. *Journal of Asian Ceramic Societies* **2013,** *1,* 17.

(113) Hayashi, A., Noi, K., Tanibata, N., Nagao, M.; Tatsumisago, M. High sodium ion conductivity of glass-ceramic electrolytes with cubic Na3PS4. *Journal of Power Sources* **2014,** *258,* 420.

(114) Richards, W. D., Miara, L. J., Wang, Y., Kim, J. C.; Ceder, G. Interface stability in solid-state batteries. *Chemistry of Materials* **2015,** *28,* 266.

(115) Takada, K., Ohta, N., Zhang, L., Fukuda, K., Sakaguchi, I., Ma, R., Osada, M.; Sasaki, T. Interfacial modification for high-power solid-state lithium batteries. *Solid State Ionics* **2008,** *179,* 1333.

(116) Ohta, N., Takada, K., Sakaguchi, I., Zhang, L., Ma, R., Fukuda, K., Osada, M.; Sasaki, T. LiNbO3-coated LiCoO2 as cathode material for all solid-state lithium secondary batteries. *Electrochemistry Communications* **2007,** *9,* 1486.

(117) Bo, S., Wang, Y., Kim, J. C., Richards, W. D.; Ceder, G. Computational and experimental investigations of Na-ion conduction in cubic Na3PSe4. *Chemistry of Materials* **2015,** *28,* 252.

(118) Lalère, F., Leriche, J., Courty, M., Boulineau, S., Viallet, V., Masquelier, C.; Seznec, V. An all-solid state NASICON sodium battery operating at 200 C. *J. Power Sources* **2014,** *247,* 975.

(119) Zhang, L., Zhang, D., Yang, K., Yan, X., Wang, L., Mi, J., Xu, B.; Li, Y. Vacancy-Contained Tetragonal Na3SbS4 Superionic Conductor. *Advanced Science* **2016,** *3,* 1600089.

(120) Wenzel, S., Randau, S., Leichtweiß, T., Weber, D. A., Sann, J., Zeier, W. G.; Janek, J. Direct observation of the interfacial instability of the fast ionic conductor Li10GeP2S12 at the lithium metal anode. *Chemistry of Materials* **2016,** *28,* 2400.

(121) Wenzel, S., Leichtweiss, T., Krüger, D., Sann, J.; Janek, J. Interphase formation on lithium solid electrolytes—An in situ approach to study interfacial reactions by photoelectron spectroscopy. *Solid State Ionics* **2015,** *278,* 98.

(122) Komaba, S., Takei, C., Nakayama, T., Ogata, A.; Yabuuchi, N. Electrochemical intercalation activity of layered NaCrO2 vs. LiCrO2. *Electrochemistry Communications* **2010,** *12,* 355.

(123) Ma, X., Chen, H.; Ceder, G. Electrochemical properties of monoclinic NaMnO2. *Journal of The Electrochemical Society* **2011,** *158,* A1307.

(124) Yabuuchi, N., Yoshida, H.; Komaba, S. Crystal Structures and Electrode Performance of Alpha-$NaFeO_2$ for Rechargeable Sodium Batteries. *Electrochemistry* **2012,** *80,* 716.

(125) Berthelot, R., Carlier, D.; Delmas, C. Electrochemical investigation of the P2–NaxCoO2 phase diagram. *Nature Materials* **2011,** *10,* 74.

(126) Vassilaras, P., Ma, X., Li, X.; Ceder, G. Electrochemical properties of monoclinic NaNiO2. *Journal of The Electrochemical Society* **2013,** *160,* A207.

(127) Komaba, S., Matsuura, Y., Ishikawa, T., Yabuuchi, N., Murata, W.; Kuze, S. Redox reaction of Sn-polyacrylate electrodes in aprotic Na cell. *Electrochemistry Communications* **2012,** *21,* 65.

(128) Chevrier, V. L.; Ceder, G. Challenges for Na-ion negative electrodes. *J. Electrochem. Soc.* **2011,** *158,* A1011.

(129) Ong, S. P., Chevrier, V. L., Hautier, G., Jain, A., Moore, C., Kim, S., Ma, X.; Ceder, G. Voltage, stability and diffusion barrier differences between sodium-ion and lithium-ion intercalation materials. *Energy & Environmental Science* **2011,** *4,* 3680.

(130) Palomares, V., Serras, P., Villaluenga, I., Hueso, K. B., Carretero-González, J.; Rojo, T. Na-ion batteries, recent advances and present challenges to become low cost energy storage systems. *Energy & Environmental Science* **2012,** *5,* 5884.

(131) Wang, L. P., Yu, L., Wang, X., Srinivasan, M.; Xu, Z. J. Recent developments in electrode materials for sodium-ion batteries. *Journal of Materials Chemistry A* **2015,** *3,* 9353.

(132) Zhao, J., Zhao, L., Dimov, N., Okada, S.; Nishida, T. Electrochemical and thermal properties of α-NaFeO2 cathode for Na-Ion batteries. *J. Electrochem. Soc.* **2013,** *160,* A3077.

(133) Kanno, R.; Murayama, M. Lithium Ionic Conductor Thio-LISICON: The Li2 S GeS2 - P 2 S 5 System. *J. Electrochem. Soc.* **2001,** *148,*

(134) Zhu, Y., He, X.; Mo, Y. First principles study on electrochemical and chemical stability of solid electrolyte-electrode interfaces in all-solid-state Li-ion batteries. *J. Mater. Chem. A* **2016,** *4,* 3253.

(135) Mo, Y., Ong, S. P.; Ceder, G. First principles study of the Li10GeP2S12 lithium super ionic conductor material. *Chemistry of Materials* **2011,** *24,* 15.

(136) Moshtev, R., Manev, V., Nassalevska, A., Gushev, A.; Pistoia, G. Chemically desodiated thiochromites as cathode materials in secondary lithium cells. *J. Power Sources* **1989,** *26,* 285.

(137) Popov, A. I.; Geske, D. H. Studies on the chemistry of halogen and of polyhalides. XIII. Voltammetry of iodine species in acetonitrile. *J. Am. Chem. Soc.* **1958,** *80,* 1340.

(138) Zhang, L., Yang, K., Mi, J., Lu, L., Zhao, L., Wang, L., Li, Y.; Zeng, H. Na3PSe4: A Novel Chalcogenide Solid Electrolyte with High Ionic Conductivity. *Advanced Energy Materials* **2015,** *5,* 2.

(139) Abouimrane, A., Dambournet, D., Chapman, K. W., Chupas, P. J., Weng, W.; Amine, K. A new class of lithium and sodium rechargeable batteries based on selenium and selenium–sulfur as a positive electrode. *J. Am. Chem. Soc.* **2012,** *134,* 4505.

(140) Chen, Z., Qin, Y.; Amine, K. Redox shuttles for safer lithium-ion batteries. *Electrochim. Acta* **2009,** *54,* 5605.

(141) Wen, Z., Cao, J., Gu, Z., Xu, X., Zhang, F.; Lin, Z. Research on sodium sulfur battery for energy storage. *Solid State Ionics* **2008,** *179,* 1697.

(142) Wizansky, A. R., Rauch, P. E.; Disalvo, F. J. Powerful oxidizing agents for the oxidative deintercalation of lithium from transition-metal oxides. *Journal of Solid State Chemistry* **1989,** *81,* 203.

(143) Kim, J. C., Li, X., Moore, C. J., Bo, S., Khalifah, P. G., Grey, C. P.; Ceder, G. Analysis of Charged State Stability for Monoclinic LiMnBO3 Cathode. *Chemistry of Materials* **2014,** *26,* 4200.

(144) Kim, Y., Ha, K., Oh, S. M.; Lee, K. T. High-Capacity Anode Materials for Sodium-Ion Batteries. *Chemistry–A European Journal* **2014,** *20,* 11980.

(145) Wenzel, S., Leichtweiss, T., Weber, D. A., Sann, J., Zeier, W. G.; Janek, J. Interfacial reactivity benchmarking of the sodium ion conductors Na3PS4 and sodium β-alumina for protected sodium metal anodes and sodium all-solid-state batteries. *ACS Applied Materials & Interfaces* **2016,** *8,* 28216.

(146) Jain, A., Ong, S. P., Hautier, G., Chen, W., Richards, W. D., Dacek, S., Cholia, S., Gunter, D., Skinner, D.; Ceder, G. Commentary: The Materials Project: A materials genome approach to accelerating materials innovation. *Apl Materials* **2013,** *1,* 011002.

(147) Murayama, M., Kanno, R., Irie, M., Ito, S., Hata, T., Sonoyama, N.; Kawamoto, Y. Synthesis of new lithium ionic conductor thio-LISICON - Lithium silicon sulfides system. *Journal of Solid State Chemistry* **2002,** *168,* 140.

(148) Kanno, R., Hata, T., Kawamoto, Y.; Irie, M. Synthesis of a new lithium ionic conductor, thio-LISICON–lithium germanium sulfide system. *Solid State Ionics* **2000,** *130,* 97.

(149) Lindqvist, M., Lundqvist, D.; Westgren, A. The crystal structure of Co9S8 and of pentlandite (Ni, Fe) 9S8. *Kemisk Tidskrift* **1936,** *48,* 156.

(150) Geller, S. Refinement of the crystal structure of Co9S8. *Acta Crystallogr.* **1962,** *15,* 1195.

(151) Fleet, M. E. The crystal structure of heazlewoodite, and metallic bonds in sulfide minerals. *Am. Mineral.* **1977,** *62,* 341.

(152) Parise, J. B. Structure of hazelwoodite (Ni3S2). *Acta Crystallographica Section B: Structural Crystallography and Crystal Chemistry* **1980,** *36,* 1179.

(153) Schwöbel, A., Hausbrand, R.; Jaegermann, W. Interface reactions between LiPON and lithium studied by in-situ X-ray photoemission. *Solid State Ionics* **2015,** *273,* 51.

(154) Hartmann, P., Leichtweiss, T., Busche, M. R., Schneider, M., Reich, M., Sann, J., Adelhelm, P.; Janek, J. Degradation of NASICON-Type Materials in Contact with Lithium Metal: Formation of Mixed Conducting Interphases (MCI) on Solid Electrolytes. *The Journal of Physical Chemistry C* **2013,** *117,* 21064.

(155) Wang, Z., Lee, J. Z., Xin, H. L., Han, L., Grillon, N., Guy-Bouyssou, D., Bouyssou, E., Proust, M.; Meng, Y. S. Effects of cathode electrolyte interfacial (CEI) layer on long term cycling of all-solid-state thin-film batteries. *J. Power Sources* **2016,** *324,* 342.

(156) McDaniel, M., Xiong, S., Wang, H.; Chen, H. Novel Sodium Tin Sulfides As Electrolyte for Solid State Sodium Ion Batteries.**2016,**

(157) Sahu, G., Lin, Z., Li, J., Liu, Z., Dudney, N.; Liang, C. Air-stable, high-conduction solid electrolytes of arsenic-substituted Li 4 SnS 4. *Energy & Environmental Science* **2014,** *7,* 1053.

(158) Seo, I.; Martin, S. W. IONIC CONDUCTIVITY MEASUREMENTS OF SOLID STATE THIN FILM ELECTROLYTES BASED ON LITHIUM THIO-GERMANATE MATERIALS. *Preparation and characterization of lithium thio-germanate thin film electrolytes grown by RF sputtering for solid state Li-ion batteries* **2009,** 153.

(159) Sahu, G., Rangasamy, E., Li, J., Chen, Y., An, K., Dudney, N.; Liang, C. A high-conduction Ge substituted Li 3 AsS 4 solid electrolyte with exceptional low activation energy. *Journal of Materials Chemistry A* **2014,** *2,* 10396.

(160) Kitaura, H., Hayashi, A., Ohtomo, T., Hama, S.; Tatsumisago, M. Fabrication of electrode–electrolyte interfaces in all-solid-state rechargeable lithium batteries by using a supercooled liquid state of the glassy electrolytes. *Journal of Materials Chemistry* **2011,** *21,* 118.

(161) Ong, S. P., Richards, W. D., Jain, A., Hautier, G., Kocher, M., Cholia, S., Gunter, D., Chevrier, V. L., Persson, K. A.; Ceder, G. Python Materials Genomics (pymatgen): A robust, open-source python library for materials analysis. *Computational Materials Science* **2013,** *68,* 314.

(162) Belsky, A., Hellenbrandt, M., Karen, V. L.; Luksch, P. New developments in the Inorganic Crystal Structure Database (ICSD): accessibility in support of materials research and design. *Acta Crystallographica Section B: Structural Science* **2002,** *58,* 364.

(163) Hautier, G., Fischer, C., Ehrlacher, V., Jain, A.; Ceder, G. Data mined ionic substitutions for the discovery of new compounds. *Inorg. Chem.* **2010,** *50,* 656.

(164) Blöchl, P. E. Projector augmented-wave method. *Physical Review B* **1994,** *50,* 17953.

(165) Perdew, J. P., Burke, K.; Ernzerhof, M. Generalized gradient approximation made simple. *Phys. Rev. Lett.* **1996,** *77,* 3865.

(166) Kresse, G.; Furthmüller, J. Efficiency of ab-initio total energy calculations for metals and semiconductors using a plane-wave basis set. *Computational Materials Science* **1996,** *6,* 15.

(167) Chase, M. W. NIST—JANAF Thermochemical Tables (Journal of Physical and Chemical Reference Data Monograph No. 9). *American Institute of Physics* **1998,**

(168) Kubaschewski, O., Alcock, C. B.; Spencer, P. J. *Materials thermochemistry*; Pergamon press: 1993.

(169) Sangster, J.; Pelton, A. D. The Na-Se (sodium-selenium) system. *Journal of phase equilibria* **1997,** *18,* 185.

(170) Jain, A., Hautier, G., Ong, S. P., Moore, C. J., Fischer, C. C., Persson, K. A.; Ceder, G. Formation enthalpies by mixing GGA and GGA U calculations. *Physical Review B* **2011,** *84,* 045115.

(171) Anisimov, V. I., Zaanen, J.; Andersen, O. K. Band theory and Mott insulators: Hubbard U instead of Stoner I. *Physical Review B* **1991,** *44,* 943.

(172) Dudarev, S. L., Botton, G. A., Savrasov, S. Y., Humphreys, C. J.; Sutton, A. P. Electron-energy-loss spectra and the structural stability of nickel oxide: An LSDA U study. *Physical Review B* **1998,** *57,* 1505.

(173) Zhang, W., Richter, F. H., Culver, S. P., Leichtweiss, T., Lozano, J. G., Dietrich, C., Bruce, P. G., Zeier, W. G.; Janek, J. Degradation Mechanisms at the Li10GeP2S12/LiCoO2 Cathode Interface in an All-Solid-State Lithium-Ion Battery. *ACS Applied Materials & Interfaces* **2018,** *10,* 22226.

(174) Koerver, R., Walther, F., Aygün, I., Sann, J., Dietrich, C., Zeier, W. G.; Janek, J. Redox-active cathode interphases in solid-state batteries. *Journal of Materials Chemistry A* **2017,** *5,* 22750.

(175) Koerver, R., Aygün, I., Leichtweiß, T., Dietrich, C., Zhang, W., Binder, J. O., Hartmann, P., Zeier, W. G.; Janek, J. Capacity Fade in Solid-State Batteries: Interphase Formation and Chemomechanical Processes in Nickel-Rich Layered Oxide Cathodes and Lithium Thiophosphate Solid Electrolytes. *Chemistry of Materials* **2017,** *29,* 5574.

(176) Walther, F., Koerver, R., Fuchs, T., Ohno, S., Sann, J., Rohnke, M., Zeier, W. G.; Janek, J. Visualization of the Interfacial Decomposition of Composite Cathodes in Argyrodite-Based All-Solid-State Batteries Using Time-of-Flight Secondary-Ion Mass Spectrometry. *Chemistry of Materials* **2019,** *31,* 3745.

(177) Tian, H.; Qi, Y. Simulation of the Effect of Contact Area Loss in All-Solid-State Li-Ion Batteries. *J. Electrochem. Soc.* **2017,** *164,* E3512.

(178) Koerver, R., Zhang, W., De Biasi, L., Schweidler, S., Kondrakov, A. O., Kolling, S., Brezesinski, T., Hartmann, P., Zeier, W. G.; Janek, J. Chemo-mechanical expansion of lithium electrode materials-on the route to mechanically optimized all-solid-state batteries. *Energy and Environmental Science* **2018,** *11,* 2142.

(179) Liu, T., Zhang, Y., Chen, R., Zhao, S. X., Lin, Y., Nan, C. W.; Shen, Y. Non-successive degradation in bulk-type all-solid-state lithium battery with rigid interfacial contact. *Electrochemistry Communications* **2017,** *79,* 1.

(180) Shi, T., Tu, Q., Tian, Y., Xiao, Y., Miara, L. J., Kononova, O.; Ceder, G. High Active Material Loading in All-Solid-State Battery Electrode via Particle Size Optimization. *Advanced Energy Materials* **2020,** *10,* 1902881.

(181) Lee, J., Urban, A., Li, X., Su, D., Hautier, G.; Ceder, G. Unlocking the potential of cation-disordered oxides for rechargeable lithium batteries. *Science* **2014,** *343,* 519.

(182) Manthiram, A., Yu, X.; Wang, S. Lithium battery chemistries enabled by solid-state electrolytes. *Nature Reviews Materials* **2017,** *2,* 16103.

(183) Sakuda, A., Takeuchi, T.; Kobayashi, H. Electrode morphology in all-solid-state lithium secondary batteries consisting of LiNi1/3Co1/3Mn1/3O2 and Li2S-P2S5 solid electrolytes. *Solid State Ionics* **2016,** *285,* 112.

(184) Nam, Y. J., Oh, D. Y., Jung, S. H.; Jung, Y. S. Toward practical all-solid-state lithium-ion batteries with high energy density and safety: Comparative study for electrodes fabricated by dry- and slurry-mixing processes. *Journal of Power Sources* **2018,** *375,* 93.

(185) Sakuda, A., Kuratani, K., Yamamoto, M., Takahashi, M., Takeuchi, T.; Kobayashi, H. All-solid-state battery electrode sheets prepared by a slurry coating process. *J. Electrochem. Soc.* **2017,** *164,* A2474.

(186) Kato, Y., Shiotani, S., Morita, K., Suzuki, K., Hirayama, M.; Kanno, R. All-solid-state batteries with thick electrode configurations. *The journal of physical chemistry letters* **2018,** *9,* 607.

(187) Shearing, P. R., Brandon, N. P., Gelb, J., Bradley, R., Withers, P. J., Marquis, A. J., Cooper, S.; Harris, S. J. Multi length scale microstructural investigations of a commercially available Li-ion battery electrode. *J. Electrochem. Soc.* **2012,** *159,* A1023.

(188) Ebner, M., Geldmacher, F., Marone, F., Stampanoni, M.; Wood, V. X-ray tomography of porous, transition metal oxide based lithium ion battery electrodes. *Advanced Energy Materials* **2013,** *3,* 845.

(189) Chung, D., Shearing, P. R., Brandon, N. P., Harris, S. J.; García, R. E. Particle size polydispersity in Li-ion batteries. *J. Electrochem. Soc.* **2014,** *161,* A422.

(190) Kloss, C., Goniva, C., Hager, A., Amberger, S.; Pirker, S. Models, algorithms and validation for opensource DEM and CFD–DEM. *Progress in Computational Fluid Dynamics, an International Journal* **2012,** *12,* 140.

(191) Di Renzo, A.; Di Maio, F. P. An improved integral non-linear model for the contact of particles in distinct element simulations. *Chemical engineering science* **2005,** *60,* 1303.

(192) Schöpfer, M. P., Abe, S., Childs, C.; Walsh, J. J. The impact of porosity and crack density on the elasticity, strength and friction of cohesive granular materials: insights from DEM modelling. *Int. J. Rock Mech. Min. Sci.* **2009,** *46,* 250.

(193) Silbert, L. E., Ertaş, D., Grest, G. S., Halsey, T. C., Levine, D.; Plimpton, S. J. Granular flow down an inclined plane: Bagnold scaling and rheology. *Physical Review E* **2001,** *64,* 051302.

(194) Zhang, H. P.; Makse, H. A. Jamming transition in emulsions and granular materials. *Physical Review E* **2005,** *72,* 011301.

(195) de Vasconcelos, L. S., Xu, R., Li, J.; Zhao, K. Grid indentation analysis of mechanical properties of composite electrodes in Li-ion batteries. *Extreme Mechanics Letters* **2016,** *9,* 495.

(196) Villars, P. PAULING FILE in: Inorganic Solid Phases, SpringerMaterials.**2012,**

(197) Park, M., Zhang, X., Chung, M., Less, G. B.; Sastry, A. M. A review of conduction phenomena in Li-ion batteries. *J. Power Sources* **2010,** *195,* 7904.

(198) Lagadec, M. F., Zahn, R., Müller, S.; Wood, V. Topological and network analysis of lithium ion battery components: the importance of pore space connectivity for cell operation. *Energy & Environmental Science* **2018,** *11,* 3194.

(199) Zeng, W.; Church, R. L. Finding shortest paths on real road networks: the case for A. *Int. J. Geogr. Inf. Sci.* **2009,** *23,* 531.

(200) Krone, M., Stone, J. E., Ertl, T.; Schulten, K. Fast visualization of gaussian density surfaces for molecular dynamics and particle system trajectories. *EuroVis-Short Papers* **2012,** *2012,* 67.

(201) Chu, I., Nguyen, H., Hy, S., Lin, Y., Wang, Z., Xu, Z., Deng, Z., Meng, Y. S.; Ong, S. P. Insights into the Performance Limits of the Li 7 P 3 S 11 Superionic Conductor: A Combined First-Principles and Experimental Study. *ACS Applied Materials & Interfaces* **2016,** *8,* 7843.

(202) Hakari, T., Deguchi, M., Mitsuhara, K., Ohta, T., Saito, K., Orikasa, Y., Uchimoto, Y., Kowada, Y., Hayashi, A.; Tatsumisago, M. Structural and electronic-state changes of a sulfide solid electrolyte during the Li deinsertion–insertion processes. *Chemistry of Materials* **2017,** *29,* 4768.

(203) Zhang, W., Leichtweiß, T., Culver, S. P., Koerver, R., Das, D., Weber, D. A., Zeier, W. G.; Janek, J. The detrimental effects of carbon additives in Li10GeP2S12-based solid-state batteries. *ACS applied materials & interfaces* **2017,** *9,* 35888.